IOWA STATE UNIVERSITY
Digital Repository

Graduate Theses and Dissertations

Iowa State University Capstones, Theses and Dissertations

2017

Structural and magnetic properties of metastable phases and undercooled liquids in Fe83B17

Dante Gabriel Quirinale
Iowa State University

Follow this and additional works at: https://lib.dr.iastate.edu/etd

Part of the Condensed Matter Physics Commons

Recommended Citation
Quirinale, Dante Gabriel, "Structural and magnetic properties of metastable phases and undercooled liquids in Fe83B17" (2017). *Graduate Theses and Dissertations*. 16107.
https://lib.dr.iastate.edu/etd/16107

This Dissertation is brought to you for free and open access by the Iowa State University Capstones, Theses and Dissertations at Iowa State University Digital Repository. It has been accepted for inclusion in Graduate Theses and Dissertations by an authorized administrator of Iowa State University Digital Repository. For more information, please contact digirep@iastate.edu.

Structural and magnetic properties of metastable phases and undercooled liquids in $Fe_{83}B_{17}$

by

Dante Gabriel Quirinale

A dissertation submitted to the graduate faculty

in partial fulfillment of the requirements for the degree of

DOCTOR OF PHILOSOPHY

Major: Condensed Matter Physics

Program of Study Committee:

Alan I. Goldman, Co-major Professor

Andreas Kreyssig, Co-major Professor

Matthew J. Kramer

Paul C. Canfield

Kerry Whisnant

Iowa State University

Ames, Iowa

2017

DEDICATION

To Pamela and Josef, for everything.

TABLE OF CONTENTS

LIST OF TABLES vi

LIST OF FIGURES vii

ABSTRACT xvii

CHAPTER 1. INTRODUCTION 1

1.1 Technological and Historical Context 1

1.2 Containerless Processing 10

1.2.1 Conical Nozzle Levitation 12

1.2.2 Electromagnetic Levitation 13

1.2.3 Acoustic Levitation 15

1.2.4 Electrostatic Levitation 15

CHAPTER 2. EXPERIMENTAL BACKGROUND AND METHODOLOGY 19

2.1 Sample Preparation 20

2.2 Electrostatic Levitation 21

2.2.1 The Levitation Mechanism 21

2.2.2 Sample Heating 25

2.2.3 Pyrometry 28

2.2.4 Density Measurements 30

2.3 Magnetic Measurements using a Tunnel Diode Oscillator 32

2.3.1 Adaption for the ISU-ESL 34

2.4 Scattering Measurements 36

2.4.1 High-energy x-Ray scattering 37
2.4.2 BESL 38
2.4.3 Neutron Scattering 40
2.4.4 NESL 40
2.5 X-Ray Analysis 44
2.5.1 Corrections 44
2.5.2 Rietveld Refinement 47
2.5.3 Diffuse Background 51
2.6 Liquid Scattering Analysis 53
2.6.1 Mathematical Foundation 53
2.6.2 Normalization 56
2.6.3 Coordination Number 57
2.6.4 Honeycutt-Andersen Indexing 58
2.6.5 Voronoi Tesselation 59
2.6.6 Reverse Monte Carlo simulations 59

CHAPTER 3. THE SOLIDIFICATION PRODUCTS OF LEVITATED $FE_{83}B_{17}$ STUIDIED BY HIGH-ENERGY X-RAY DIFFRACTION 62

3.1 INTRODUCTION 62
3.2 Experimental Details 64
3.2.1 Sample Preparation 64
3.2.2 X-ray Measurements 64
3.2.3 X-ray Data Analysis 66
3.3 Results 68
3.3.1 Overview 68
3.3.2 Cycles 2 and 3: Liquid $\rightarrow Fe_{23}B_6 \rightarrow Fe_2B$ 68
3.3.3 Cycle 4: Liquid $\rightarrow Fe_{23}B_6$ 77
3.3.4 Evidence for the coherent growth of fcc Fe and $Fe_{23}B_6$ 80
3.4 Summary and Discussion 81

CHAPTER 4. IN-SITU INVESTIGATION OF MAGNETISM IN METASTABLE PHASES IN LEVITATED $FE_{83}B_{17}$ **85**

CHAPTER 5. THE STRUCTURE OF LIQUID $FE_{83}B_{17}$ AND $FE_{83}C_{17}$ **95**

5.1 Introduction 95

5.2 Experimental Methods 97

5.2.1 X-ray and Neutron Scattering 97

5.2.2 Computational Methods 99

5.3 Results 101

5.3.1 The Structure factor $S(q)$ and pair distribution function $g(r)$ 101

5.3.2 Honeycutt-Andersen Index 103

5.3.3 Voronoi Tesselation 105

5.4 Discussion 105

CHAPTER 6. CONCLUSIONS AND OUTLOOK **113**

APPENDIX. SYNERGISTIC STABILIZATION OF METASTABLE $FE_{23}B_6$ AND γ-FE IN UNDERCOOLED $FE_{83}B_{17}$ **116**

LIST OF TABLES

Table 2.1: Voronoi and HA indices corresponding to common structural motifs. . . 59

Table 5.1: The voronoi indices of common structures near the Fe-B and Fe-C eutectic. 108

LIST OF FIGURES

Figure 1.1: Phase diagram of the Fe-B binary from [1] 2

Figure 1.2: The tetragonal Fe_2B structure; $I4/mcm$, $a = 5.12$ Å, $c = 4.25$ Å. Large dark red spheres represent Fe atoms, small green spheres correspond to B. 3

Figure 1.3: (left) bcc Fe structure, $Im - 3m$, $a = 2.8$ Å(right) fcc Fe structure, $Fm - 3m$, $a = 3.62$ Å 4

Figure 1.4: (a) The orhthorhombic Fe_3B structure; $Pnma$, $a = 5.09$ Å, $b = 6.748$ Å, $c = 4.25$ Å[2]. (b) *bct*-Fe_3B, $I\overline{4}$ (c) *pt*-Fe_3B, $P4\frac{2}{n}$. Large dark red spheres represent Fe atoms, small green spheres correspond to B. . . . 6

Figure 1.5: The cubic $Fe_{23}B_6$ structure along the (1 0 0) direction; Fmm, $a = 10.71$ Å. Large dark red spheres represent Fe atoms, small green spheres correspond to B. 8

Figure 2.1: Electrodes currently installed in the ISU-ESL. 22

Figure 2.2: Top view schematic of the ISU-ESL furnace and surrounding instrumentation. 23

Figure 2.3: The core of the positioning system. The "iris" size for LEDs is indicated as a red line. 24

Figure 2.4: A Paschen curve detailing the voltage required to produce dielectric breakdown. 25

Figure 2.5: The HIS13 helium discharge lamp, properly ignited. 27

Figure 2.6: The temperature data from a two color pyrometer on the WU-BESL during solidification of a $Ni_{50}Zr_{50}$ sample. A structural transition during the solidification plateau could be interpreted as noise in the ratio output (black), but the two individual color readings, K1 (red) and K2 (blue) show a clear second recalescence event 31

Figure 2.7: An AlPdMn sample, with a significant oxide phase 31

Figure 2.8: An AlPdMn sample after a high temperature hold 31

Figure 2.9: The BESL as installed at Beamline 6-ID-D. The GE 40RT Revolution 2D detector is pictured to the left. 38

Figure 2.10: A sample being heated in the NESL. Notably, the entire bottom area of the picture is filled by the sample catcher assembly, enabling easy sample retrieval. 42

Figure 2.11: (a) Schematic of the NESL[3] (b) The electrode platform and mirror assembly (c) port layout from above. 43

Figure 2.12: (a) Raw data taken on solid sample (b) Data corrected for background and bad pixels 45

Figure 2.13: Rietveld refinement performed at high temperatures using (a) a 16 term Chebeschev polynomial background function (b) a 25 term Chebeschev polynomial (c) a custom function modeled on the liquid. (see text) . . 52

Figure 2.14: A representative neutron scattering $S(q)$ from the NESL at NOMAD. The black curve is the initial output from the NOMAD data reduction subroutines. The red curve is the curvature attributed to inelastic and secondary scattering, determined via the Peterson metric. The blue curve is the normalized $S(q)$. 56

Figure 2.15: Example of n_4 distinguishing between two different HA topologies. . . 58

Figure 3.1: (Color online) X-ray diffraction measurements taken during free-cooling from the melt for (a) solidification directly into the equilibrium Fe_2B + Fe phases; (b) precipitation of metastable $Fe_{23}B_6$ + liquid phases in the region defined by the dashed green lines, followed by solidification into the equilibrium Fe_2B + Fe phase; (c) Solidification into the metastable $Fe_{23}B_6$ + Fe phases followed by a transformation into Fe_2B + Fe; and (d) primary solidification into $Fe_{23}B_6$ + Fe, which persists down to the lowest temperature measured (900 K). The precipitation of Fe_3B is concomitant with the appearance of *bcc* Fe. 67

Figure 3.2: (color online) Refinements of the x-ray data taken on cooling into the equilibrium Fe_2B + Fe phases [Fig. A.1(b)] for Cycle 2 (a) immediately after solidification is complete, (b) during the Fe allotropic transformation, and (c) at the lowest recorded temperature. The insets show an expanded view near the positions of the (2 0 0) *bcc* and (2 2 0) *fcc* Fe diffraction peaks. The residual intensity at the position of the (2 2 0) *fcc* Fe diffraction peak in panel (c) is due to diffraction peaks from Fe_2B. The brown, blue, and red hash marks denote the calculated positions of diffraction peaks from Fe_2B, *bcc* Fe and *fcc* Fe, respectively. The line below the hashmarks plots the residuals from the fits to the experimental data. 69

Figure 3.3: (color online) (a) Sample temperature curve determined from the pyrometer data taken during the high-energy x-ray diffraction measurement of Cycle 2. The initial temperature signature corresponds to the precipitation of the metastable phase. The second, larger recalescence indicates formation of the equilibrium Fe_2B + *fcc* Fe phases. The event at approximately 42 seconds corresponds to the allotropic *fcc* to *bcc* transition in Fe on cooling. (b) The weight fractions of the Fe_2B phase and Fe allotropes as determined from the sequential Rietveld refinements of the diffraction data. 70

Figure 3.4: (color online) Results of the Rietveld refinement of the diffraction data displayed in Fig. A.1(b). (a) The weight fractions of the Fe_2B phase and Fe allotropes as a function of temperature, (b) The Fe_2B a lattice parameter as a function of temperature compared against the fcc Fe a lattice parameter and, (c) the a lattice parameter for bcc Fe as a function of temperature. All axes are scaled using geometric relationships between the lattice parameters of each structure. 71

Figure 3.5: (color online) (a) Sample temperature curve determined from the pyrometer data taken during Cycle 3. The plateau from 10 to 28 seconds corresponds to the initial formation of the metastable phase. The second recalescence to 1401 K indicates relaxation into the equilibrium Fe_2B + Fe(fcc) phases. The event at approximately 46 seconds corresponds to the allotropic fcc to bcc transition in Fe on cooling. (b) The weight fractions of the $Fe_{23}B_6$, Fe_2B and Fe allotropes, starting from the earliest time in the solidification that sequential rietveld refinement converged. 72

Figure 3.6: (color online) Refinements of the x-ray data taken on cooling into the metastable $Fe_{23}B_6$ + Fe phases during Cycle 4 (a) after solidification is complete, (b) during the Fe allotropic transformation, and (c) at the lowest recorded temperature. The red line corresponds to the best calculated pattern with all phases included, while the black is the pattern calculated from the same set of parameters refined without including fcc Fe. The insets show an expanded view near the positions of the (2 2 0) fcc Fe diffraction peak. The (2 2 0) fcc Fe diffraction peak appears as a shoulder on the low-angle side of a relatively strong diffraction peak from $Fe_{23}B_6$. The green, blue and red, and purple hash marks denote the calculated positions of diffraction peaks from $Fe_{23}B_6$, bcc Fe, fcc Fe, and Fe_3B, respectively. The residual from the final fit to the experimental data is shown in red, while the second line, in black, shows the residual to the fit not including the fcc Fe. 73

Figure 3.7: (color online) (a) Sample temperature curve determined from the pyrometer data taken during the high-energy x-ray diffraction measurement of Cycle 4. The initial temperature signature corresponds to the solidification of the metastable $Fe_{23}B_6$ + Fe phases. Note the absence of a distinct signature of the *fcc* to *bcc* transition for Fe as compared to the data in Fig. 3.4(b). The weight fractions of the $Fe_{23}B_6$, Fe_3B, and Fe allotropes as determined from the sequential Rietveld refinements of the diffraction data. 75

Figure 3.8: (color online) Results of the Rietveld refinement of the diffraction data displayed in Fig. A.1(d). (a) The weight fractions of the $Fe_{23}B_6$ phase and Fe allotropes as a function of temperature, (b) The cubic a lattice parameters as a function of temperature and, (c) the cubic a lattice parameters for *bcc* and *fcc* Fe as a function of temperature. Note the extended temperature range of the *fcc* to *bcc* transition and coexistence of the Fe allotropes on cooling. 76

Figure 3.9: (color online) Rietveld refinement of x-ray diffraction data taken on powder produced from a levitation processed sample exhibiting behavior corresponding to metastable phase formation. Green tick marks represent $Fe_{23}B_6$, red *fcc* Fe, and blue *bcc* Fe. The blue line below the pattern represents the residual difference between the observed data and the refined fit. 77

Figure 3.10: (color online) Several frames of background-subtracted x-ray patterns. (a)-(d) were obtained during the cycles in the BESL presented earlier while (e)-(f) were obtained at ambient temperature on samples processed in the ISU-ESL. (a) Equilibrium solidification of Fe_2B + *fcc* Fe during Cycle 2 directly after the solidification plateau at 1410 K, (c) Same sample a short time later at 900 K with Fe_2B+ *bcc* Fe. (b) Frames from Cycle 4 with $Fe_{23}B_6$ + *fcc* Fe immediately after solidification (d) Same cycle at 900 K with $Fe_{23}B_6$ + Fe_3B + *fcc* Fe + *bcc* Fe present. (e) Sample showing the same thermal profile in the ISU-ESL as those in Cycle 2 (f) Sample with a thermal history resembling that in Cycle 4. . 79

Figure 3.11: (color online) An enlarged section of a frame from Cycle 4, taken immediately following solidification at 1390 K. The green labels on the left indicate the *hkl* index for each ring belonging to $Fe_{23}B_6$, while the red indices on the right delineate the *fcc* Fe rings. 81

Figure 4.1: (color online) (a) and (b) Results of Rietveld refinements of the x-ray data. The red triangles represent *fcc*-Fe, blue triangles represent *bcc*-Fe, and the brown triangles represent Fe_2B. Weight fractions in panel (a) were measured on cooling, and those in (b) were measured on heating. (c) Volumetric data taken in the ISU-ESL. Temperatures labeled as I and II denote the allotropic transition on cooling and heating, respectively. (d) Frequency shift measured by the TDO circuit. The inset displays the peak near 1018 K taken on a similarly-sized sample with data taken at a lower cooling and heating rate (∼0.25 K/s) for higher resolution. Dark blue circles correspond to cooling and orange squares represent the subsequent reheat. The volume is represented as a fractional change from ambient temperature values to more easily compare to the results from the x-ray data. 89

Figure 4.2: (color online) (a) and (b) display results of Rietveld refinements on x-ray data. Green squares represent $Fe_{23}B_6$, red triangles pointing down *fcc* Fe, blue triangles pointing up *bcc* Fe, brown triangles pointing left Fe_2B, and purple circles Fe_3B. Fractions in (a) were measured on cooling, and those in (b) were measured on heating. (c) Sample volume as compared to an ambient temperature measurement. Points I through IV are temperatures corresponding to transitions as described in the text. (d) The measured frequency shift in the TDO. The inset presents a detailed view of the signal near 790 K. 91

Figure 4.3: (color online) TDO output from an anneal following the solidification displayed in Fig. A.2(c) and (d), where the sample was heated to the temperature region where $Fe_{23}B_6$ transforms to Fe_2B + *bcc* Fe + Fe_3B. Orange squares represent the initial heat and eight minute anneal at 990 K, while blue circles represent the subsequent cool. 93

Figure 5.1: Black circles represent experimental $S(q)$ data, while red lines are the corresponding RMC fits. (a) X-ray and (b) neutron diffraction on $Fe_{83}B_{17}$ at 1470 K (c) X-ray and (d) neutron diffraction on liquid $Fe_{83}C_{17}$ at 1450 K 100

Figure 5.2: (a) Comparison of the $g(r)$ obtained for both materials by (a) x-ray scattering and (b) neutron scattering. Brown lines correspond to $Fe_{83}B_{17}$ while green represent $Fe_{83}C_{17}$ 102

Figure 5.3: Most prevalent Honeycutt-Andersen indices among root pairs in the liquid, arranged by prevalence in the Fe-B system 103

Figure 5.4: Most prevalent Voronoi indices in the liquid, arranged by prevalence in the $Fe_{83}B_{17}$ system 104

Figure 5.5: Coordination polyhedra of (a) boron atoms and (b) iron atoms in the Fe_2B structure 106

Figure 5.6: Coordination polyhedra of (a) boron atoms and (b-d) iron atoms in the $Fe_{23}B_6$ structure. (b), (c), (d), and (e) represent $8c$, $4a$, $32f$, and $48h$ sites, respectively. 107

Figure 5.7: Coordination polyhedra of (a) $4c$ carbon atoms, (b) $4c$ iron atoms and (c) $8d$ iron atoms in the θ-Fe_3C structure. 109

Figure 5.8: Most common HA indices in $Fe_{23}B_6$ (black) θ-Fe_3C (red) as fraction of total root pairs 110

Figure A.1: (color online) Time-resolved high-energy x-ray diffraction measurements of $Fe_{83}B_{17}$. Cycles A and B denote two of the seventeen melting/cooling sequences on one of several samples in this study. The x-ray data were obtained at a rate of 2 fps. Panels (a) - (c) and (d) - (f) show the measured temperature of the sample, the corresponding x-ray diffraction pattern with the intensity color-coded and the weight fractions of the crystallization products determined from Rietveld refinements of the x-ray data for Cycles A and B, respectively. For both Cycles the total proportions of Fe and B, calculated from the composition and weight fractions of the constituent phases, remained constant within our experimental uncertainty of 1 -2 %, demonstrating the constant composition of the sample over the course of the measurement. 117

Figure A.2: (color online) Rietveld refinements of the x-ray data from (a) Cycle A and (b) Cycle B at $T = 925$ K, well below the allotropic fcc γ-Fe to bcc α-Fe transition. The hash marks correspond to the expected peak positions for the constituent phases. The lines through the data represent the fits from the refinement and the lines below the hash marks represent the residuals from these fits. No additional unindexed diffraction peaks, within the limits of detection were observed. For panel (a) $R_p = 0.027$. In panel (b) the fits and residuals including all four phases in the fit (red lines) ($R_p = 0.038$) or excluding γ-Fe (black lines) ($R_p = 0.073$) demonstrate a significant improvement in the fit including γ-Fe. The top insets to both panels show portions of the Debye-Scherrer rings recorded at $T = 1390$ K illustrating a smooth continuous nature for Cycle A [panel (a)] and the larger grain structure for Cycle B [panel (b)] in the grayscale encoded intensity. The smaller insets to each panel display an expanded view of the region close to the γ-Fe (220) Bragg peak illustrating the quality of the refinement. 118

Figure A.3: (color online) Volume thermal expansion measurements of $Fe_{83}B_{17}$. The volumes are normalized to the lowest temperature measured on cooling from the liquid. The data acquisition began at (I), with the sample in the equilibrium Fe_2B + γ-Fe solid phases at a temperature of 1420 K. The heating laser power was increased in a single step (black curve) such that the sample melted and was heated to a maximum temperature of 1565 K (II). The heating laser was turned off and the sample underwent free radiative cooling (green curve). At (III) the liquid reached its minimum temperature of 1368 K, corresponding to an undercooling below the Fe_2B melt plateau of $\Delta T \sim 79K$, and underwent recalescence and solidification into the metastable $Fe_{23}B_6$ + γ-Fe phases. A gradual positive deviation (IV) from linear behavior occurred as the sample temperature decreases down to 640 K. After a two minute hold at this temperature, the sample temperature was increased at a constant rate of 3 K/s to 1420 K (orange curve). The cooling and heating curves begin to diverge at (IV) with a step in the volume at (V). After heating to 1420 K, the temperature was decreased to 670 K (blue curve) and increased to 1420 K (red curve) at a rate of 3 K/s. The cooling and heating curves are featureless beyond the expected first-order allotropic phase transition for Fe (VI). 123

ABSTRACT

Containerless processing techniques allow the exploration of several poorly understood areas of materials science and physics. The formation of transient metastable phases is typically challenging to study *in-situ*, and so information on high-temperature solidification pathways and the properties of such phases are often incomplete at best. Similarly, the structure and properties of the undercooled liquid regime are just now being explored. The wide variety of optical instrumentation and scattering techniques available for use with levitation based systems allow novel, multi-faceted approaches to *in-situ* materials characterization.

Metastable phase formation in the $Fe_{83}B_{17}$ system was investigated through a wide variety of techniques using multiple electrostatic levitators. Two primary phase selection pathways were observed via *in-situ* x-ray diffraction studies. Samples either solidified into the equilibrium Fe_2B + fcc-Fe phase or formed a coherently intergrown metastable $Fe_{23}B_6$ + fcc-Fe structure, which either transformed during the solidification plateau to the equilibrium phase or persisted through cooling down to room temperature. The metastable solidification featured a kinetically suppressed allotropic transformation, as well as the irreversible precipitation of a primitive tetragonal Fe_3B structure at low temperatures.

Both solidification pathways were probed with the use of the newly developed ISU-ESL tunnel diode oscillator to observe magnetic transitions through the dynamic susceptibility. In addition to observing the ferromagnetic transition of bcc-Fe, the ferromagnetic transition temperature of the Fe_3B phase was identified to be 795 K. Fe_2B was seen to experience a ferromagnetic transition at 1015 K, which appeared to be characteristic of local moment magnetism. A new transition temperature of 850 K was established for the metastable $Fe_{23}B_6$ + fcc-Fe structure.

The newly developed Neutron Electrostatic Levitator, in conjunction with x-ray scattering results from the Beamline Electrostatic Levitator, was used in combination to probe the liquid

structure of $Fe_{83}B_{17}$ and compared to that of $Fe_{83}C_{17}$. Reverse monte carlo simulations were carried out to model the structure of the liquid, which was then characterized using Voronoi tesselation and Honeycutt-Andersen indexing. In doing so, qualitative evidence for a greater degree of similarity to the $Fe_{23}B_6$ structure in the Fe-B liquid was demonstrated and used to construct an argument for the comparative rarity of observation of the $Fe_{23}C_6$ in the Fe-C binary.

CHAPTER 1. INTRODUCTION

1.1 Technological and Historical Context

In 1976, the first of a new series of ferromagnetic metallic glasses containing only one metalloid component was trademarked by Allied Chemical Corporation[4]. The previous alloys in the series, dubbed Metglas, contained two or three metalloid species, making it challenging to understand trends in structural or magnetic properties of interest. The prevailing understanding of good metallic glass forming materials were that materials exhibiting deep eutectics and a large variance in atomic size, such as metal-metalloid systems, would be the most likely candidates. The Fe-B binary system matches both of these criteria handily. The $Fe_{80}B_{20}$ metallic glass was found to be the strongest, hardest, and stiffest glass yet discovered[5]. Hasegawa et al[6] performed a series of vibrating magnetometer experiments on this newly synthesized system, and determined that the glass exhibited a Curie temperature T_C of 647 K, approximately 11 K below a crystallization temperature of 658 K. This was much higher than the Curie temperatures reported in other Fe-based Metglas materials containing phosphorous and/or carbon. Further studies confirmed the $Fe_{80}B_{20}$ glass showed the highest room temperature saturation magnetization of the Metglas family[7]. The low coercivity associated with the low anisotropy in metallic glasses, combined with a high saturation magnetization, culminated in a tantalizing material for transformer or inductor cores in a number of industrial applications[8].

The $Fe_{80}B_{20}$ glass forming system was thoroughly investigated in the following years, and the numerous studies on the crystallization products of these glasses led to the discovery of a number of metastable structures in the system. However, the sensitivity of the devitrification process to the precise heat treatment applied[9], as well as compositional inhomogeneities resulting from different quenching methods[10] and ribbon thicknesses[11], led to wide discrep-

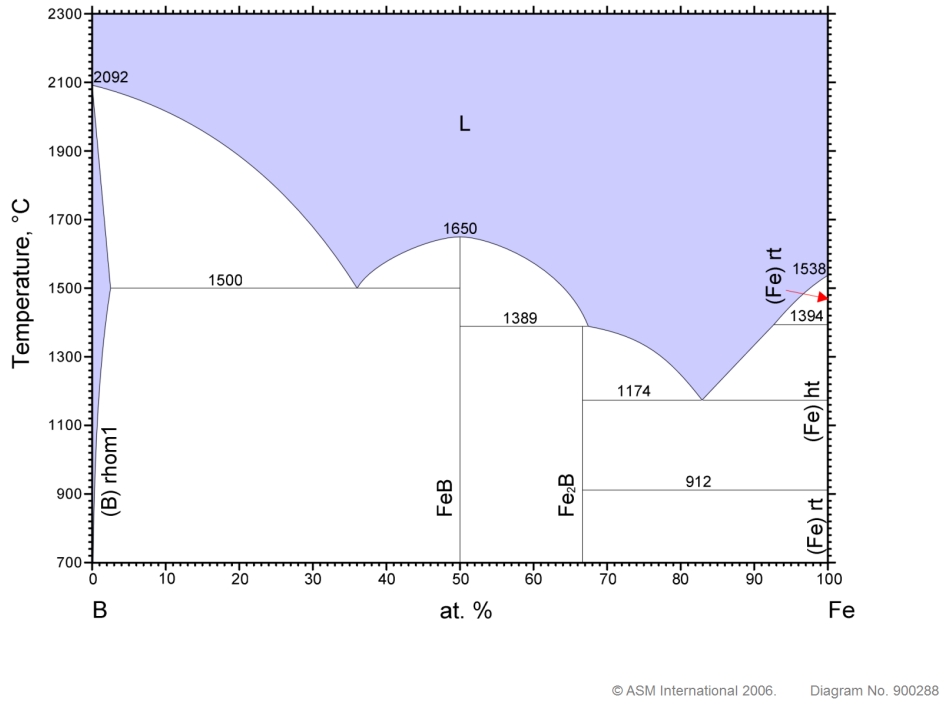

Figure 1.1: Phase diagram of the Fe-B binary from [1]

ancies over the precise nature of the crystallization pathways from the glass, causing confusion over the thermodynamics of the system and a number of competing proposals regarding the kinetics of crystallization in the system[12].

Typical glass forming compositions in the system range from $Fe_{73}B_{27}$ to $Fe_{91}B_9$[13], with the lowest critical cooling rate at the eutectic of $Fe_{83}B_{17}$[14]. According to the equilibrium phase diagram[1] (Fig. 1.1), at the relevant compositions near the eutectic, the stable boride is body-centered tetragonal Fe_2B ($I4/mcm$, $a = 5.12$ Å, $c = 4.252$ Å)[15] as seen in Fig. 1.2. Fe_2B is ferromagnetic[16] with Curie temperature T_C of 1015 K [17], and experiences a shift in its easy axis of magnetization between 460 and 480 K[18]. At high temperature, from 912°C to 1394°, the fcc allotrope of Fe (γ-Fe, $Fm\overline{3}m$, $a = 3.57$ Å) is stable. At 912°C, on cooling, γ-Fe transforms to bcc-Fe (α-Fe, $Im\overline{3}m$, $a = 2.8$ Å). Both allotropes are displayed in Fig. 1.3. These are the only equilibrium structures near this composition. As it turns out, however, there are several metastable structures involved in a typical crystallization pathway.

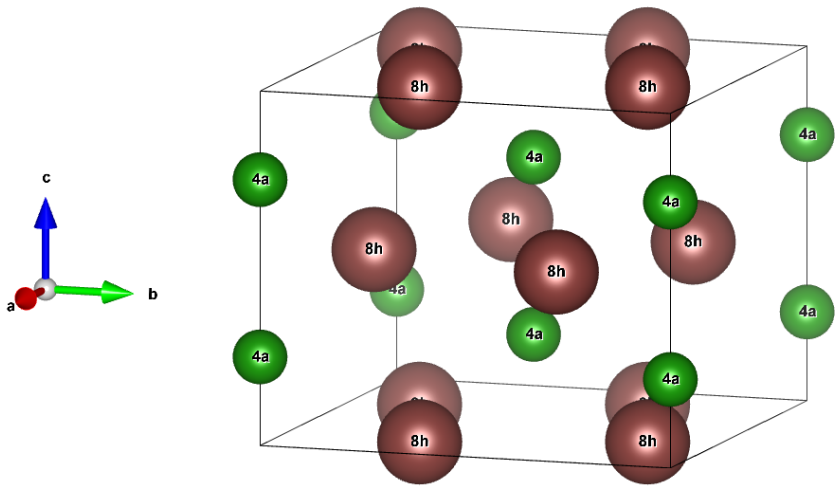

Figure 1.2: The tetragonal Fe_2B structure; $I4/mcm$, $a = 5.12$ Å, $c = 4.25$ Å. Large dark red spheres represent Fe atoms, small green spheres correspond to B.

Hasegawa et al [6] performed several of the early devitrification studies of the alloy. Their initial x-ray diffraction study of the ensuing phases yielded α-Fe and a phase that appeared to be consistent with orthorhombic Fe_3B (θ-Fe_3B, $Pnma$), isomorphic with the common metastable carbide Fe_3C. They attributed this Fe_3B structure a T_C of 793 K, while others have claimed a T_C of 897 K[19]. By contrast, Koster et al [20] determined that devitrification resulted in plate-like α-Fe particles embedded in a matrix composed of a tetragonal phase with a stochiometry near Fe_4B, independently observed by electron microscopy[21], though no explicit form of the structure was ever determined. Koster only observed θ-Fe_3B after annealing the system above 950 K. Heating the system above 1270 K caused a structural transformation to the equilibrium Fe_2B + γ-Fe phase.

Yet another devitrification study by Greer[22] found only a body-centered tetragonal variant of Fe_3B (*bct*-Fe_3B, spacegroup $I\overline{4}$, $a = 8.63$ Å, $c = 4.87$ Å), isomorphic with Fe_3P, was always present during devitrification, a conclusion supported by further studies [13, 23]. This phase was also suggested to have a Curie temperature of ∼800 K[24]. Later work on annealing $Fe_{80}B_{20}$ at 380°C also observed *bct*-Fe_3B by transmission electron microscopy (TEM) and x-ray diffraction (XRD), as well as noting a contiguous, possibly coherent, α-Fe phase[25]. Alternatively, Khan

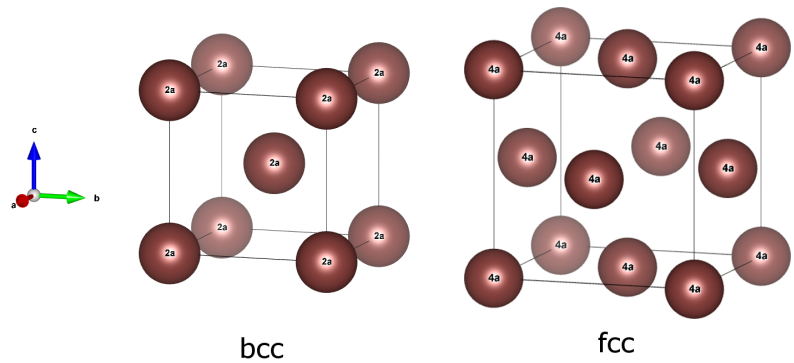

Figure 1.3: (left) bcc Fe structure, $Im-3m$, $a = 2.8$ Å(right) fcc Fe structure, $Fm-3m$, $a = 3.62$ Å

et al[26] observed a primitive tetragonal Fe_3B phase (pt-Fe_3B, $P42/n$, $a = 8.655$ Å, $c = 4.297$ Å), an observation later repeated by Inal[12], who claimed it preceded any other Fe_3B phases during crystallization. Observation of this phase was also mirrored by Rundqvist in the Fe-B-P ternary system[27], who established a model of the structure.

Theoretical studies of these boride compounds have established that Fe_2B is the only stable boride in this region[28]. Due to their metastable nature, there is a dearth of experimental examinations of their properties, it is difficult to obtain physical parameters as inputs and constraints on simulations. The similarity between the structures caused further disagreement and confusion, as they may have been misidentified in the past. This has even led some to wonder if the Fe_3B phases were, in fact, stable[29].

Meanwhile, following the initial flurry of activity on the Fe-B glasses, a new permanent magnet system was discovered. Previously, the market for hard magnetic materials had been dominated by Sm-Co magnets. Nominally created as $SmCo_5$ and Sm_2Co_{17}, these hard magnets proved expensive for applications requiring mass production of large magnets, such as the automotive industry. In 1982, General Motors and Sumitomo Special Metals independently developed a new class of rare-earth magnets based on neodymium iron boron (specifically, Nd_2Fe_14B)[30]. The new magnets exhibited a rare-earth stabilized magneto-crystalline anisotropy[31] that resulted in high coercivity[30] similar to the SmCo magnets, but at much lower cost, making them far more attractive for applications not requiring the higher T_C of

SmCo. The new magnets were produced either by sintering or through crystallization from melt-spun ribbons, producing nano-crystalline magnetic structures. Soon thereafter, a number of devitrification studies on Nd-Fe-B ternary glasses were performed.

In a seminal work detailing the new principle of the "Exchange-Spring Magnet", Kneller and Hawig [32] developed a microstructure prototype wherein hard magnetic nanoparticles were surrounded by a soft magnetic matrix, promoting intergrain ferromagnetic exchange coupling for the enhancement of a number of critical properties, and described such a system by using the microstructure produced on devitrification of $Nd_{3.8}F_{77.2}B_{19}$. In contrast to the previous studies on binary $Fe_{80}B_{20}$ glasses, however, they note that neither α-Fe or any variation of Fe_3B were the initial devitrification products. Instead, a complex metastable cubic phase, $Fe_{23}B_6$ (spacegroup $Fm\overline{3}m$, $a \sim 10.70$ Å), shown in Fig.1.5 and isomorphic with $Cr_{23}C_6$, was observed on crystallization every time. They reasoned that the broad crystalline reflections they had observed via x-ray diffraction during the crystallization process could be attrributed to this structure containing a significant amount of dissolved Nd, and noted it appeared to be the only metastable boride capable of doing so. Upon formation, the $Fe_{23}B_6$ immediately began to decompose to α-Fe and Fe_3B, leading to a supersaturation of Nd in the residual $Fe_{23}B_6$. The remaining $Fe_{23}B_6$ eventually transformed to the hard magnetic phase $Nd_2Fe_{14}B$, set in the soft magnetic matrix of Fe_3B. By alloying with small amounts of silicon and/or vanadium, this sequence could be controlled to reduce or eliminate the initial decomposition into α-Fe and Fe_3B, producing a range of microstructures.

Devitrification and metallic glasses are not a focus of this dissertation, as the studies presented in later chapters are primarily related to solidification from the undercooled liquid. However, aside from painting a picture of the confusion of poorly-characterized metastable phases present in the system and establishing some of the historical interest in this alloy, these studies may be instructive in light of the intimate relationship between the local structure of a metallic glass and the short range ordering in the undercooled liquid it is produced from[33]. Given the theorized similarity in the cohesive energies of many of these borides [28], the contribution of interfacial energies in the phase selection process or the kinetics associated with the phase transformations should be considered. Recent *in-situ* measurements during solidification

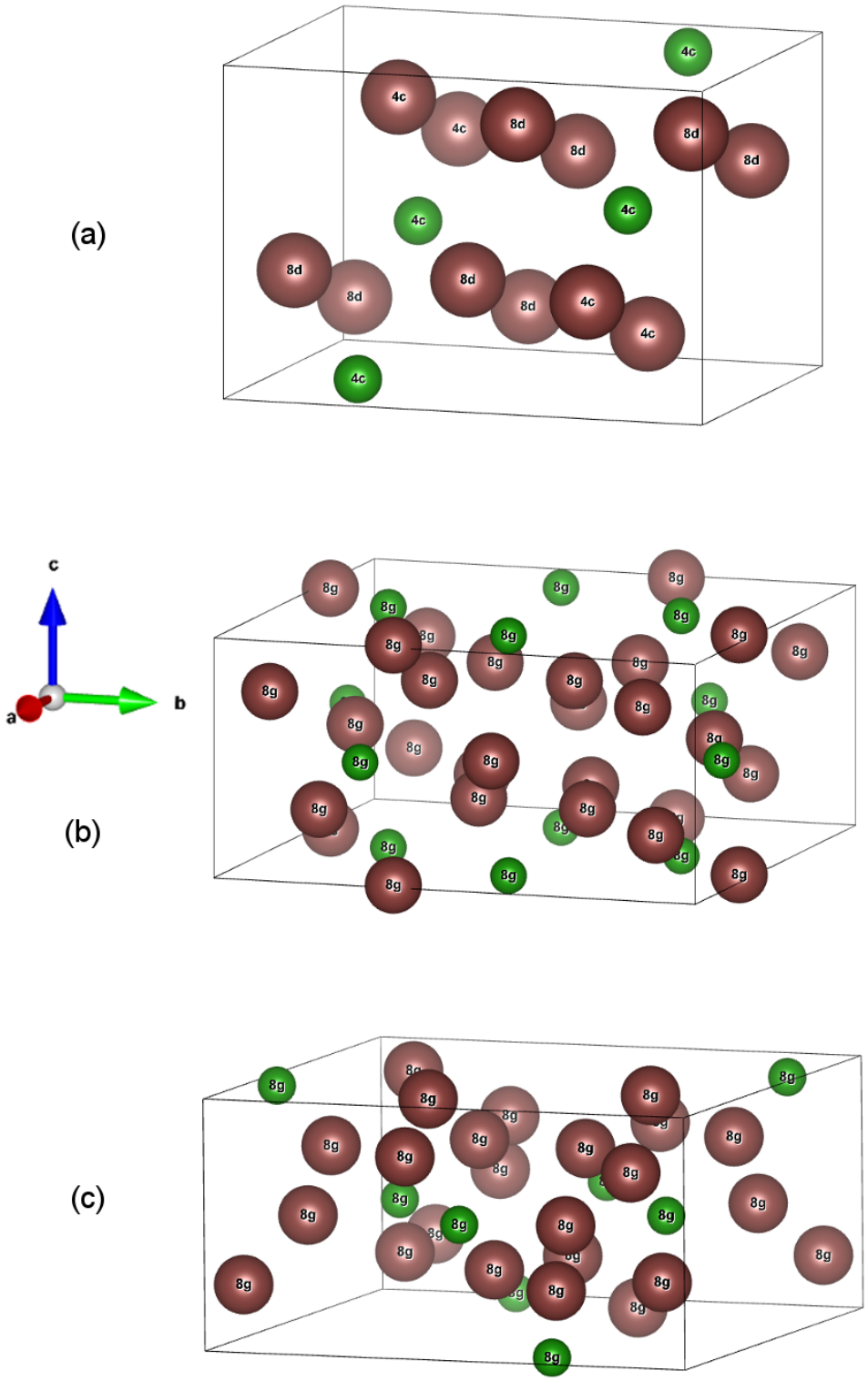

Figure 1.4: (a) The orhthorhombic Fe_3B structure; $Pnma$, $a = 5.09$ Å, $b = 6.748$ Å, $c = 4.25$ Å[2]. (b) bct-Fe_3B, $I\overline{4}$ (c) pt-Fe_3B, $P4\frac{2}{n}$. Large dark red spheres represent Fe atoms, small green spheres correspond to B.

of other systems have revealed transient phases that effectively lower the nucleation barrier [34], and the importance of the $Fe_{23}B_6$ system as a transient phase during the crystallization of some glassy phases arouses some curiousity about a similar role during solidification.

In this regard, while solidification in the Nd-Fe-B ternary has been studied fairly extensively[35–41], solidification studies of binary near-eutectic Fe-B are comparatively rare, and provide conflicting information on the formation of metastable borides. Yang et al thermally cycled $Fe_{83}B_{17}$ samples under a glass flux at the eutectic composition and found they exhibited a wide range of undercooling [42, 43]. Performing XRD and TEM on solidified samples showed that for undercooling temperature $\Delta T < 386$ K, the equilibrium α-Fe + Fe_2B phase resulted. For $386 < \Delta T < 460$ K, metastable tetragonal Fe_3B was formed and persisted to room temperature. No other metastable phase was found. That study reported that the Fe_3B phase remained after annealing at 858 K for up to 16 hours and at 1223 K for up to 3 hours, decomposing after 5, as verified by SEM micrograph analysis. Battezzati et al [44] also observed an Fe_3B phase through similar methodology, but were unsure of the precise symmetry of the phase, noting only that it transformed to the equilibrium phases on heating to ∼1300 K. Neither of these studies observed $Fe_{23}B_6$.

To observe solidification of these metastable phases *in-situ*, conical nozzle levitation was combined with XRD to study both $Fe_{83}B_{17}$ and $Fe_{83}C_{17}$ at cooling rates up to 170 K/s[45]. In $Fe_{83}C_{17}$ they observed first the formation of γ-Fe at 1420 K, followed by θ-Fe_3C at 1000 K, contrary to expectations from the phase diagram, which suggests a eutectic solidification. No evidence of $Fe_{23}C_6$ was observed. By contrast, in $Fe_{83}B_{17}$ the $Fe_{23}B_6$ structure was seen to precipitate as the primary, and only, phase. At cooling rates of 30 K/s it transformed to the equilibrium Fe_2B + γ-Fe phase; at 170 K/s the $Fe_{23}B_6$ persisted below the sensitivity of their pyrometer, though a small amount of α-Fe was seen to appear. No Fe_3B was observed, and no quantitative phase analysis was performed. This is the first instance of the $Fe_{83}B_{17}$ structure appearing as the primary constituent of the binary.

Barinov et al successfully obtained single phase $Fe_{23}B_6$ by mechanical milling [46]. Their sample exhibited a Curie temperature of 601 K at the nominal composition of 20.7 at% boron, but demonstrated a sensitive dependence on the boron composition and ranging as high as

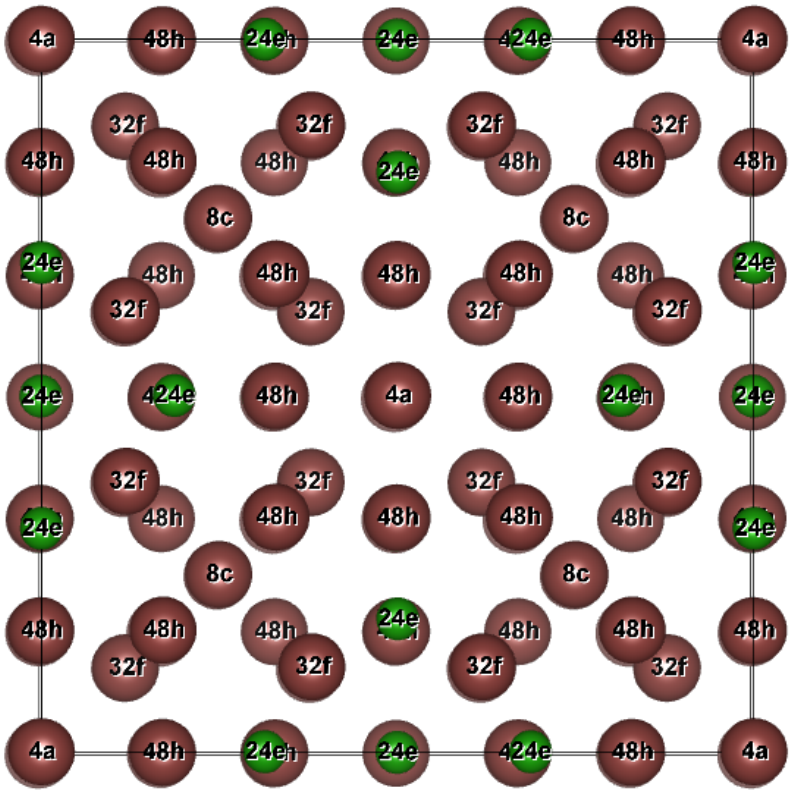

Figure 1.5: The cubic $Fe_{23}B_6$ structure along the (1 0 0) direction; Fmm, $a = 10.71$ Å. Large dark red spheres represent Fe atoms, small green spheres correspond to B.

750 K. Upon applying Mössbauer spectroscopy to further detail the local atomic environments, they observed a curious precipitation of α-Fe, where the weight fraction of α-Fe varied between 0.6 wt % and 12-15 wt %[47]. This appeared to have no effect on the ferromagnetic ordering temperature. They attributed this phenomenon to the "Diverse Atomic Position Occupancy" (DAPO) effect, a mechanism by which Fe atoms moved from the $4a$ to $4b$ sites[47].

The $Fe_{23}B_6$ structure also came under renewed scrutiny through the work of computational physicists. Fang et al [48] determined that the low vacancy energy of several of the Fe sites, combined with a large variety of electronic structures and magnetic moments, led to a range of chemical environments that allowed easy substitution of other transition metal atoms. They studied a number of structural models, varying the site occupancies and positions, and compared their cohesive energy to that of pure austenitic γ-Fe and the diamond structure (and, by extension, graphite). At least one variant of the $Fe_{23}C_6$ was found to be even more energetically stable than θ-Fe_3B (19.5 meV/atom vs 20.6 meV/atom, respectively). Additionally, they determined that the Fe sites on the (1 0 0) plane of the $Fe_{23}C_6$ structure matched the (1 0 0) plane of austenite well enough to develop an epitaxial growth relationship, implying a possible reduction in the nucleation barrier to forming the $Fe_{23}C_6$ structure out of an austenitic matrix. They concluded that one would expect to see this structure much more commonly in steel alloys, a thought echoed elsewhere [49]. However, despite the predicted thermodynamic stability and structural flexibility, $Fe_{23}C_6$ is never seen in the Fe-C binary, and is only observed in multicomponent systems.

Providing somewhat contrary results, ab inito MD simulations [50] were performed to study the stability of the $Cr_{23}C_6$ structure in ternaries based on Fe-B and Fe-C. Their interest in the system was in preventing the $Fe_{23}(B,C)_6$ structure from forming, considering it a primary competitor to glass formation in the system. Other studies [45] suggested that the appearance of the $Fe_{23}B_6$ phase was related to the glass formability of the system. Thermodynamicaly, Widom found that while $Fe_{23}B_6$ had a slightly higher cohesive energy than equilibrium Fe_2B, $Fe_{23}C_6$ was found to have the lowest energy of all of the metastable carbides. Their approach claimed that the structure would be *destabilized* with the substitution of sufficiently large rare-

earth atoms onto the Fe sites, the opposite conclusion of previous experimental work[32] and theoretical predictions[51].

As discussed through both devitrification processes and solidification from the liquid, rare *in-situ* studies seem to suggest that $Fe_{23}B_6$ plays an important role, either as a transient metastable phase or as a primary solidification product. It is possible kinetic factors contribute to this, and the local structures of the glass or the liquid may play a role. Many models have been proposed for the glass structure, generally envisioning a network composed of structural motifs similar to the metastable crystallization phases[52, 53] arranged dense-packed solute-centred atomic clusters[54, 55], based on structure factors from diffraction[56] or simulation[57]. The additional icosahedral ordering of the $Fe_{23}B_6$ structure appears to be less common in the binary FeB glasses, appearing when larger atoms, such as Nd or Nb, are alloyed[55]. The liquid itself is commonly suggested to exhibit the trigonal prisms dominant in the Fe_3B structures and the archimedian antiprisms related to the boron environments in the $Fe_{23}B_6$ structure[58]. However, icosahedral ordering is also frequently observed in undercooled liquid metals[59] and is correlated with glass-formability[60, 61].

The variation of solidification or crystallization products among the different methods and the lack of concrete phase analysis suggest a need for another look at the phase selection pathways in the system. While some variability is expected due to different methodologies, theoretical studies require some experimental constraints; in this regard, due to the metastability of these phases, there are barely any experimental studies to use for comparison. For instance, what experimental work does exist on the local atomic environments in $Fe_{23}B_6$[46, 47] conflicts with theoretical models of the structure[62, 49]. Given the importance of these sometimes transient phases and the difficulty of experimentally studying them (or even creating them), a new approach is required. It is here that the utility of containerless processing techniques become apparent.

1.2 Containerless Processing

The development of levitation-based containerless processing furnaces stretches back to the early 20th century, with the first appearances of electromagnetic levitation (EML), patented

in 1923 [63]. The utility of the approach is multi-faceted, avoiding common problems in high-temperature metallurgical processing, allowing easy *in-situ* characterization of solidification processes, and enabling the study of a new regime of liquid physics.

For one, from a very practical perspective, special care must be taken with the selection of container materials to avoid alloying processes that could at best cause cross-contamination and at worst threaten the integrity of the crucible itself. A particular example of great relevance to the origins of the ISU-ESL project involves the many attempts to study the resistivity of liquid silicon and other reactive high temperature liquids, which have been stymied by the introduction of impurity phases from container walls and the resulting scatter in experimental data[64]. Further complications arise when the interest lies in structural changes during solidification processes, and special furnaces optimized for scattering environments are often needed, introducing a large, unavoidable background. By contrast, levitation systems optimized for scattering, though comparatively rare, enable repeated thermal cycling and low-background structural studies while bypassing many of these technical hurdles.

Perhaps the more significant benefit of a containerless processing environment is the elimination or reduction of the influence of impurity phases and container walls on the solidification process. Classical theory models nucleation as the formation of clusters, with an associated energy $\Delta G(r)$ given by

$$\Delta G(r) = -\frac{4}{3}\pi r^3 \Delta G_{\mathrm{LS}} + 4\pi r^2 \gamma_{\mathrm{LS}} \tag{1.1}$$

where r is the radius of the cluster, ΔG_{LS} is the bulk Gibbs free energy difference per unit volume, and $\gamma_{\mathrm{LS}} > 0$ is the interfacial energy. Below the melting temperature, $\Delta G_{\mathrm{LS}} > 0$, and so there is a critical cluster size $r^* = \gamma_{\mathrm{LS}}/\Delta G_{\mathrm{LS}}$ beyond which it becomes energetically favorable for the cluster to grow. The activation energy ΔG^* to create this critical cluster is given by

$$\Delta G^* = \frac{16\pi\gamma_{\mathrm{LS}}^3}{3\Delta G_{\mathrm{LS}}^2} \tag{1.2}$$

In this framework, the nucleation rate I(T) may be calculated according to

$$I(T) \sim \frac{10^{36}}{\eta(T)} \exp(-\frac{\Delta G^*}{k_{\mathrm{B}}T})\mathrm{m}^{-3}\mathrm{s}^{-1} \tag{1.3}$$

where $\eta(T)$ is temperature dependent viscosity and k_{B} is the Boltzmann constant[65]. By contrast, in the case of heterogenous nucleation on a surface, such as a container wall, the heterogenous activation energy is given by

$$\Delta G^*_{het} \; = \; G^* f(\theta) \tag{1.4}$$

where $0 \leq f(\theta) \leq 1$ is a function of the wetting angle θ and is given by

$$f(\theta) = \frac{1}{4}(2 - 3\cos\theta + \cos^3\theta) \tag{1.5}$$

While the nature of heterogenous nucleation means that there are fewer potential nucleation sites, the exponential function in the nucleation rate is greatly affected by reducing the wetting angle, affecting the rate of nucleation by many orders of magnitude.

By removing container walls and eliminating a large source of heterogenous nucleation sites, a liquid may be readily undercooled. Studies of this state have, to date, largely focused on the short and medium range ordering in the liquid, its relation to solidification pathways, as well as the formation of non-equilibrium states such as metastable crystal phases or bulk metallic glasses. There are a number of levitation based schemes in use today; the following is a short overview of the most common methods.

1.2.1 Conical Nozzle Levitation

Conical nozzle levitation (CNL) is mechanically the simplest technique to achieve levitation. The sample is placed in the eponymous nozzle, and connected to a gas line. The nozzle is designed such that Bernoulli forces will guide the sample back to the levitation axis. Levitation of a sample of mass M may be described by

$$\int [\frac{1}{2}\rho\mu^2 + p]\mathrm{d}A \; = \; Mg \tag{1.6}$$

where ρ is the gas density, μ is the flow velocity, and p the gas pressure[63]. Typically, high purity noble gasses are used as a levitation gas, though there is the potential for application of special reducing atmospheres, and oxygen-rich atmospheres are commonly applied for oxide studies. The levitation mechanism is material agnostic, the main limitation on material selection being that the surface tension of the sample in the liquid state must be sufficient to maintain sample integrity. Typical setups employ a high powered CO_2 laser aimed at the top of the sample, though some employ RF heating. A pyrometer is used to measure sample temperature from above.

A drawback of CNL is that the stable region of levitation for these setups is such that only a hemispherical fraction of the sample is visible above the nozzle. For the purposes of structural studies, this requires special nozzle materials (vanadium, or aluminum) or intensive beam collimation that can affect statistics. In addition, the sample is heated only from the top, while gas flow from below provides cooling power, establishing thermal gradients on the order of 30 K for metals and up to 80 K for oxides [63]. Further, the flow of gas across the surface can interfere with single and two color pyrometers, adding significantly to the measurement uncertainty. This flow also interferes with determination of surface tension and viscosity.

1.2.2 Electromagnetic Levitation

A slightly more complicated setup, electromagnetic levitation furnaces, are based around a specially designed levitation coil powered by an RF generator. The field produced by the RF-coil induces eddy currents in the sample, which experiences a Lorentz force according to

$$F \; = \; \frac{\bigtriangledown B^2 4\pi}{6\mu_0} a^3 G(\frac{a}{\delta}) \tag{1.7}$$

where a is the sample radius, δ is the sample skin depth given by $\delta = \sqrt{2/\omega\mu\mu_0\sigma}$, σ is the sample conductivity, and μ is the permeability[66]. The function $G(x)$ is given by [63] as

$$G(x) = \frac{3}{4}(1 - \frac{3}{2x}\frac{\sinh(2x) - \sin(2x)}{\cosh(2x) - \cos(2x)}) \tag{1.8}$$

Critically, since the levitation mechanism depends on the development of eddy currents, EML is limited to the study of metals of sufficient conductivity. Additionally, ohmic heating due to resistive losses from the eddy currents leads to a power dissipation of

$$P = \frac{B^2\omega}{2\mu_0}\frac{4\pi}{3}a^3 H[\frac{a}{\delta}] \tag{1.9}$$

where ω is the frequency of the field and H(x) is given by[63]

$$H(x) = \frac{9}{4x^2}(x\frac{\sinh(2x) + \sin(2x)}{\cosh(2x) - \cos(2x)} - 1) \tag{1.10}$$

Not only is the levitation mechanism coupled to the heating mechanism, but positional variations of the sample in the coil will alter the power absorbed. Simply levitating a sample is often enough to keep it in the liquid state;, a cooling gas is used to maintain some control of the temperature and enable solidification. Temperature is measured via pyrometry. Typically, samples are several hundred milligrams and on the order of 6 mm in diameter, though micro-EML setups have been used for samples closer to 20 mg[67]. The geometry of levitation apparatus, requiring coils surrounding the sample, make this technique more difficult to apply to scattering environments, though it has been successfully installed for high-energy x-ray investigations at the ILL and ESRF[68].

EML systems have also been used to measure resistivity by implementing a secondary measurement coil and observing the voltage induced by magnetic fields produced by eddy currents in the levitated sample [69]. This is of tremendous interest when applied to liquids, controlling melt flow under the influence of an electromagnetic field or signifying structual changes. However, the technique requires precise knowledge of the shape of the sample, which is typically deformed when processing under normal gravity conditions. Microgravity experiments are currently underway on the International Space Station to bypass this drawback.

1.2.3 Acoustic Levitation

In the acoustic levitation scheme, materials are levitated by being placed in acoustic pressure nodes. The technique has been applied to a range of materials, such as tungsten and liquid mercury [63], with a viable temperature range up to ∼800 K, limited by the changes in gas density near a hot sample[70]. The levitation force, driven by high intensity sound waves, frequently results in deformation of the sample, increasing uncertainty in schemes to measure surface tension or viscosity. However, the technique is optimal for systems that are liquid near room temperature, such as sensitive biological samples. Some groups have used the technique to levitate small insects and fishes, noting that the insects survived, while the "vitality of the young fish is reduced due to inadequacy of water supply" [71]. A promising application of the acoustic technique is to hybrid systems, such as the aero-acoustic systems developed by Weber et al[72]. The aero-acoustic system offers a full field of view of the sample, floating well out of the levitation nozzle, while stabilizing it on the gas jet with a series of acoustic transducers.

1.2.4 Electrostatic Levitation

The history of the development of the electrostatic levitation technique is a fascinating one, born out of microgravity research, and developed initially by several space agencies. A detailed history of the development of ESL can be found in Ref. [73], which chronicles the development of a number of ESL systems and hybrid furnaces around the globe in the last two decades. Each furnace is unique. Available property measurements range from determination of hemispherical emissivity[74], electrical resistivity[75], creep[76], surface tension[77] and viscosity measurements[78], density[79], triggered nucleation and growth front studies[80], and structural determination through x-ray and neutron scattering. The technique is typically performed in a high vacuum environment, eliminating any concern about metal-gas interactions on thermophysical measurements, but high pressure variants are also in use for volatile materials. Additionally, ESL features an open view of the sample for optical and scattering measurements. Any material that can hold a charge is theoretically available for experiments, though the need for a low vapor pressure remains a significant restriction on alloy choice. The

technique is the most challenging in terms of operator skill and knowledge, requiring constant attention and a firm mechanical intuition.

The first ESL experiments were carried out during parabolic flight by the European Space Agency, first in 1977 and again in 1988. Beginning in the 1980s and continuing through the 90s, the National Aeronautics and Space Administration (NASA) Jet Propulsion Laboratory (JPL) invested considerable effort in the development of electrostatic levitation furnaces. While the initial prototype system relied heavily on large concave electrodes for lateral control, the second facility implemented an early version of the positioning system described in Chapter 2. A set of four electromagnetic rotors were added in sequence around the top electrode to control sample rotation.

Space Systems Lorals Electrostatic Containerless Processing System ESCAPES[81] was constructed soon after this, featuring a deuterium arc lamp for charging and a separate YAG laser for heating. This system eventually became the Marshall Space Flight Centers (MSFC) ESL, which was later modified for use in a high-energy x-ray scattering beamline at the Advanced Photon Source (APS) at Argonne National Laboratory. The modified system was deemed the BESL[82]. The early studies performed at the APS with the MSFC BESL focused on the nature of the ordering in undercooled liquids. The BESL had been used to probe the nature of the short range ordering in deeply undercooled liquid silicon as it related to the predicted liquid-liquid transition [83, 84], as well as describe the influence of the icosahedral short range ordering in the liquid on the nucleation barrier [85, 86].

A new system inspired by this BESL, as well as the system developed by the DLR in Germany, the Washington University Beamline Electrostatic Levitator (WU-BESL)[87], followed soon after. The WU-BESL was designed specifically for high-energy x-ray scattering studies performed at the APS, and was the result of a collaboration between Washington University, Iowa State, and NASA scientists. It was an attempt to design a more mobile and compact levitator than the previous iteration, and was first successfully deployed to the APS in 2010. The Washington University group has historically focused on glass-forming systems, and so many of their experiments focused on zirconium based BMG alloys. The WU-BESL also implemented density, viscosity, and surface tension based measurements [88, 89]. The combination of these

physical and structural capabilities has led to an increased understanding of the contribution of liquid fragility to glass formability and a universal scaling relation of the viscosity of liquid metals [90] relating $\log(\nu/\nu_0)$ to T_A/T, where T_A represents the departure from Arrhenius behavior and corresponds to the onset of cooperative motion in the liquid.

To further probe liquid short and medium range ordering, an ESL was commissioned for the Spallation Neutron Source (SNS) at Oak Ridge National Laboratory (ORNL). Dubbed the NESL[91], the levitator was designed for integration into multiple beamlines, and has so far been tested in BL1B (NOMAD) and BL18 (ARCS). The first results from the instrument used the contrast between neutron and x-ray liquid structure factors to describe the short range ordering in ZrPt and ZrRh [92]. Recent experiments, in collaboration with the Iowa State team, have been designed to further explore the ramifications of the universal viscosity relation, using inelastic neutron scattering to find excitations relating to diffusion in the liquid above and below T_A.

Concurrent with the development of the WU-BESL, an ESL system was constructed at Iowa State, dubbed the ISU-ESL[62]. Driving the construction was the implementation of a tunnel diode oscillator (TDO) for high temperature resistivity and dynamic susceptibility measurements [93]. In general, the ISU-ESL functions as a permanent thermophysical and electrical property measurement system, and is considered more stable than its sister systems. The ISU-ESL group works closely with the Washington University team for scattering experiments, but has focused on materials deemed difficult to process. Initial studies at the 2010 commissioning run of the WU-BESL included structural studies of undercooled CoPd, a material of interest for its fascinating magnetic properties at deep undercooling [67], its potentially magnetically triggered nucleation mechanism [94], and the possibility of study with the TDO. Later work focused on gaining high quality x-ray diffraction data from undercooled liquid Si[95] and germanium, and attempting to obtain similar structural data from neutron diffraction using the NESL for direct comparison and evaluation of possible discrepancies in the x-ray atomic form factor of liquid silicon. Additionally of interest have been transient phase formation in the NiZr glass forming system[96], the AlPdMn quasicrystal forming system[97], and a number of other alloys featuring complex metastable phases, including FeZr, FeSi, and NiB.

Work on eutectic Fe-B began in the ISU-ESL lab in 2013 when x-ray data was acquired during solidification of $Fe_{83}B_{17}$ samples during a WU-BESL experiment at the APS. The analysis of this data concluded in early 2015 with the surprising results presented in Chapter 3 and Appendix, at which point it became the topic of this dissertation. Chapters 3, 4, and 5 summarize the work performed since then.

CHAPTER 2. EXPERIMENTAL BACKGROUND AND METHODOLOGY

One of the greatest strengths of the electrostatic levitation technique is its versatility. The wide range of accessible sample materials combined with the open field of view for a wealth of thermophysical optical instrumentation and the availability of furnaces integrated into scattering beamlines for structural studies, can, in the hands of a skilled and lucky operator, lead to a veritable wealth of data.

The studies presented in later chapters made combined use of many of the current capabilities of the ISU-ESL, the WU-BESL, and the NESL. This chapter serves as an overview of these techniques; each of these recently constructed levitation systems has extensive published work associated with their construction and operation, and for a more thorough outline the reader is invited to delve into the work of Rustan [93], Mauro[98, 99, 91], and Derendorf[100]. These systems are complex and temperamental, and those seeking a more thorough understanding of the ISU-ESL are referred to the excellent discussion in Ref. [62].

First, the preparation of levitation spheres will be explained. Then, the core components of the ESL technique will be described, along with the basic thermophysical measurements common among most systems. Next, the tunnel diode oscillator (TDO) circuit implemented into the ISU-ESL for magnetic susceptibility measurements will be briefly discussed. Details of the x-ray scattering performed will be presented in Section **??**, with particular regards to the design of the WU-BESL setup, the protocols and corrections required, and the Rietveld refinement methods critical to Chapters 3 and 4. The NESL, and the neutron scattering measurements performed with it, will then be described. Finally, as it is a much less common formalism than those pertaining to crystal structures, a brief summary of the mathematics of liquid scattering is presented, the application of the reverse Monte-Carlo (RMC) simulation

technique to experimental diffraction data, and the various methodologies for interpreting the resulting ensembles, will be laid out.

2.1 Sample Preparation

All Fe-B and Fe-C samples prepared for the studies in this thesis were prepared by a combination of techniques at the Ames Laboratory Materials Preparation Center (MPC) and within the ISU-ESL itself. Iron from Toho Zinc (99.99% purity, metals basis), Boron from first Alfa Aesar (99.9999% purity, metals basis) and later B^{11} from Eagle Pritcher (99.54% purity), and Carbon from Alfa Aesar (99.9995% purity, metals basis) were first arc melted to form ∼20 g ingots. First the iron was arcmelted several times under a reducing atmosphere. The boron or carbon was then added, and the resulting ingot melted, flipped, and remelted six times to promote homogenization.

The ingots were then broken into chunks sized appropriately for the levitator of choice; 20 to 100 mg for ESL and BESL studies, and 200 to 400 mg chunks for NESL studies. The pieces were were then placed on polished copper or graphite blocks within the ISU-ESL, chosen for their high thermal conductivity and easy of cleaning, and the chamber evacuated to high vacuum conditions ($\sim 10^{-7}$ torr). Each sample was melted once to form a sphere.

The chamber brought up to partial atmosphere ($\sim$ 300 torr) by backfilling with a forming gas (Airgas, 5% H, 95% Ar, 99.999% purity). The samples were then melted and held briefly in the liquid state so that the surface of the sample could be observed via the visualization camera to monitor the reduction of any surface oxides. This was typically performed multiple times, and the samples flipped, the chamber evacuated, and backfilled again, to ensure the entire surface of the sample was exposed to the reducing atmosphere. Examples of samples before and after forming gas processing are shown in **figure x**.

Each sample was individually monitored, and the mass measured before the initial vacuum melting, after any forming gas processing, and after any levitation processing, in order to track evaporative mass-loss. Typically, no measurable mass loss was observed when melting under an atmosphere. In addition, due to concerns of carbon contamination from the graphite substrates, a batch of 20 Fe-B samples created on copper and a batch of 20 Fe-B samples

created on graphite, all created from the same ingot, were analyzed using the MPC's Leco CS-444 Carbon/Sulfur determinator for variations in carbon content. The difference between the arc-melted ingot, the copper processed spheres, and the graphite processed spheres was found to be on the order of 1 ppm.

The same instrument was used to test if there was any stochiometry shift in the Fe-C samples, comparing the arc-melted ingot and the sample that had been held in the liquid state in the NESL for ∼20 minutes. The weight percent carbon of the ingot was determined to be 4.19%, corresponding to 17.04 at%, and repeated measurement established a compositional variability in the ingot of +/- 0.05 wt%. The processed sample was determined to be 4.19 wt % carbon, corresponding to 16.9 at%. Given the small amount of mass available to test compared to the recommended mass for the instrument, this variation was considered within the margin of error.

The composition of a prepared Fe-B ingot was measured in bulk by inductively coupled plasma mass spectrometry (ICP-MS). A composition of 82.9 at.% iron, 17.1 at.% boron was determined over a number of samples, with a standard deviation of 0.2 at.%. The composition of a sphere processed in the BESL during the experiments for the results in Chapters 4 and 5 was determined to be 82.55 +/- 0.2 at.% Fe after levitation processing.

2.2 Electrostatic Levitation

2.2.1 The Levitation Mechanism

All ESL systems share the same basic operational design principles. A set of conducting electrodes provide the levitation control. While early iterations of the system relied solely on large, curved top and bottom electrodes to provide both the levitation force and a stabilizing lateral restoring force, current systems incorporate two sets of orthogonal lateral electrodes, each set consisting of a grounded electrode and an electrically isolated electrode. The WU-BESL and NESL use hemispherical top electrodes, while the ISU-ESL electrode set is composed of copper cylinders, primarily to minimize the electrode filling factor when using the TDO system, and can be seen in Fig. 2.1. The top electrode has a shaft drilled through it to allow samples

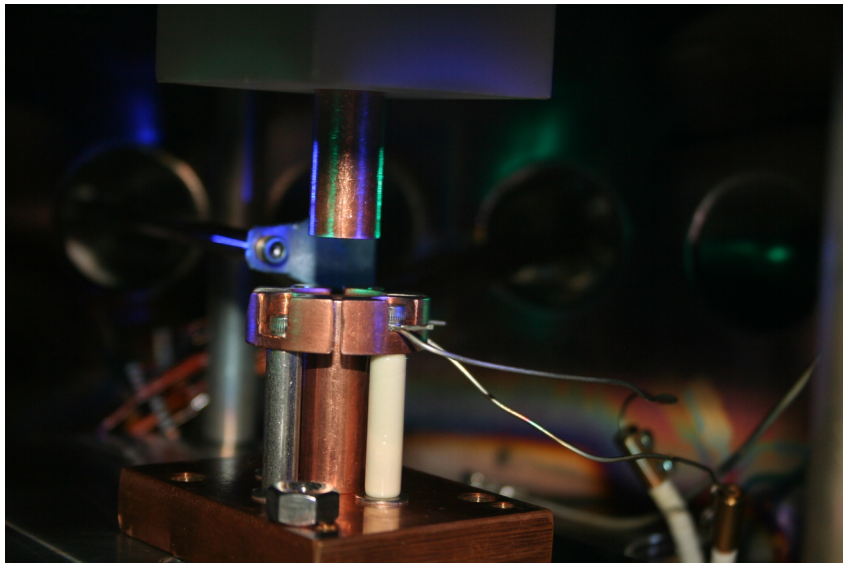

Figure 2.1: Electrodes currently installed in the ISU-ESL.

to drop down from a carousel above; the bottom electrode has a similar shaft to enable the vertical translation of a copper sample post. This post controls the initial vertical position during the launch, an important parameter to attain stable levitation.

The top electrode is isolated electrically by a large Macor block and connected to a Trek model 20/20c amplifier, capable of a slew rate of 450 kV/ms and operating between 0 and 20 kV. The ungrounded lateral electrodes are placed on Steatite standoffs and each is connected to an individual amplifier outputting between -5 kV and 5 kV. When the electrodes are turned on, a sample sitting on the grounded bottom electrode is capacitively charged and achieves levitation when the electrostatic force is sufficient to overcome gravity such that $F_{\mathrm{E}} = mg$.

Earnshaw's theorem[101] states that there can be no stable minimum in 3D from a collection of static charges, and so to maintain a stationary sphere an active positioning system is required. The positioning instrumentation is arrayed as shown in Fig. 2.2. Two orthogonal LED sources, centered at 455 and 505 nm, are each aligned with one of the sets of lateral electrodes. Each LED is centered on the levitation gap, and focused slighly behind the levitation position so that the beam is roughly the same size as the gap when it hits the sample. As the LED is a divergent light source, two bi-convex spherical singlet lens as seen in Fig. 2.3 focus the

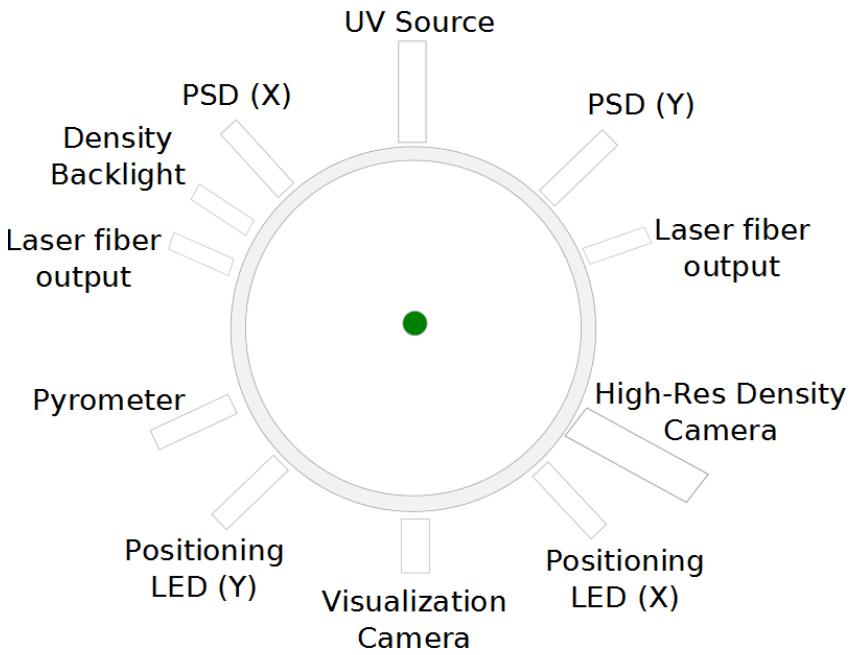

Figure 2.2: Top view schematic of the ISU-ESL furnace and surrounding instrumentation.

beams just behind the sample, projecting a shadow. This shadow is cast onto position sensitive detectors (PSDs) and is converted into two voltages indicating lateral and vertical position. The signal is converted via an analog to digital converter and sent to the target computer, an independent PC running the control algorithm.

The algorithm operates at 500 Hz, a limitation of the National Instruments DAC, and is derived from the gain-scheduled control scheme described in Ref. [102]. The Matlab-controlled algorithm is based on two linear models (horizontal and vertical positioning) and uses an LMI-based pole region assignment to determine three parameters, similar to those of a PID algorithm, for each direction. These are input by the user during construction of a sample algorithm, and affect system behavior such as initial launch time and equilibrium settling time. An individual algorithm is built for each sample, with the primary inputs being the mass and radius of the sphere, which determine a series of gains between the output of the PSDs and the corresponding amplifier voltage signal.

The high voltages present are capable of causing dielectric breakdown if an atmosphere is present at a sufficient pressure as seen in Fig. 2.4. At low pressures, the mean free paths of the

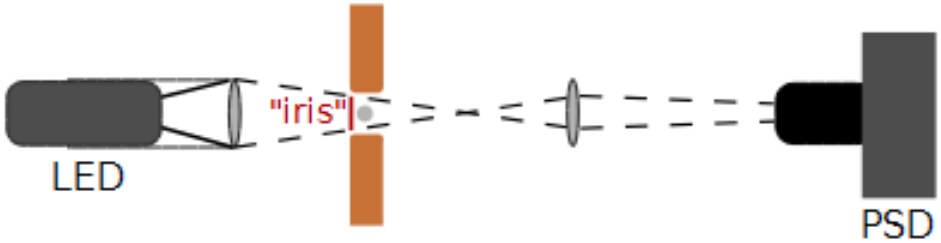

Figure 2.3: The core of the positioning system. The "iris" size for LEDs is indicated as a red line.

gas molecules are sufficiently larger than the chamber such that collisions are prevented, while at high pressures, the mean free path is low enough to prevent the accumulation of kinetic energy required for ionization. In addition, the possible interaction with residual gas phases may cause oxide formation or otherwise inhibit the undercooling desirable for levitation studies. As a result, the ESL system is operated under high vacuum conditions, driven by a rotary vane pump and a turbomolecular pump. The levitation system is not operated above 5x10^{-6} torr; processing generally begins at 5x10^{-7} torr, a compromise between pump time ($\sim$ 1/2 hour) and oxygen partial pressure. The baseline pressure of the system is currently 9x10^{-9} torr.

The ISU-ESL is optimized for samples massing between 30 and 70 mg, with densities in the region of 5 to 7 g $cdot$cm^{-3}. Samples have been processed with densities as low as 2.3 g $cdot$cm^{-3} and as high as 16 g $cdot$cm^{-3}. In theory, any sample shape can be levitated; in practice, highly irregular, asymmetric shapes acquire an uncontrollable multi-axial spin very quickly. Spheres are the easiest shape to process, as well as being the typical shape after levitation solidification, so all samples are prepared as spheres. The only strict material requirement is a high enough conductivity to capacitively charge during launch.

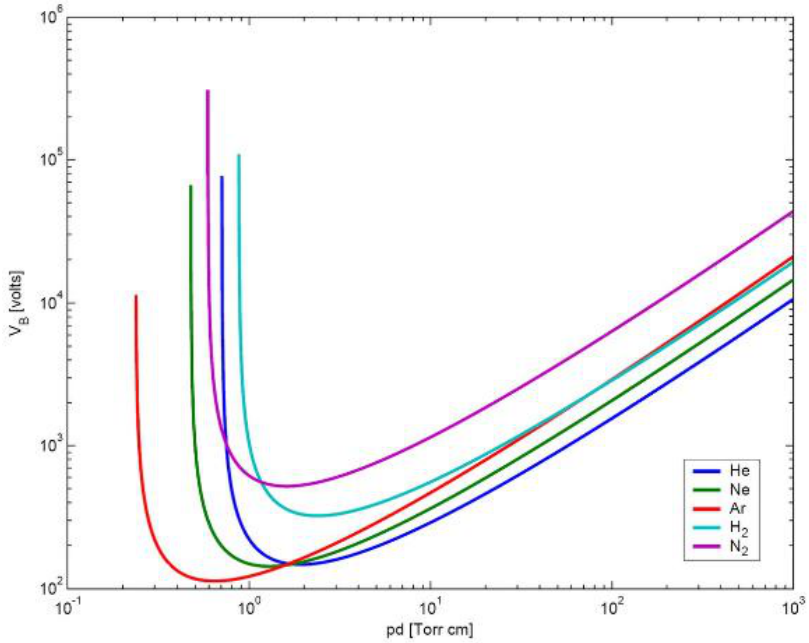

Figure 2.4: A Paschen curve detailing the voltage required to produce dielectric breakdown.

2.2.2 Sample Heating

Once the sample is levitated, it is heated bi-directionally by the fiber coupled output of a watercooled Apollo Instruments laser diode. The laser is nominally centered at 980 nm, with a bandwidth of approximately 8 nm. While initially only one fiber output was used, it was found that the radiation pressure from the laser at high power would push the sample out of the center of the levitation gap, and thermal gradients would establish across the sample, so a second fiber output was installed. The laser focusing optics were designed in house and allow a spot size on the sample of 1 to 4 mm[62]. Alignment is performed via a low power pilot beam incorporated into the laser. The fiber mounting mechanisms also allow deliberate misalignment of the lasers to the side, inducing or damping a rotational spin via radiation pressure[103]. While in the ISU-ESL lab this is primarily used to maintain spinning frequency so that sample stability is not affected and to avoid sample bifurcation, other ESL groups use this capability for creep measurements[76].

The lasers themselves are controlled via a LabVIEW interface. The laser may be controlled manually, by specifying an output power, or in an automatic ramp mode. A PID algorithm

was implemented for the purpose of controlled ramps. After tuning, the heating rate can be adjusted to less than 0.1 K/s, while the maximum rate is dependent on the response of the sample but may be on the order of ∼100 K/s. The cooling rate is limited on the upper end by the ability of the sample to cool radiatively according to

$$mc_p \frac{\mathrm{d}T}{\mathrm{d}t} = -\epsilon A_\mathrm{s} \sigma_\mathrm{B} (T^4 - T_0^4) \tag{2.1}$$

where m is the mass of the sample, c_p is the specific heat, ϵ is the hemispherical emissivity described below, A_s is the surface area, σ_B is the boltzmann constant, and T_0 is the ambient temperature in the chamber. In practice, this limits the cooling rate during solidification to 15-30 K/s, dependent on the sample and melting temperature, and to rates on the order of 2-5 K/s well below the melt. All initial processing must be performed manually since, when first heated, samples tend towards instability and are extremely sensitive to the slightest changes in the input power.

Heating with the laser has the effect of both outgassing any adsorbed gasses from the sample as well as causing evaporative mass loss. Since the sample is isolated, this causes charge loss, a corresponding increase in the levitation voltage, and can lead to levitation instability and sample dropping. At high temperatures ($>$ 1000°C), thermionic emission becomes efficient enough to offset charge losses at a rate given by the Richardson-Dushman equation

$$j = AT^2 \exp(-\frac{\phi}{k_\mathrm{B} T}) \tag{2.2}$$

where j is the thermionic emission current, A is a constant (120 A cm^{-2}K^{-2}), and ϕ is the Boltzmann constant. At 1500 K this yields a value on the order of 1 nA [62] which, given the charge of the sample is on the order of 1 nC, is a powerful effect. This is ineffective at low temperatures, however, and alternative methods are required for sample charging. Several groups overcome this transition region by melting the samples prior levitation and launching them in a liquid state [73]. This has the downside of introducing post contamination, as well

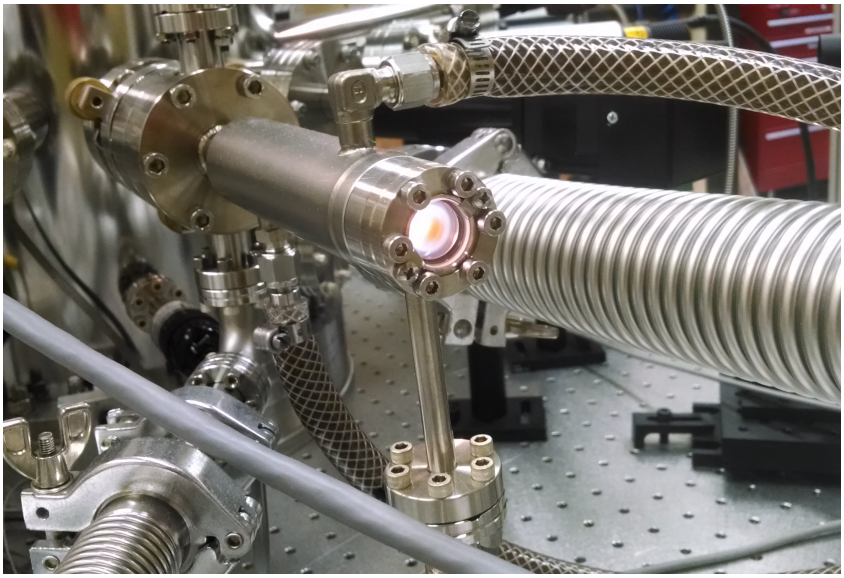

Figure 2.5: The HIS13 helium discharge lamp, properly ignited.

as a certain "stickiness" to the post due to surface tension, and the ISU-ESL group has not perfected the technique yet.

Instead, the ISU-ESL uses an Omicron HIS13 helium discharge lamp as a source of UV photons to induce sample charging via the photoelectric effect. The lamp, pictured in Fig. 2.5, features a watercooled ignition chamber with a constant flow of 99.9999% purity helium gas, through which a set of high voltage electrodes induce an arc. The resulting plasma emits primarily at the He I line, with an energy of 21.2 eV (∼60 nm). Most elemental work functions are on the order of 4-6 eV, and so this photon energy is more than adequate for efficient charging, and, as described in [62], serves to increase the efficiency of charging by a large increase in the number density of excitable electrons. As the top electrode is negatively charged and a levitated sample thus positively charged, ejected electrons have the effect of lowering the required levitation voltage to an equilibrium voltage, derived in [62].

A thin capillary guides the emitted light from the ignition chamber to several centimeters from the levitated the sample and reduces the potential of evaporated material making its way into the UV source and contaminating the chamber. A stepper-driven shutter mechanism enables shielding for the capillary once volatile samples have reached the thermionic region.

The speed of processing samples is limited by the ability of the UV source to recharge the sample after charge loss events. To maintain the high purity conditions required for optimal ignition, the UV system requires its own differential pumping system, provided by a separate rotary vane rough pump and a small turbo pump.

The evaporation of material at high temperatures poses a significant constraint on material choice for the ESL. The Langmuir molar flux equation, which describes an evaporation rate $\dot{m}$, may be modified as in Ref. [104] to describe the evaporation of an n component alloy over time t. The total evaporation of each component i, having vapor pressure P_v, i and molecular weight M_i, is given by

$$\sum_i^n \int_0^t \dot{m}_i dt = \sum_i \int_0^t \frac{\alpha A a_i (P_{v,i} - P_{\mathrm{ref},i})}{\sqrt{2\pi M_i R T(t)}} dt \tag{2.3}$$

where a_i is the activity, A is the molar surface area of component i, $P_{\mathrm{ref},i}$ is the reference pressure, R is the gas constant, and $T(t)$ is the temperature in kelvin as a function of time. α is a constant to correct for deviation from an ideal vacuum, where it would be unity, and is frequently empirically determined. In practice, an ideal mixing approximation is applied, and the concentration of component i, c_i, is substituted for a_i for quick feasibility calculations, though this tends to overestimate evaporative losses and is only a rough guide.

While the ISU-ESL is operationally very robust against evaporation, in one case processing a single $Al_7Pd_7Mn_2$ sample long enough to evaporate >10 mg of material, the WU-BESL requires frequent cleaning during operation. In both systems, glass slides are installed in all viewports, in order to ease cleaning of evaporated metals. However, the principle concern is not operation, but stochiometry shift, as components of an alloy frequently have different vapor pressures. It is critical to choose materials that have low vapor pressures, and to consistently check the mass of the sample before and after processing.

2.2.3 Pyrometry

Sample temperature is measured via optical pyrometry. Blackbody radiation is emitted from a material according to the well known Planck's law:

$$I(T,\lambda) = \frac{2hc^2}{\lambda^5}(\frac{1}{e^{\frac{hc}{\lambda k_{\mathrm{B}} T}}} - 1) \tag{2.4}$$

Single color pyrometers, such as the ones in use in the ISU-ESL (Metis MI16 from 300°C to 1300°C, and HI16 from 700°C to 2300°C), sample one particular wavelength (1.6 μm in the ISU-ESL) and relate the measured intensity to the temperature according to

$$I(T,\lambda) = \int_{\lambda_1}^{\lambda_2} \epsilon(T,\lambda)\frac{2hc^2}{\lambda^5}(\frac{1}{e^{\frac{hc}{\lambda k_{\mathrm{B}} T}}} - 1)d\lambda \tag{2.5}$$

where $\epsilon = \epsilon(T,\lambda)$ is the wavelength dependent emissivity of the material, ranging from 0 to 1. Single color pyrometers depend heavily on the assumption that the (user-entered) emissivity is not strongly temperature dependent, a belief which often proves to be true. The emissivity is highly dependent on surface conditions and may change dramatically based on surface texture or the presence of oxide impurity phases. In the particular case of levitation work, the sample is not in a fixed position, and depending on the stability of the particular system, lateral and vertical instability may also affect temperature readings. Instrumental error on the MI16 and HI16 can be estimated as 0.1% of the signal under 1000 °C, and 0.5% above. The pyrometers used in this work acquired data at 10 Hz, but are capable of acquiring up to 100 Hz.

As the emissivity is an unknown quantity and is difficult to measure directly, generally obtainable in the form of $c_p(T)/\epsilon_T(T)$[74, 105], the pyrometer emissivity is typically recalibrated by comparing transition temperatures measured by the pyrometer to known transition temperatures from the literature or calorimetric techniques such as DSC. This transformation can be applied quickly and easily such that the emissivity may be recalculated according to

$$\epsilon'_\lambda = \epsilon_\lambda \exp(\frac{hc}{\lambda k_{\mathrm{B}}}(\frac{1}{T'_{\mathrm{tr}}} - \frac{1}{T_{\mathrm{tr}}})) \tag{2.6}$$

where T'_{tr} and T_{tr} represent the verified transition temperature and that observed experimentally, respectively. This yields a new temperature T' determined by

$$T' = (\frac{1}{T} + \frac{k\lambda}{ch}\ln(\frac{\epsilon'_\lambda}{\epsilon_\lambda}))^{-1} \tag{2.7}$$

Two-color pyrometers, such as those in use on the BESL and NESL, sample two wavelengths and compare the ratio using

$$T = \frac{hc}{k_\mathrm{B}}\frac{\lambda_1 - \lambda_2}{\lambda_1\lambda_2}\ln(\frac{\omega_1\lambda_1^5\epsilon_2}{\omega_2\lambda_2^5\epsilon_1})^{-1} \tag{2.8}$$

which mitigates the need for extensive calibration. Two-color pyrometers have been shown to correct many of the shortcomings of single color pyrometers [106]. However, on occasion, the ratio measurement erroneously covers signals that may be present in the single-color reading, such as seen in Fig. 2.6. There, a structural transition was identified through the corresponding x-ray data as occuring during the solidification plateau. The ratio signal exhibited a small signal, but largely overcorrected for the discrepancies in the individual wavelengths, K1 and K2. The single color output showed a much clearer event, resembling a double recalescence.

Finally, a Thorlabs CMOS color camera, with a sensor resolution of 1280x1024, is used in combination with magnification optics for sample visualization. While this is useful to observe the stability of the sample and as an indication of a sample melting, it is best for observing the surface of the sample, with particular regards to oxide and impurity phases.

Pictured in Fig. 2.7 is a levitated liquid AlPdMn sample featuring a large oxide patch, easily visible in the image. Depending on the material, extended high temperature processing at high vacuum is sometimes enough to clean these phases, at the cost of potential stochiometry shift; Fig. 2.8 is the same sample, held at a higher temperature. In this way sample cleanliness can be easily monitored during an experiment.

2.2.4 Density Measurements

Density measurements in the ESL use the machine vision method described in Ref. [79] The sample is backlit by a violet (405 nm) LED source similar to the positioning LEDs, and

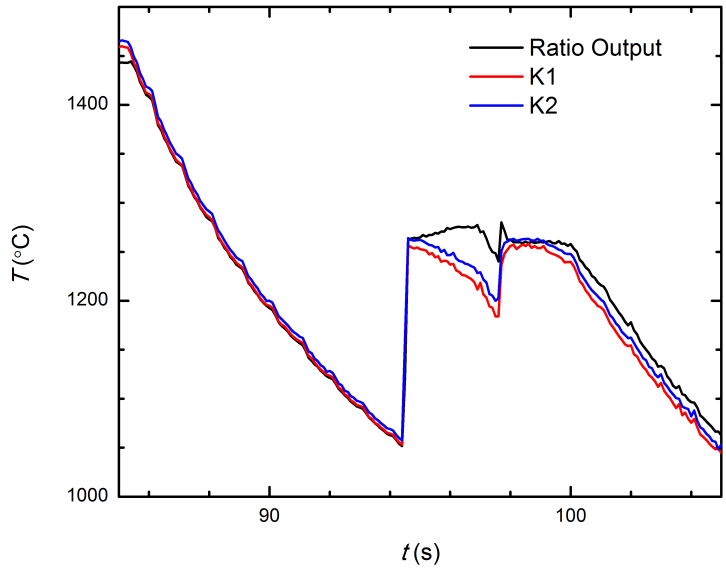

Figure 2.6: The temperature data from a two color pyrometer on the WU-BESL during solidification of a $Ni_{50}Zr_{50}$ sample. A structural transition during the solidification plateau could be interpreted as noise in the ratio output (black), but the two individual color readings, K1 (red) and K2 (blue) show a clear second recalescence event

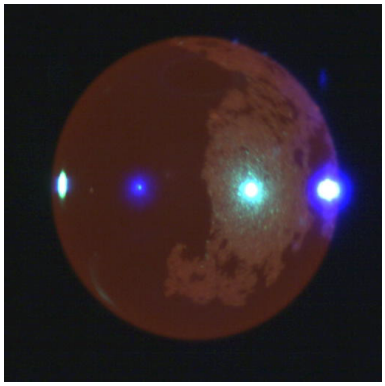

Figure 2.7: An AlPdMn sample, with a significant oxide phase

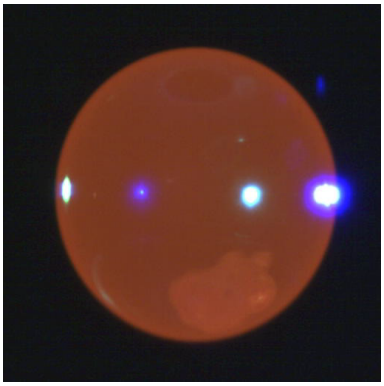

Figure 2.8: An AlPdMn sample after a high temperature hold

video of the sample taken by a high resolution monochrome camera (Pixelink PL-B741) with a corresponding bandpass filter. An Infinity K2 telephoto lens provides high magnification and enables a resolution of approximately 3 μm/pixel. The contrast between the sample and the surrounding background is used to define the cross-sectional area of the sample. An integration proceeds either by numerical methods or approximation by legendre polynomials. To obtain absolute units the calculated volume is compared to a well defined calibrant, for which the ISU-ESL laboratory uses Grade 3 tungsten carbide spheres from McMaster-Carr. Tungsten carbide is chosen as it is unlikely to deform during sample manipulation; stainless steel is also acceptable.

The method relies on the sample possessing azimuthal symmetry so that a rotational integral may be performed. This assumption generally holds well for liquids, where surface tension will force the material into an ellipsoid with a very slight elongation in the z direction. In cases where the spin of the sample is uni-axial, deformation in the lateral direction may also occur, but preserve azimuthal symmetry. With a large multi-axial spin, the deformation will occur along a diagonal axis and break the symmetry, making the volume calculation unreliable. Unless specifically machined for low grade sphericity, even levitation-solidified spheres have notable surface roughness, and small inhomogeneities on the surface will cause large errors in the volume integration.

The precision of the method, as applied to grade three WC spheres, is approximately 0.04%[62]. When properly calibrated with a low-grade calibrant sphere, this technique will have an error as low as 0.1% when studying liquids, with much of this coming from uncertainty regarding mass loss during the experiment. When applied to solid spheres in the ESL, the error becomes 1% to 2%, depending on surface conditions on the sample.

2.3 Magnetic Measurements using a Tunnel Diode Oscillator

There have been numerous attempts to integrate resistivity and dynamic susceptibility measurements into containerless processing environments. For instance, the JAXA ESL system[75] integrated a series of asynchronous electromagnetic rotors to induce rotation in a liquid sample, requiring precise measurement of the rotation of a featureless liquid, a complication that

limits the utility of the technique. EML systems have attempted to measure the conductivity of liquids through the use of an additional transformer coil, an approach challenged by sample deformation and positional variation with temperature[107]. Measurements of magnetic susceptibility in EML and CNL are often carried out simply by placing a CoSm permanent magnet near a levitated sample and measuring either the ensuing deviation from the levitation axis as a function of temperature or the force on the magnet, creating a Faraday balance.

The approach to magnetic measurements in the ISU-ESL focused on the integration of a tunnel diode oscillator (TDO) into the levitation chamber. Traditionally a low-temperature technique, the TDO functions as a highly sensitive radio-frequency probe of resitivity, magnetic susceptibility, and London penetration depth[108–110]. It consists of an LC tank circuit driven by a tunnel diode, a special p-n junction that may be biased to a region of negative resistance.

The interaction of the circuit with a spherical sample in the AC field of the inductive coil may be understood by closely following the derivation laid out in Refs. [62, 93]. The resonant frequency f_0 of the TDO circuit is given by

$$f_0 = \frac{1}{2\pi\sqrt{LC}} \tag{2.9}$$

Any change ΔL in the inductance of the resonator coil by, for example, placing a sample inside of it, shifts the resonant frequency by Δf as given by

$$f_0 + \Delta f = \frac{1}{2\pi\sqrt{(L+\Delta L)C}} \tag{2.10}$$

The impedance of an AC circuit is given by $Z = R_0 + i\omega L$. With a sample of complex susceptibility $\chi = \chi' + i\chi''$, changes in the impedance of the coil may be related to the sample by

$$\frac{\Delta L}{L_0} = \phi\chi' \tag{2.11}$$

$$\frac{\Delta R}{R_0} = -\frac{\omega L_0}{R_0}\phi\chi'' \tag{2.12}$$

where ϕ is the sample filling factor. Using the derivations in [111], it may be shown that the real part of the susceptibility χ' is given by

$$\chi' = -\frac{3}{2} + \frac{9\delta}{4a}(1+\chi) \tag{2.13}$$

where the skin depth $\delta = \sqrt{2\rho/\mu\omega}$, and ρ is the sample resistivity. This leads to a final expression for the frequency shift given by

$$\frac{\Delta f}{f_0} = \frac{3}{4}\phi(1 - \frac{3}{2a}\sqrt{\frac{\rho}{\pi f_0 \mu_0}}\sqrt{1+\chi}) \tag{2.14}$$

2.3.1 Adaption for the ISU-ESL

The integration of the TDO circuit into the ISU-ESL required placing the pickup coil close to the sample, remaining electrically isolated, and not interfering with the line of sight required for the optical instrumentation. Further, traditional TDO measurements are performed at low temperatures, often between 4 and 170 K, and require mK stability. By contrast, the melting temperatures required for the solidification studies of interest to the ISU-ESL laboratory are commonly between 1300 K and 1800 K. Thermal fluctuations in the inductive coil dramatically increase the level of noise in the signal through altering the resistivity of the copper. Therefore, any such system installed in the ESL required careful thermal management. At the same time, given that the sample could not be placed directly inside the coil, the filling factor needs to be maximized by keeping the coil as close to a levitating sample as possible. The effect of fluctuations in sample positional stability on the coil measurement also drove an upgrade of the positioning system from a HeNe laser based system to the high powered LEDs described above[62, 93].

A detailed examination of the instrumentation involved in the implementation of the ISU-ESL TDO may be found in Ref. [93, 62]. The bottom electrode was replaced with a hot pressed Boron Nitride (BN) cylinder, chosen for its excellent thermal conductivity. The pickup coil was wound around a groove in the cylinder near the top, leaving a 'lip' to provide a measure of shielding. The coil was potted with an epoxy to ensure thermal transfer with the BN. The passive cooling power of the BN and copper baseplate were not sufficient to stabilize the coil against radiative heating from a molten sample, so an active temperature management scheme was implemented. A nichrome heating wire is wound 1.5 cm below the inductive coil in order to maintain the temperature above ambient conditions. The temperature of the inductive coil is monitored with a platinum resistance temperature detector (RTD). A Lakeshore Model 331 Temperature Controller then stabilizes the temperature of the coil at a particular setpoint - typically 350 K - using a carefully tuned PID algorithm.

The gate time on the frequency counter is set to 1 second, to reduce noise in signal. Crucially, this limits the ability to resolve the temperature dependence of any signals in the TDO output according to the heating or cooling rate of the sample. Typical sample freecools may have cooling rates on the order of 10 K/s at high temperatures, and so whenever possible, controlled ramps are preferred.

Initial calibration was performed by heating the TDO with the heating laser, reflected from a mirror mounted onto the top electrode[93]. It was found that the frequency shift exhibited by the coil in response to temperature drift was approximately 200 Hz / K. The frequency is corrected for thermal drift using the coil temperature and heater power by

$$\Delta f' = \Delta f - A\Delta T_{\text{coil}} + B\Delta P_{\text{coil}} \tag{2.15}$$

where A and B are empirically determined constants. For the results presented in Chapter 4, where only the large frequency shifts associated with magnetic transitions were of interest, the coil was slowly heated($\sim$0.1K/min) from 340 K to 360 K using the nichrome heating element and cooled back to 340 K with no sample in the gap. B was set to zero, using only the second term in Eq. 2.15, which was sufficient to remove any signals clearly associated with

rapid temperature changes. However, at high temperatures, determined by Rustan[93] to be above 1700 K, the radiative heating of the electrodes from the sample (and the corresponding shift in the resistivity of the copper electrodes) begins to affect the background signal in a way that is much more difficult to model.

In typical TDO measurements, the sample is placed inside the coil, and ϕ is given by $V_{\text{sample}}/V_{\text{coil}}$. In the ESL, as the sample is located outside the coil in an inhomogenous field, the filling factor must be determined empirically using well characterized standards, here copper. The resistivity was measured through the well characterized zirconium *hcp*-*bcc* transition, and used to calculated a conversion rate of 3.5 Hz/$\mu\Omega$ cm. By contrast, the ferromagnetic transition in a low-carbon steel ball bearing (McMaster-Carr 96455K49, *bcc* Fe $T_C = 1043$ K) produced a frequency shift of 3370 Hz. Thus while careful calibration for temperature drift and a sufficiently slow heating/cooling rate is required for resistivity studies, the frequency shifts associated with ferromagnetic transitions have a magnitude much larger than typical temperature effects or noise associated with the circuit.

2.4 Scattering Measurements

The advent of third generation synchrotron light sources and high intensity neutron facilities has spurred the development of a number of containerless processing furnaces aimed at the study of high temperature liquids and metastable solid phases. These systems enable *in-situ* study of solidification processes and transient phases challenging to probe by more traditional means.

While the development of ESL furnaces for thermophysical measurements began in the 1980s, it was not until the early 2000s that the technique was widely adapted for scattering environments[87, 112, 113]. NASA's own BESL system was used for initial studies of liquid metals and the nucleation barrier [86], as well as structural modeling of deeply undercooled liquids [114]. The success of these studies helped spur the development of the Washington University Beamline Electrostatic Levitator (WU-BESL), which first acquired data in 2010. Concurrently, a complex, unique ESL system was designed to fit the requirements of neutron TOF studies at the Spallation Neutron Source at Oak Ridge National Laboratory. The Neutron

Electrostatic Levitator, or NESL, performed its first commissioning run in 2013, and the first publishable data from the instrument was obtained in late 2014 [91, 92].

The BESL was used by the ISU-ESL group first in 2013 to obtain much of the x-ray data for Chapter 3, and then again in 2016 for the studies presented in Chapters 4 and 5. A significant effort during the course of this dissertation was spent on ensuring the NESL was operational and reliable, and the liquid data taken on the NESL and presented in Chapter 5 represents some of the first data obtained from the instrument.

2.4.1 High-energy x-Ray scattering

Diffracted x-rays obey the well known Bragg relation, given by $n\lambda = 2d\sin\theta$, wherein n is an integer, λ is the wavelength of incident x-ray, d is the plane distance, and θ is the angle of scattering. The scattering process may be characterized by the momentum transfer, $Q = k_f - k_i$, where k_i and k_f are the incident and scattered wavevectors, respectively. In this work, only elastic scattering is considered.

X-rays scatter from the electron cloud, and each element has a Q-dependent profile, denoted the atomic form factor $f(Q)$, as a fourier transform of the spatial distribution of the electron cloud. A direct consequence of this is a decrease in scattering intensity at large Q. Another consequence of this is a general insensitivity to light elements relative to larger, heavier atoms; near $Q = 0$, $f(Q) \sim Z$.

Diffracted x-rays may be used to establish the structure of a material or identify what known structures are present. While available in a wide range of energies, all x-ray scattering in this dissertation was performed using high-energy x-rays ($E > 100$ keV), providing a significant penetration depth and thus excellent transmission through typical ESL sized samples, as well as a small enough scattering cone to collect a large region of Q-space at high speed on simple 2D detectors. This is important to the work in Chapter 5, as a large Q range is critical to obtaining the accurate fourier transformations required to generate a high quality pair distribution function, an important tool for the understanding of non-crystalline materials. Much of the design of the BESL scattering environment was optimized for studies of this type.

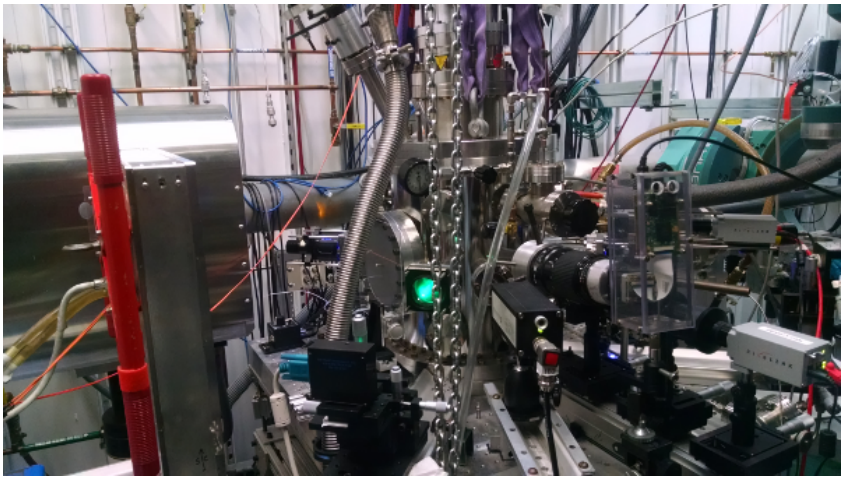

Figure 2.9: The BESL as installed at Beamline 6-ID-D. The GE 40RT Revolution 2D detector is pictured to the left.

2.4.2 BESL

The ISU-ESL was based on the design of the BESL, and the vacuum chamber itself is a near-carbon copy, pictured in Fig. 2.4.2. The system was designed for easy integration into Beamline 6-ID-D at the Advanced Photon Source (APS) with the possibility of further work at Beamline 1 for small angle scattering (SAX). A few key design choices differentiate the two systems.

Due to the time constraints associated with beam-time and the safety requirements of operating in an x-ray hutch, motorized carousel and post mechanisms were included in the BESL. The carousel is capable of holding 32 samples, which drop through the top electrode, and is driven by an external stepper motor. The motor mechanism for the post additionally allows later sample "kicking" by raising the post into the PSD path during levitation.

The original UV source for the BESL was a deuterium arc lamp. The photon energy was 7.8 eV (∼160 nm) and had a large, unfocused spot, leading to inefficient charging. Following the success of the integration of the HIS-13 into the ISU-ESL, the BESL was updated with the same model. However, during the 2013 studies the deuterium lamp was still installed on the BESL to counteract x-ray charging difficulties. Long exposure to high energy x-rays charges

the sample to the point of levitation instability, and so the deuterium lamp shutter was opened, charging the electrodes and effectively raising the levitation voltage.

The access flange was replaced by a beryllium window to reduce secondary scatter effects and optimize transmission. Critical to obtaining the high framerates necessary for thermal cycling and rapid acquisition of isothermal liquid scans was the implementation of a 2D x-ray detector. A GE 4RT Revolution amorphous silicon area detector was placed close to the exit port of the BESL (working distance $\sim$ 500 mm). At the x-ray energies used ($\lambda = 0.094$ Å, $E = 131$ keV), this enable acquisition up to $Q \sim 22\text{Å}^{-1}$. The detector was operated at full resolution (2048 x 2048) at between 1 and 8 Hz for measurements presented here. Some attempts were made at higher framerates for solidification studies, but firmware issues and the limited downtime during the experiment made this impossible.

The high-energy x-ray capabilities of the Advanced Photon Source (APS) at Argonne were used for all x-ray measurements. High-energy is necessary to provide sufficient transmission through the sample; at the operational energies used in this work, between 85 and 90% of the x-ray intensity was transmitted through the sample, enabling bulk structural measurements. A high flux is needed for the rapid acquisition needed for solidification events; solidification of a 2 mm sample can happen in seconds or less, and when the sample is freely cooling at rates upwards of 10 K/s a high framerate is needed for reasonable temperature resolution. The flux at beamline 6-ID-D using the superconducting undulator was $\sim 5\text{x}10^{11}$ photons/second.

Initial experiments during the 2013 BESL run found a sample processing success rate of approximately 15%, with most samples lost on launch or floating in a wildly unstable manner, either positionally or with the voltage, during processing, until they were lost in the chamber. The sample stability during the 2016 run was dramatically improved by some algorithmic optimization as well as improved methodology for keeping the electrode spacing consistent during chamber opening and cleaning. Launching and processing were subsequently successful almost 80% of the time.

Samples were heated through the melt into a liquid and held at a constant temperature just above the melt. Diffraction patterns were obtained in 30 s increments at 1 Hz. The temperature was increased in a step-wise fashion, taking 30 s increments every 50 degrees, until the maximum

desired temperature, before the process was repeated on cooling. Samples were freely cooled according to by turning the laser off, and some attempts were made at controlled cools by manually tuning the laser power in a decreasing fashion. As of the experiments included in this dissertation the BESL had no implementation of automatic temperature control.

2.4.3 Neutron Scattering

While interpretation of a diffraction pattern obtained from neutron scattering remains fundamentally the same as those obtained from x-ray, there are several important differences between the probes that may be leveraged for the characterization of levitated materials.

For one, even a powerful source such as the SNS produces a lower flux of neutrons than may be obtainable at a synchrotron light source such as the APS ($\sim$1 x 10^8 neutrons cm^{-2} sec^{-2} at NOMAD vs $\sim$1 x 10^{11} photons cm^{-2} sec^{-2}, respectively). The interaction cross section for neutron scattering is also significantly smaller. While x-rays primarily scatter from the electron cloud, neutrons scattering occurs primarily from the atomic nuclei. The typical atomic nucleus is several orders of magnitude smaller than the electron wavefunctions. As the atomic form factor $f(Q)$ is derived from the fourier transform of the density distribution of the scattering element, the form factor for neutrons appears as a nearly flat line.

In addition, due to the strong dependence on nuclear scattering, different isotopes possess a different coherent scattering length $< b >$, enabling the application of isotopic substitution to vary the contrast between various elements in a scattering pattern. For the purposes of liquid scattering, isotopic substitution allows easier derivation of experimentally observed partial pair correlation functions.

2.4.4 NESL

While some ESLs have been developed for neutron beamlines in the past 10-15 years, they tend to be limited to reactor sources, and more of an adaption of a traditional ESL design than a radical redesign. The installation of a levitator into the beamlines at a pulsed neutron source such as the SNS required just such an endeavor. The implementation of a complex ESL system in a neutron environment requires a number of design modifications and compromises,

for neutron safety, scattering optimization, and for optimized use of the system despite the radiation hazards involved.

The NESL was commissioned in 2010 as a levitator designed to fit into the beamline wells at the Spallation Neutron Source at Oak Ridge National Laboratory. The original plan was to integrate the system into three beamlines: the Nanoscale Ordered Materials Diffractometer (NOMAD) at BL1B for elastic measurements, the Wide Angular-Range Chopper Spectrometer (ARCS) at BL18 for inelastic scattering, and the Backscattering Spectrometer (BASIS) at BL-2. Commissioning at VULCAN was carried out as a viability test in early 2013. Commissioning at NOMAD was first attempted in late 2013, but during the two week beamtime no samples were successfully melted. After a significant effort from the most junior members of the WU and ISU ESL groups to revamp and repair the system, a successful run was accomplished in late 2014. The system has since had several successful runs at both NOMAD and ARCS.

The system is the most complex of the NASA derived electrostatic levitators. The beamline detector tanks operate between 10^{-3} torr (NOMAD) and 10^{-7} torr (ARCS), so the entire sample environment is designed to be lowered into a high vacuum environment. The differential pumping system, water-cooling, and helium gas lines all route to a UV source, idential to the ISU-ESL lamp, that sits inside the detector chamber. The vacuum environment of the detector chambers, combined with the unobstrocted scattering path to the sample needed for high-Q measurements with comparatively low energy neutrons, necessitate a radical redesign of the positioning, heating, and thermophysical measurement components. All instrumentation is mounted vertically, and a system of mirrors was constructed to enable line of sight to the sample. In order to not interfere with neutron scattering, the UV source is mounted at an angle, and the capillary is aimed at the sample from below. The entire lower section of the chamber, denoted the tailpiece, is constructed of aluminum, and much of the area is covered by a thin 1/16" aluminum window. The middle section of the levitator, featuring the electrode assembly and mirror platforms, is designed to lift out of the tailpiece independently, allowing the chamber to open up mid experiment without venting the detector tank.

While in both the BESL and the ESL, all alignment is performed by hand, the geometry required necessitates that all optical components are inaccessible during the experiment, and

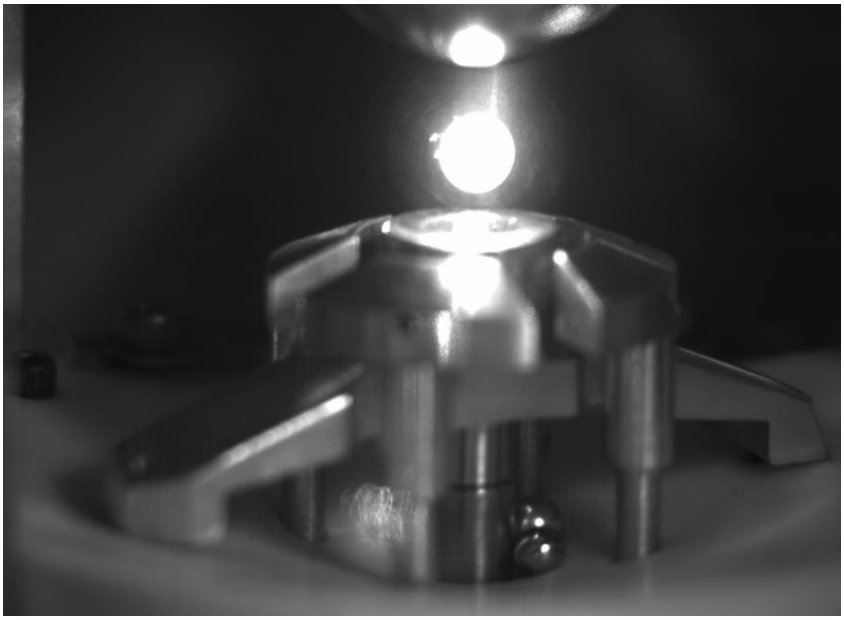

Figure 2.10: A sample being heated in the NESL. Notably, the entire bottom area of the picture is filled by the sample catcher assembly, enabling easy sample retrieval.

so the PSDs are placed on motorized stages. The post is motorized, with all wiring routing through the lower flange. The carousel is also motorized, connected by a drive shaft to an external stepper motor placed near the turbo. The complexity of the interior mechanics, optics, and electronics, added to the difficulty of replacing flanges under permanent optical mounts, leads to a large rate of outgassing and possible leaks, both virtual (from trapped gasses or surface outgassing) and real. The pump time is typically on the order of 6 to 8 hours until low 10^{-6} torr and 12 to 16 hours until mid 10^{-7} torr.

Critically, the lower interaction cross-section of neutrons compared to x-rays as well as the lower flux of neutrons produced require both significantly longer measurement times as well as larger samples for good statistics. The system uses a 30 kV amplifier instead of the standard 20 kV. The NESL is thus optimized for samples near 350 mg. Two separated lasers, each capable of a maximum of 110 W and operating at 980 nm, heat the levitated samples bi-directionally.

Finally, the bottom of the tailpiece is sloped to encourage samples to roll towards a sample catcher attached to the very bottom of the chamber. This catcher is inaccessible during the experiment, but may be removed once the NESL is returned to the instrument floor. As all

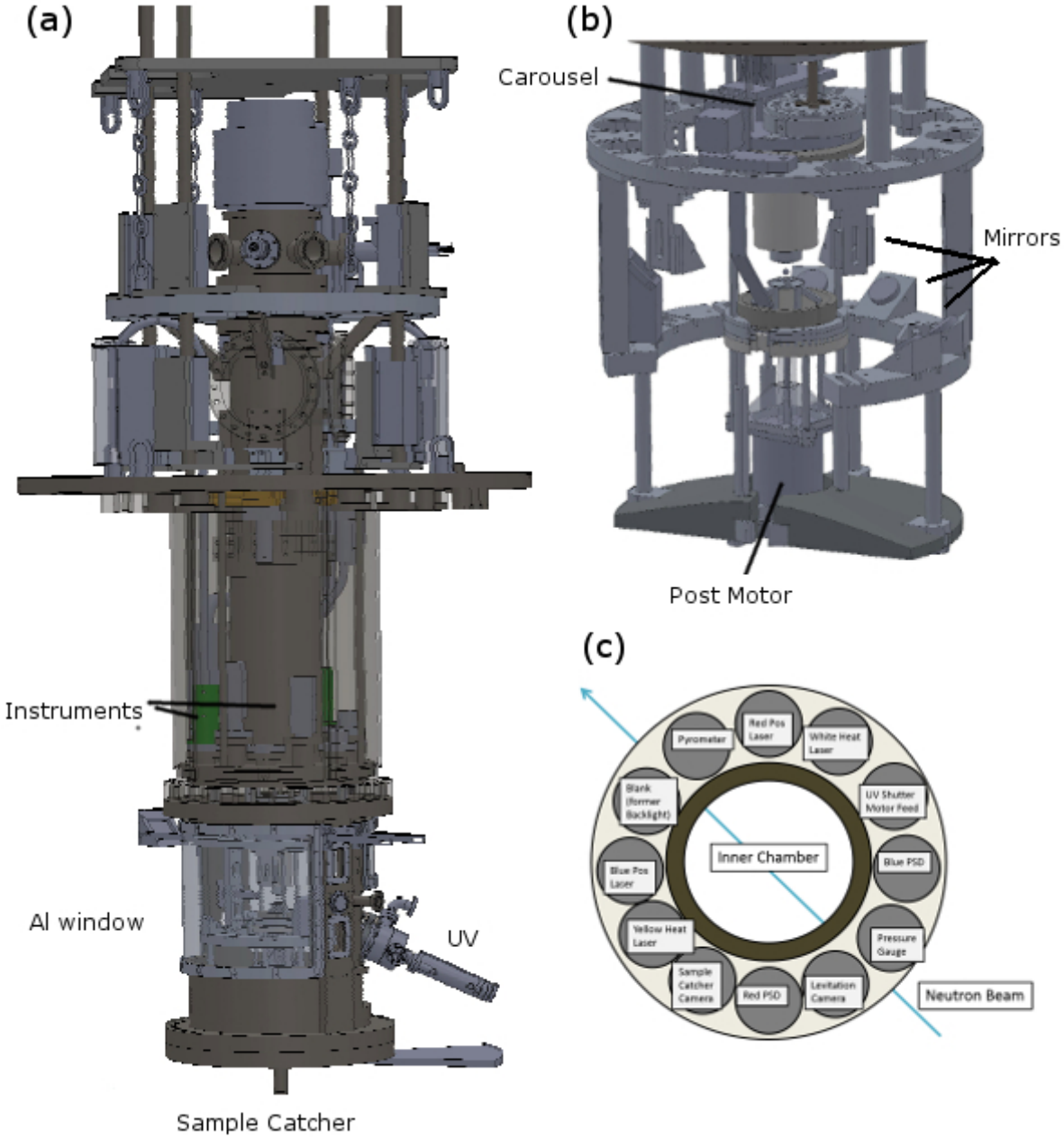

Figure 2.11: (a) Schematic of the NESL[3] (b) The electrode platform and mirror assembly (c) port layout from above.

samples not stuck in the electrode staging are in this catcher at the end of the experiment, it can be challenging to sort them, as the best identifier is their mass. It is important to keep consistent, well logged process knowledge; samples have to be carefully chosen to have distinguishable initial masses, and evaporative mass loss on one sample may cause it to be confused with another.

While all ESL systems exhibit varying degrees of robustness against sample evaporation, the NESL has the unique disadvantage of relying on mirrors for positioning, heating, and temperature measurement. While the positioning system functions well with coated mirrors, the pyrometer readings can actively change as material is deposited on the mirrors. As was learned during the processing of silicon, too much deposition on the heating laser mirrors can cause a decrease in their reflectivity, heating the mirror and eventually destroying them. With the long pumping times currently associated with the system, this must be avoided on the beamline.

Epoxy spheres analogous to those described in the BESL section were attempted for neutron scattering experiments using diamond powder, but were unable to charge sufficiently relative to their increased mass. Several solutions have been suggested, including hollowing out vanadium spheres and filling them with diamond powder, or coating the epoxy samples in a graphite layer for potentially easier surface charging.

2.5 X-Ray Analysis

2.5.1 Corrections

The polycrystalline nature of the samples, as well as their large, often multiaxial spin, mean the diffraction patterns obtained resemble well-averaged powder patterns. A proper quantitative analysis of powder diffraction data, whether on crystalline samples or liquid droplets, requires extensive data reduction and careful correction. High temperature solidification studies in a containerless environment add another layer of complications, such as the impossibility of including standards in each sample for phase fraction quantification, translational instability of the specimen, or even effects from the uncommon spherical sample geometry. The simple act

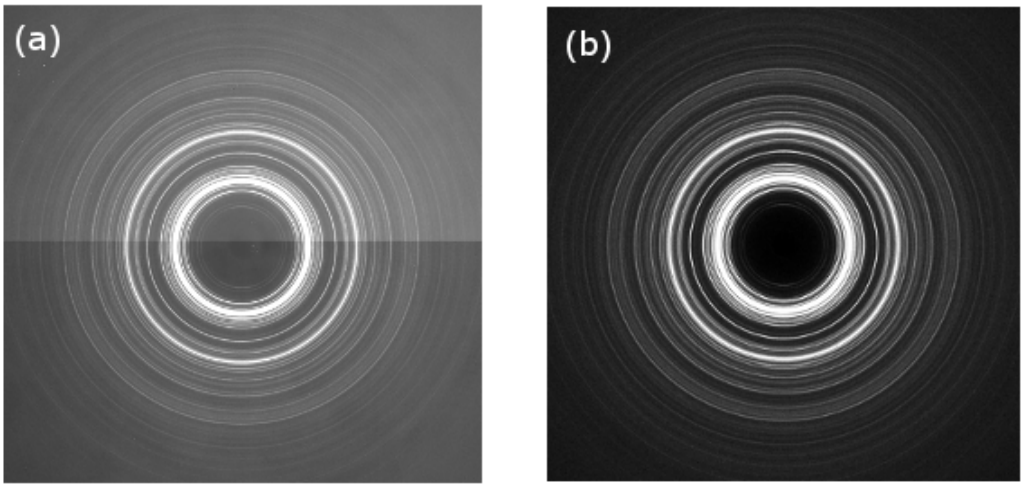

Figure 2.12: (a) Raw data taken on solid sample (b) Data corrected for background and bad pixels

of taking standards requires creative solutions. Many of the corrections are standard [115–117], while several have been developed recently specifically for the particular requirements of ESL scattering experiments [118, 89].

In order to obtain a polycrystalline silicon diffraction pattern for detector calibration, the ISU team mixed NIST SRM-640c Si powder with Epoxy Technology Ep-Tek 353ND 2-Part Epoxy in spherical molds. These spheres were capable of charging and levitation, and were used in both BESL 2013 and 2016 runs. They were floated as close as possible to processing position during acquisition. The GE detector itself was placed as close as possible to the beryllium exit dinwo of the BESL, ∼550 mm from the sample for all data taken during the BESL 2013 run. During the 2016 run, in addition to the 550 mm distance, the detector was also moved back to ∼1250 mm, sacrificing range in Q for better resolution of crystal peaks for the purpose of phase analysis.

All diffraction patterns were first corrected for background and dark current by subtracting dark frames, obtained with the x-ray shutter closed. As there was virtually no discernible difference between patterns taken with the shutter closed versus an open shutter on an empty chamber, the empty chamber frame was used for background subtraction on all crystalline

analysis via ImageJ scripts[119]. A gain map specific to the detector was applied to all frames to remove signals from bad pixels.

Further correction for detector artifacts then proceeded via Fit2D[**?**]. The sample-to-detector distance and beam center was refined using the built-in capabilities of Fit2D. As the detector proved difficult to align perfectly orthogonal to the incoming beam, a tilt correction was applied, derived in [120].

For the purposes of liquid scattering analysis, additional inelastic contributions must be subtracted from the the recorded intensity. The largest contribution comes from Compton scattering,

$$n(q) = (E_{\mathrm{c}}/E)^{\alpha} i(M) \tag{2.16}$$

where $(E_C/E)^{\alpha}$ is the Breit-Dirac recoil factor and $i(M)$ is the modified scattering intensity, given by

$$i(M) = \sum c_i Z_i - \sum c_i (\sum_z f_e^2)_i \tag{2.17}$$

where c_i is the fraction of element i and f_e is the electron form factor. Flourescence contributions, wherein an incident photon is absorbed and re-emitted at a longer wavelength, must also be subtracted. Here the flourescence contributions were determined and subtracted on an ad-hoc basis. A Laue diffuse scattering term, originating in samples of multiple atomic species, is given by

$$(\sum \chi_i f_i^2) - (\sum \chi_i f_i)^2 \tag{2.18}$$

and is subtracted when calculating $S(Q)$.

Specific to the BESL environment, Bendert et al.[118] derived an absorption correction for spherical samples in an offset incident beam geometry. The derivation is long and complex,

and the reader is referred to his derivation in Ref. [118] for details. This correction was applied to all liquid scattering data obtained using x-rays.

2.5.2 Rietveld Refinement

The Rietveld technique[117] is a powerful method for the extraction of quantitative structural information from powder samples. A model of the phases of interest are constructed, described by a wide range of parameters. The calculated scattering pattern from this model is then compared to experimental data. The minimization function, M_p, is then computed according to

$$M_p = \sum_i w_i (I_i - I_{ci})^2 \tag{2.19}$$

where w_i is the statistical weight at point i, I_i is the observed intensity at point i, and I_{ci} is the calculated intensity at point i. Any number of parameters, chosen by the user, are then modified. The resulting M_p is compared against the original, and the changes thrown out or applied accordingly. Several goodness of fit parameters are used to evaluate the accuracy of the model. The most commonly given parameter is the R-factor R_p, given by

$$R_p = \frac{\sum |I_o - I_c|}{\sum I_o} \tag{2.20}$$

where I_0 refers to the observed intensity, and I_c is the calculated intensity. It is notable that neither value is considered the intensity from an individual bragg peak, as peaks frequently overlap.

The weighted pattern R-factor, R_{wp}, is more directly related to the residual and therefore often considered a more accurate measure of fit. It is given by

$$R_{wp} = \sqrt{\frac{\sum w(I_o - I_c)^2}{\sum w I_o^2}} \tag{2.21}$$

The minimization function also yields

$$\chi^2 = \frac{M}{(N_{\text{obs}} - N_{\text{var}})} = \frac{\sum_i w_i (I_i - I_{ci})^2}{(N_{\text{obs}} - N_{\text{var}})} \tag{2.22}$$

which is another common indicator of fit, not unique to Rietveld. In general, a value of χ^2 close to unity is considered to indicate an accurate model, and R_{wp} less than $\sim .1$ is a reasonable profile factor. However, these parameters can be misleading when the dataset is overfitted or reliant on poor statistics, and so they should be thought of as guidelines. The most reliable way to judge a refinement is the residual function itself. During the course of this work, all refinements were accomplished using the General Structural Analysis System (GSAS) [115] using the EXPGUI user interface[121].

Care must be taken to avoid false minima in the residual function. Refinements of complex structures and multi-phase materials frequently get "stuck" at a non-local minimum. In the studies presented here, 100 refinement cycles were allowed on each scan to reach convergence.

There are a variety of parameters which may be used to improve the calculated model. The order in which these are applied and refined is crucial to both the stability of the refinement and the reliability of the results. In refinements presented here, lattice parameters were first refined, with a fixed scale factor and small half-width pseudo-voigt peak form factor ($W \sim 0.5$). The dimensionless phase scale factor S_{ph}, representing the molar cell fracion, was then allowed to freely refine. A simple background function was then applied using the built in Chebeschev polynomial of the first kind, a functionality in GSAS, given by

$$I_i = \sum_{j=1}^{N} P_j T'_{j-1} \tag{2.23}$$

where T' is given by

$$T'_n = \sum_{m=0}^{i-1} C_m X^m \tag{2.24}$$

and X is defined by

$$X = \frac{2(T - T_{\min})}{T_{\max} - T_{\min}} - 1 \tag{2.25}$$

The coefficients T'_{j-1} and the values of C_m are taken from Ref.[122]. Once a reasonable fit was obtained for the phase in question, the background was further refined. The peak profile shape was described by a pseduo-Voigt function, given by

$$F(\Delta T') = \eta L(\Delta T', \Gamma) + (1 - \eta) G(\Delta T', \Gamma) \tag{2.26}$$

where η is the mixing function and Γ is a function of the gaussian full width at half maximum, both detailed in the GSAS manual. The width of the peak is described by

$$\sigma^2 = U \tan^2\Theta + V \tan\Theta + W + \frac{P}{\cos^2\Theta} \tag{2.27}$$

while the Lorentzian coefficient is

$$\gamma = \frac{X + X_e \cos\phi}{\cos\Theta} + (Y + Y_e \cos\phi + \gamma_L d^2) \tan\Theta \tag{2.28}$$

P in the gaussian contribution and the first term of the lorentzian contribution are directly related to Scherrer broadening. Often, synchrotron beamline instruments have a set of parameters that are dependent upon the beam profile and are available in an instrument parameter file. As the samples in these studies covered a wide range of temperatures and phases, several of the profile coefficients were refined. In the course of these refinements, initially W was refined, and later γ_X and γ_Y were also refined.

The Debye-Waller (DW) factor, also known as the temperature factor, represents the q-dependent effect of the thermal motion of atoms on the scattering pattern.

$$T = \exp[-(8\pi^2 U_{\text{iso}} \sin^2\Theta/\lambda^2)] \tag{2.29}$$

Here U_{iso} is measure of the mean square displacement from equilibrium. It is sometimes represented as B_{iso}, given by

$$B_{\text{iso}} = 8\pi^2 U_{\text{iso}} \tag{2.30}$$

Only the isotropic form of the DW term was used in these refinements. The temperature factor is known to couple to the atomic fractional occupancies f_i, and frequently cannot be simultaneously refined. As the temperature during crystalline studies varied from 900 to 1500 K, significant changes in the DW term were expected and observed during sequential refinement, and so fractional occupancies were only refined as a sanity check at high and low temperatures.

Sequential refinements were performed using the SEQGSAS subroutine of the EXPGUI interface. For each thermal processing cycle, there were typically 100 to 180 crystalline frames. Sequences were started both at high and low temperatures in order to avoid biasing. Structural transitions tend to cause divergence in the sequential refinement, and so starting points were also picked in the middle of each transition region, when both phases were present.

Producing a successful Rietveld refinement is by nature an iterative process; completing a long sequence of such refinements while maintaining confidence in any resulting trends, even more so. Scans functioning as the base of a sequence were refined multiple times, from multiple sets of starting parameters, to ensure that values obtained on final convergence were accurate. The refinement state of all parameters, free or fixed, was kept consistent throughout regions of sequences with a constant set of phases present. In addition, sequences had a tendency to crash unexpectedly from extraneous terms diverging, and so the final set of refined parameters was defined by the smallest set that could well describe the entire sequence.

All frames included in refinement converged. Each frame in all sequences had a final R_{wp} less than 0.09, and was frequently closer to 0.05.

2.5.3 Diffuse Background

The Chebeschev polynomial based background presented in the previous section provided adequate modeling for individual frames at low temperatures. However, during the work in Chapters 3 and 4, the high temperature diffraction data contained a large diffuse signal originating from residual liquid throughout solidification and a notable amount of disordered material for several hundred degrees during the subsequent cooling. The Chebeschev polynomial function proved inadequate for subtracting this background, not matching the oscillations well, and frequently had too much intensity, causing a negative residual. In addition, studies of the lattice parameters as a function of temperature featured an artifact at the allotropic transition, wherein the profile function corresponding to the Fe_2B phase coupled with the poorly modeled background. While a graphically defined background could be a better match, it required upwards of 20 parameters to model accurately, and performed similarly poorly during sequencing.

One solution to this problem is to create a polynomial function that subtracts all of the background and leaves a flat residual. As the peaks were fairly broad, and sensitive coupling with the background had been demonstrated, it was decided this would not be an ideal approach, as it was desirable to check the background function for individual frames to ensure the integrity of the refinement process. Additionally, GSAS has built in functionality to model diffuse scattering; however, at the time the work was being performed, no refinements would stably converge with these terms activated.

It was found that the pre-solidification liquid diffraction pattern could be modeled by combining two of the crystalline phases with very broad profile functions, carefully tuned thermal parameters, and spherical harmonic based textural modeling. By allowing the scaling factors and "lattice parameters" (for thermal expansion/contraction effects) of the two-phase "liquid" function to freely refine during a sequence, the new background both matched the oscillations corresponding to the diffuse scattering and assigned the correct intensities necessary to flatten the residual function. All refinement artifacts subsequently disappeared when using this tech-

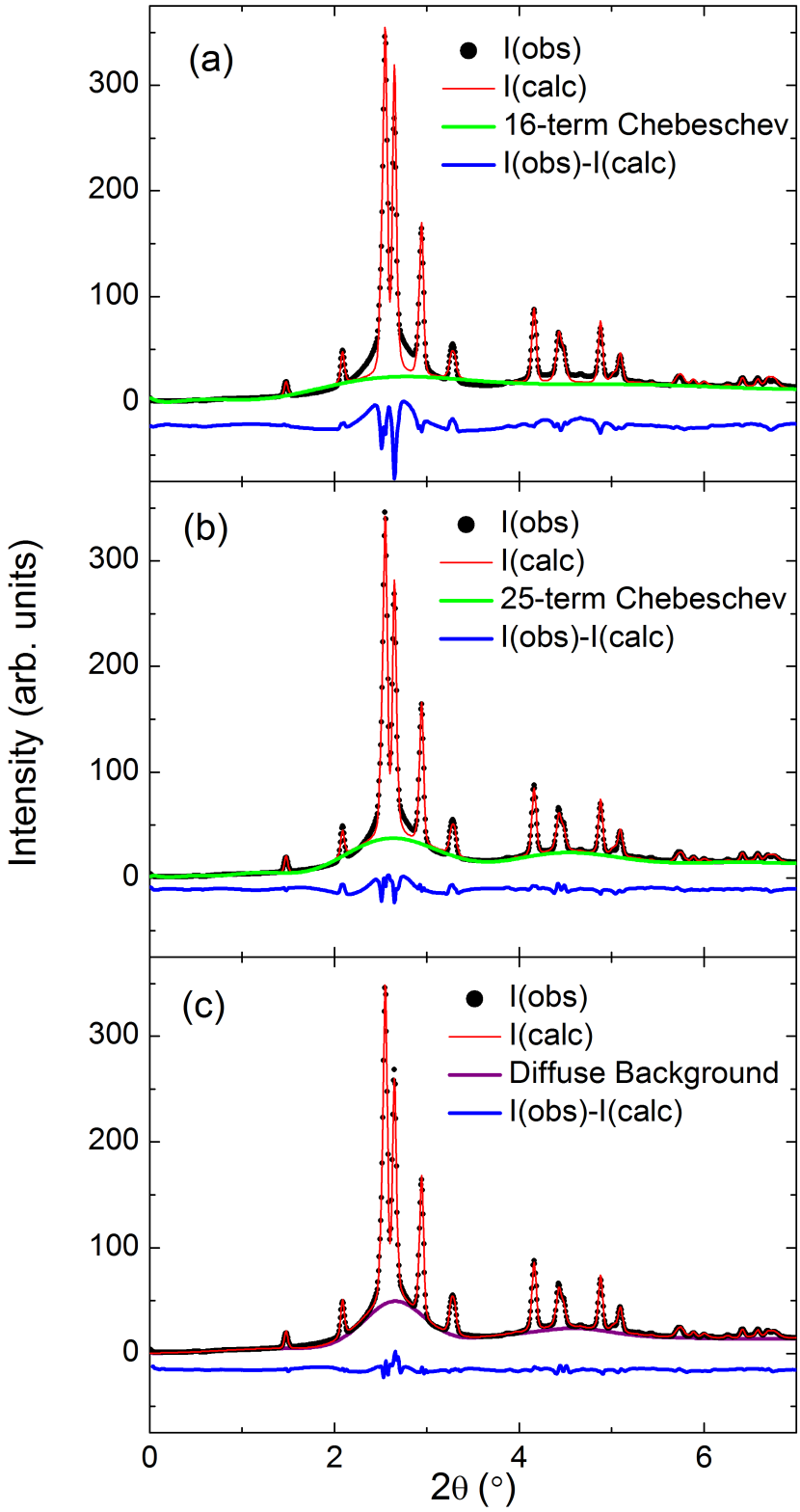

Figure 2.13: Rietveld refinement performed at high temperatures using (a) a 16 term Chebeschev polynomial background function (b) a 25 term Chebeschev polynomial (c) a custom function modeled on the liquid. (see text)

nique, and divergences during sequential refinement were notably reduced. An example of the technique is shown in Fig. 2.13.

There is a significant computaitonal cost associated with this approach, however, resulting from the extremely wide peak profile functions required. A typical refinement cycle using normal background functions requires a fraction of a second; with this background technique, each cycle took up to 18 seconds. This caused sequential refinements to require 8 to 10 hours per run. In this light, this should only be used when significantly overlapped peaks with broad profile functions are present.

Similar approaches have being applied to studies of amorphous materials in the pharmaceutical industry[123] and nanocrystalline composites[124] for the purpose of phase quantification. No quantitative data was derived here. However, it is an approach that may be applied to future ESL solidification studies. It would be advisable, however, to formalize the technique somewhat in a separate program, which could pre-proces the data outside of the Rietveld package of choice.

2.6 Liquid Scattering Analysis

Much of the formalism for the scattering of x-rays from liquids was developed in the 1960s. Until the development of containerless systems, however, the field remained somewhat niche, and compared to crystalline analysis, there is a scarcity of texts thoroughly describing the underlying mathematical basis. Even after reduction to the normalized structure factor $S(q)$, the ensuing analysis and interpretation is a continually developing subject. Some of the techniques described here for data renormalization and interpretation were only applied to levitation systems very recently, within the past 10 years. This section will begin by laying out some of the mathematical foundations of the study of liquids, which will rely heavily on the excellent and thorough derivations in Refs. [125, 126]. It will then discuss the computational modeling for interpretation of experimental results, and some of the common indexing methods.

2.6.1 Mathematical Foundation

The amplitude of scattered x-rays is described by

$$A(\mathbf{Q}) = \sum_k f_k(\mathbf{Q})\exp(-i\mathbf{Q}\cdot\mathbf{r}_k) \tag{2.31}$$

where $\mathbf{Q}$ represents the momentum change given by $\mathbf{Q}_{\text{final}}$-$\mathbf{Q}_{\text{initial}}$, and $f_k(\mathbf{Q})$ is the atomic scattering factor for atom k at real-space position $\mathbf{r}_k$. The coherent scattering intensity is then calculated through

$$I^{\text{coh}}(\mathbf{Q}) = <|A(\mathbf{Q})|^2> = <\sum_j\sum_k f_j(\mathbf{Q})f_k(\mathbf{Q})\exp(-\mathbf{Q}(\mathbf{r}_j-\mathbf{r}_k))> \tag{2.32}$$

where in a disordered system, such as a liquid, $(\mathbf{r}_j - \mathbf{r}_k)$ is not described by a rigid structure, but by an average distribution across all directions, such as represented by the pair distribution function. The spherical symmetry allows $\mathbf{Q}$ to be represented by the magnitude Q.

For a one component system, $f_j = f_k$, and so

$$I^{\text{coh}}(\mathbf{Q} = f_k(\mathbf{Q})^2 < \sum_k \exp(-\mathbf{Q}(\mathbf{r}_j-\mathbf{r}_k))> \tag{2.33}$$

The normalized structure factor $S(Q)$ is defined by

$$S(Q) = \frac{I^{\text{coh}}(Q) - |f(q)|^2}{f^2(Q)} + 1 \tag{2.34}$$

The equivalent expression for neutron scattering is given by

$$S(Q) = \frac{I^{\text{coh}}(Q) + <b>^2 - <b^2>}{<b>^2} \tag{2.35}$$

For a two component system, Eq. 2.32 may be expanded to

$$I^{\mathrm{coh}}(\mathbf{Q} = f_1^2(Q) < |\sum_{j=1}^{N_1} \exp(-i\mathbf{Q}\cdot\mathbf{r}_{1j})|^2 > + f_2^2(Q) < |\sum_{k=1}^{N_2} \exp(-i\mathbf{Q}\cdot\mathbf{r}_{2k})|^2 + 2f_1(Q)f_2(Q) < \sum_{j=1}^{N_1}\sum_{k=1}^{N_2} \exp(-i\mathbf{Q}(\mathbf{r}_{1j}-\mathbf{r}_{2k})) > \tag{2.36}$$

where N_1 and N_2 are the number of atoms of species 1 and 2, respectively, and $f_1(Q)$ and $f_2(Q)$ are their atomic form factors. $S(Q)$ may then be determined as

$$S(Q) = \frac{I^{coh}(Q) - \sum_{i=1}^{n} c_i |f(q)|^2}{|\sum_{i=1}^{n} c_i f_i^2(Q)|^2} + 1 \tag{2.37}$$

where c_i and $f_i(Q)$ are the atomic fraction and q-dependent form factor. It can be shown[125] that $S(Q)$ is obtained by a fourier transformation of the pair distribution function $g(r)$ through

$$S(Q) = 1 + \rho_0 \int [g(r) - 1]\exp(-i\mathbf{Q}\cdot\mathbf{r})d\mathbf{r} \tag{2.38}$$

Finally, the reduced pair distribution function $G(r)$ may be obtained from

$$G(r) = 4\pi\rho_0(g(r) - 1) \tag{2.39}$$

which is used for normalization processes during the analysis procedure.

To obtain $I^{\mathrm{coh}}(Q)$, inelastic contributions must be subtracted out. The compton scattering correction is given by

$$n(q) = (E_c/E)^{\alpha} i(M) \tag{2.40}$$

where the first term is the Breit-Dirac recoil factor and α is a detector-dependent term, and $i(M)$ is given by

$$i(M) = \sum \chi_i Z_i - \sum \chi_i (\sum_Z f_e^2)_i \tag{2.41}$$

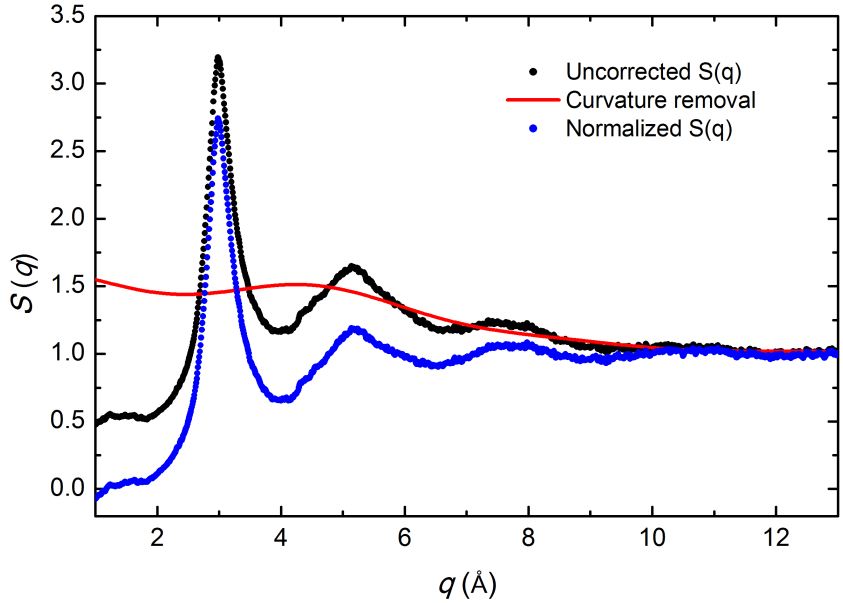

Figure 2.14: A representative neutron scattering $S(q)$ from the NESL at NOMAD. The black curve is the initial output from the NOMAD data reduction subroutines. The red curve is the curvature attributed to inelastic and secondary scattering, determined via the Peterson metric. The blue curve is the normalized $S(q)$.

In addition, flouruescence and Laue diffuse scattering corrections are subtracted, and are calculated in an ad-hoc manner.

2.6.2 Normalization

Proper normalization of any structure factor $S(q)$ generated from liquid scattering experiments is critical for both fourier transformation into the more intuitive pair distribution function as well as for comparison between different experimental methods, such as x-ray and neutron experiments. As it is not possible to add a standard to each sample for comparison, there is not an easy way to ensure differences in the recorded structure factor between different techniques, samples, or temperatures, is physically rooted, and not an artifact of the reduction process. Frequently, damping functions are convoluted with $S(q)$ to ensure it approaches unity at high q, potentially masking real correlations in the liquid. Advances in analysis specific to such levitated liquids for normalization and curvature correction were made during the last several years to correct these issues, and applied to all results presented here.

The reduced pair distribution function, $G(r)$, ideally features a line below the hard sphere cutoff, with a slope given by $dG/dr = 4\pi\rho_0$, where ρ_0 is the number density. Non-linearity in this region represents unphysical short-range correlations that can produce large, spurious curvature in $S(q)$. In additions, a deviation from the experimental slope will result in improper normalization across $S(q)$, a problem frequently seen in older liquid scattering data, giving spurious coordination number calculations. Minimization of the Peterson metric[127], given by

$$\Delta G_{\text{low}} = \frac{\int_0^{r_{\text{low}}} [rG(r) - (r^2/r_{\text{low}}^3) \int_0^{r_{\text{low}}} rG(r)dr]^2 dr}{\int_0^{r_{\text{low}}} [(r^2/r_{\text{low}}^3) \int_0^{r_{\text{low}}} rG(r)dr]^2 dr} \tag{2.42}$$

can correct these effects, and together with proper correction for various physical effects, also improves the limiting behavior at high Q.

Neutron diffraction $S(q)$s produced by the data reduction routines at NOMAD (BL-1B, Spallation Neutron Source) tended to have extremely large curvatures as mentioned above. To fix these, as well as improve the normalization of the x-ray data, Johnson [128, 92] developed a LabVIEW program specifically to perform the minimization with significantly more user control. He noted that RMC simulations performed on the data undergoing absolute normalization resulted in both significantly better fits and more realistic indexing results. An $S(q)$ acquired at NOMAD and corrected using this technique is demonstrated in Fig. 2.14.

2.6.3 Coordination Number

The coordination number (CN) in a liquid is a primary measure of short range order. The radial distribution function, given by $R(r) = 4\pi r^2 g(r)$, is generally integrated to find the population of a coordination shell, as in

$$\text{CN} = \int_{r_0}^{r_1} 4\pi r^2 g(r) dr \tag{2.43}$$

where r_0 is the minimum below the first peak of $g(r)$, and r_1 is either the first minimum after the first peak of $g(r)$ or the first minimum after the first peak of $R(r)$. The subject of the

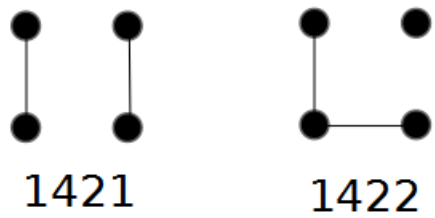

Figure 2.15: Example of n_4 distinguishing between two different HA topologies.

integration limits is hotly debated, and as the integration is exquisitely sensitive to the bounds, can result in large variances in reported coordination numbers.

2.6.4 Honeycutt-Andersen Indexing

The method of Honeycutt and Andersen (HA) was first designed to describe the short range ordering in Lennard-Jones cluster enesmbles generated by Molecular Dynamics and Monte Carlo simulations. A bond length is defined, typically determined by the first minimum after the first peak. The clusters are assigned a set of four indices (n_1, n_2, n_3, n_4). n_1 is either a 1 for bonded root pairs, or a 0 for unbonded pairs. n_2 denotes the number of shared nearest neighbors between the two atoms in the root pair. n_3 is the number of bonds among the shared nearest neighbors from n_2. The configurations described by n_3 are often not topologically unique, as described in Fig. 2.15. n_4 is therefore a degeneracy breaking index, signifying only different arrangements of the bonds counted by n_3.

The different combinations of indices correspond to different structural motifs. The most commonly reported indices are described in Table.2.1.

Initial HA analysis was performed by a Mathematica package written for the purposes of this dissertation. It proved to be fast but inconsistent when differentiating between topologies for n_4. A python package written by the Washington University group [3] was obtained instead and modified for the analysis in Chapter 5.

Table 2.1: Voronoi and HA indices corresponding to common structural motifs.

Symmetry	Voronoi	HA Index
Perfect Icosahedral	(0,0,12,0)	1551
Distorted Icosahedral	(0,0,10,2),(0,2,8,1)	1541,1431,1311,1321
Trigonal Prism	(0,3,6,0)	
BCC	(0,6,0,8)	1661,1441
FCC	(0,12,0,0)	1421,1422

2.6.5 Voronoi Tesselation

Voronoi indexing is another measure of the local order in a system, which proceeds similarly to the construction of a Wigner-Seitz cell. A vector is constructed between each nearest neighbor in the ensemble. That vector is then bisected with a plane normal to the vector. The polyhedron constructed by the intersection of these planes is then indexed by sorting and counting the faces by the number of bounding edges, such that 0,2,10,2 would correspond to 0 faces with 3 edges, 2 faces with 4 edges, 10 faces with 5 edges, and 2 faces with 6 edges. In general, the relative abundances of the different voronoi indices are used to characterize the average local ordering in a system. A higher number of edges corresponds to a more close packed system[98].

Common voronoi indices and the structural motifs they describe are listed in Table 2.1. Voronoi indexing is also used as a measure of the average coordination number, by counting the total faces of each polyhedron, and can be species specific. The number tends to be inflated by extremely small faces from distant atoms, and so most voronoi packages include limitations on the minimum countable face area, and the minimum countable edge length.

All voronoi tesselation here was performed with the Voro++ package [129] as implemented by Ovito[130]. A custom python script was written to apply minimum face sizes and edges, and to sort and count the output. For the calculations reported here, a minimum face size of 0.3 $Å^2$ was used.

2.6.6 Reverse Monte Carlo simulations

Simulating the structure of disordered materials is traditionally the realm of Molecular Dynamics (MD) simulations or other empirical potential based computational methods. By

contrast, Reverse Monte Carlo (RMC) techniques enable the simulation of a structure without the need for complicated potentials or large computation time. Unlike traditional Monte Carlo methods, where a probability distribution or potential is used to generate the configuration of interest, RMC is focused on a fit to experimentally obtained structure factors, using properly scaled data as a constraint. Other experimentally derived quantities, such as number density, can be used to constrain the data further.

RMC works by minimizing some quality factor (typically a χ^2 value) between an experimental structure factor and a simulated pattern from the atomic arrangement. In a similar manner to a least squares refinement scheme, a number of atoms (the exact quantity defined by the operator) are moved according to the metropolis algorithm [131]. In the case where there is no potential used, a new $S(q)$ or $g(r)$ is generated and the effect on the χ^2 value checked. In the case of a decrease, the move is accepted. In the case of an increase, the move may be accepted according to a weighted Boltzmann proability ($\exp[-(\chi_f^2 - \chi_i^2)]$), in order to help escape local minima in the χ^2 landscape. Other parameters to ease the simulation may be used, such as enabling a certain percentage of moves as swaps between different atomic species. Atoms are treated as hard spheres, and minimum hard cutoff distances are defined for each partial pair correlation function (PPCF). Here, all cutoffs were determined from a combination of experimental results and atomic sizes. The simulation may also take defined bin sizes, and here a bin size was chosen to match the resolution of the scattering data at 0.01 Å. All simulations were run until the χ^2 value had stabilized at a minimum value. The bin size was then widened and the maximum move size increased to enable the configuration to escape any local minima in χ^2 ,before continuing the simulation at the original parameters.

An initial configuration is needed to begin the simulation. The ideal choice uses the results of an MD simulation to begin with a physically based atomic topology. In this case, the RMC algorithm will act in the same way as a Rietveld refinement, and change the configuration to better suit the experimentally defined pattern. When no MD results are available, as was the case in Chapter 5 of this work, it is important to use a variety of starting configurations to avoid biasing the final results.

In the case of a single species system, a single pattern is all that is needed to generate a configuration. As the simulation will tend towards the most disordered configuration that fits the experimental data, however, conventional wisdom is that the RMC algorithm will fit anything, but may not be physical. Constraints are required to ensure any results are meaningful. In the case of two or more component systems, the situation becomes more difficult. In a system of N components, there are $N(N-1)/2$ different PPCFs describing the distribution of each pair type. For instance, in a two components system ($N = 2$), there are 1-1 pairs, 1-2 pairs, and 2-2 pairs. As such, to have confidence in the refined structure, three different constraints are needed. When, as was this case in the work in Chapter 5, one of the PPFCs contributes very little to the scattering pattern, it is possible to constrain this contribution to zero. This is common with light elements in x-ray diffraction experiments, or species composing a small relative fraction of the sample.

A common criticism of the RMC method addresses the lack of "uniqueness" of a simulation result, and by extension, whether or not the generated model is correct. It has been thoroughly documented that the configurations produced by RMC will tend towards the most disordered state possible [131]. When modeling a liquid structure which lacks static symmetry with, say, 5000 atoms , there are an arbitrarily large number of ways to generate the same structure factor. However, consistency with the experimental data is all that can be hoped for, and should be the only criteria of "correctness". There is, by definition, not a "unique" configuration for a physical liquid. One can constrain the simulations with a number of parameters, such as bond angle constraints, number density, coordination number, and any possible topological constraints. By using a sufficiently large number of atoms, and repeating the simulation from a number of starting configurations to avoid trapping in local minima of the residual function, it is reasonable to believe that the sampled average is at least representative of the likely local configurations of the liquid. Any claims beyond this, especially for configurations generated without the use of a potential (as in this thesis), should be treated with a healthy dose of skepticism.

CHAPTER 3. THE SOLIDIFICATION PRODUCTS OF LEVITATED $FE_{83}B_{17}$ STUIDIED BY HIGH-ENERGY X-RAY DIFFRACTION

This chapter has been published in *Journal of Applied Physics* in collaboration with G.E. Rustan, A. Kreyssig, S. Lapidus, M.J. Kramer, and A. I. Goldman[132], and has been adapted to be consistent with the formatting in this dissertation. The author's contribution to this work involved assisting in sample preparation and data acquisition, performing all analysis, and preparation of the manuscript in conjunction with A.I. Goldman. G.E. Rustan prepared samples and acquired data. A. Kreyssig assisted in experiments during BESL 2013 and helped edit the manuscript. S. Lapidus performed the room temperature powder measurements presented in Fig. 3.9. M.J. Kramer assisted in editing the manuscript and provided invaluable insight during the analysis process.

3.1 INTRODUCTION

The Fe-B binary alloy is an important system for investigations of glass-forming alloys, as well as their mechanical and magnetic properties. In addition to being a good binary glass forming system [133], Fe-B also forms the basis of a large body of multi-component glass forming systems, ranging from ternary alloys such as Fe-B-Si [134] to five- and six-component bulk glass forming alloys such as $Fe_{43}Cr_{16}Mo_{16}(C, B, P)_{25}$ [135] with critical cooling rates on the order of 100 K/sec. These materials exhibit excellent glass forming ability and important engineering properties such as hardness [136], corrosion resistance [135], and soft ferromagnetism [137, 138]. The Fe-B binary system continues to receive significant attention, in both the glassy [139, 140] and liquid states [141, 45, 142–145, 44, 146], as it is a valuable system for performing fundamental studies to gain insight into the nature of the glass transition.

According to the equilibrium stable phase diagram [147], Fe-B alloys with Fe contents $\geq$ 66.7 at.% tend to form two-phase mixtures of Fe_2B and Fe. However, when the Fe-B alloys are initially formed into a glassy state and undergo crystallization during subsequent annealing processes, it has been found that a wide variety of metastable intermetallic compounds can form [148, 148]. Potentially, these metastable phases may play an important role in the production of industrially relevant materials such as permanent magnets [29, 32]. The three most commonly observed metastable phases are body-centered tetragonal (*bct*) Fe_3B, orthorhombic (*o*) Fe_3B, and face-centered cubic (*fcc*) $Fe_{23}B_6$. Nevertheless, recent assessments of the Fe-B binary system, including both experiments [148] and calculations [148], have verified that the only stable intermetallic phase with Fe content greater than 50 at.% is Fe_2B, and *ab-initio* calculations of the cohesive energies of several Fe-B intermetallic phases have verified that *bct*-Fe_3B, *o*-Fe_3B, and *fcc*-$Fe_{23}B_6$ are indeed metastable phases [28].

The solidification behavior of the Fe-B binary close to the eutectic composition, $Fe_{83}B_{17}$, particularly with respect to metastable phase formation, has remained an open and interesting question. The $Fe_{23}B_6$ structure has been studied in some detail due to its importance in the formation of critical hard magnetic phases in the Nd-Fe-B system. Previous work has established links between thermal history and the resulting microstructure [46] and phase selection [141, 45], although little insight into the persistence of observed metastable phases has been gained. More specifically, the mechanisms by which $Fe_{23}B_6$, a structure important as a soft magnetic material and a critical intermediary in certain Nd-Fe-B magnets, [32] forms and is stabilized, remains unclear.

Recently, we reported on a set of *in-situ* high-energy x-ray investigations of the phase selection process for the eutectic $Fe_{83}B_{17}$ composition which revealed that the metastable $Fe_{23}B_6$ and fcc Fe phases grew coherently from the eutectic liquid and effectively suppressed the allotropic transformation to *bcc* Fe at lower temperature (Appendix A). Here, we present further evidence for this coherent growth, provide details of the different solidification pathways, describe the behavior of the lattice parameters of each phase over the studied temperature range, and present initial results from ambient temperature studies comparing samples containing the equilibrium or metastable phases.

3.2 Experimental Details

3.2.1 Sample Preparation

Samples of $Fe_{83}B_{17}$ were prepared by arc melting appropriate quantities of high-purity starting materials on a water-cooled copper hearth at the Ames Laboratory Materials Preparation Center. The starting materials were 99.99% pure Fe from Toho Zinc Corporation and 99.9999% pure B from Alfa Aesar; the purities are metals basis only. After the initial arc melting and formation of the alloy button, it was remelted three times to ensure that the composition was homogeneous throughout its volume. The alloy button was drop cast into rods with diameters of approximately 3 mm and these rods were cut into pieces with masses ranging from 25 - 75 mg. To form spheres for electrostatic levitation these fragments were laser melted on a substrate of either copper or graphite within the Iowa State Electrostatic Levitation Furnace (ISU-ESL) [93]. A Process Sensors Metis MI16 pyrometer was used to measure the sample temperature, and the sample surface condition was monitored by using a high-resolution color imaging system.

3.2.2 X-ray Measurements

High-energy x-ray diffraction measurements were performed at beamline 6-ID-D of the Advanced Photon Source (APS)- Argonne National Laboratory ($E = 132$ keV; $\lambda = 0.09403$ Å) employing an incident beam cross-section of 0.2 x 0.2 mm. The samples were electrostatically levitated in the Washington University Beamline Electrostatic Levitator, a full description of which can be found in Ref. [99]. Two orthogonal LED sources combined with position sensitive detectors and a feedback loop enabled full positional control. The temperature was measured with a Process Sensors Metis MQ2 pyrometer, using two wavelengths to help account for the unknown emissivity. The measured temperatures were later calibrated by matching the measured melt temperature to established values, under the assumption that the emissivity remained approximately constant over the measured temperature range.

X-ray diffraction patterns were collected using a two-dimensional (2D) Ge Revolution 41-RT flat panel detector. The range of scattering angles accessible in transmission geometry using

the 2D detector was $0.9° \leq 2\theta \leq 19.5°$, allowing measurements over a range of momentum transfers of 1 $Å^{-1} \leq Q \leq 22.6$ $Å^{-1}$. Spheres of Si powder mixed with epoxy were levitated as standards to determine detector tilt/rotation and flat-field corrections as well as refining the sample to detector distance to a value of 565 mm, using Fit2D [120, 116]. The high energy of the x-rays (132 keV) allowed a large penetration through the sample, and the resulting scattering came from throughout the bulk of the approximately 2 mm diameter samples. The linear attenuation coefficient was calculated based on sample geometry, giving a transmission of approximately 88% of the x-ray intensity. Frame rates from 1 fps to 8 fps were used for different heating/cooling cycles to ensure the acquisition of both rapid crystallization data as well as high-quality liquid and crystal data. The acquisition rate of the data presented here is generally 2 fps. Data storage restrictions of the detector system allowed a maximum of 188 frames, providing a maximum data collection time of 94 seconds at this frame rate.

In order to reduce outgassing and the ensuing charge loss during levitation, samples were heated to a partially molten state several times on the molybdenum launch post using the diode heating laser (λ = 980 nm). The samples were then floated and slowly brought up to the melting temperature of 1447 K. Once molten, samples were overheated by 150 - 200 K and held for 20 to 30 seconds to ensure the samples were fully molten and to facilitate the dissolution of any oxide or impurity phases that may have been present. The laser was then shut off and the samples radiatively cooled to a temperature below the measurement range of the pyrometer (approximately 900 K). Data were obtained for multiple heating/cooling cycles in order to ensure consistency in the structural refinements. Whereas only a few cycles were taken at low temperatures below the allotropic transition, several cycles were taken at higher frame rates in order to identify the initial phases that precipitated from the melt.

High resolution synchrotron powder diffraction data were collected at ambient temperature using beamline 11-BM at the APS (E = 30 keV; λ = 0.414 Å). The sample was placed in a Kapton capillary and held in place with the use of glass wool (which will contribute only a glassy signal). A bank of 12 point detectors were used and the data from each was corrected for detector offsets and sensitivities and merged into a final data file.

3.2.3 X-ray Data Analysis

Raw high-energy x-ray data were first corrected for bad detector pixels using the supplied pixel intensity map, the dark current was subtracted using ImageJ [149], and each frame was azimuthally integrated to produce x-ray powder diffraction profiles. The levitated samples spin about a vertical axis as a result of the radiation pressure from the laser heating, providing some degree of averaging over grains in the recrystallized material. Nevertheless, the raw x-ray data from solidified samples did exhibit some degree of texturing resulting in peak intensity fluctuations from frame to frame. For our structural refinements, a moving boxcar average over seven frames was applied to damp these intensity fluctuations. The refinements of the resulting powder diffraction patterns were accomplished using GSAS [115]. In general, the diffraction patterns in each temperature series were refined sequentially using the results at one temperature point as input for the next temperature point. In addition, the refinement sequences were initiated at both at the highest and lowest temperatures to ensure consistency in the structural parameters across the full temperatrure range. Pseudo-Voigt functions were used to model the peak shapes of the crystalline phases. Isotropic thermal factors were allowed to vary for the Fe atoms, but constrained within each phase to one value shared at all positions. Tenth order spherical harmonics were used to calculate texture corrections after boxcar averaging and, for most patterns, the texture index generated by GSAS was between 1.0 and 1.05, indicating only mild texturing. Our initial attempts to refiine the atomic occupancies found that the x-ray data were insensitive to small changes in occupancy, so site occupancies were fixed at unity to prevent correlations with the thermal parameter refinements.

A significant signal in frames from samples still partially liquid or containing disordered material made conventional background modeling difficult. Therefore, a background function was developed based on a fit to the observed scattering from the liquid phase. The use of this background resulted in a significantly better quality of fit and improved consistency when refining a large sequence of frames.

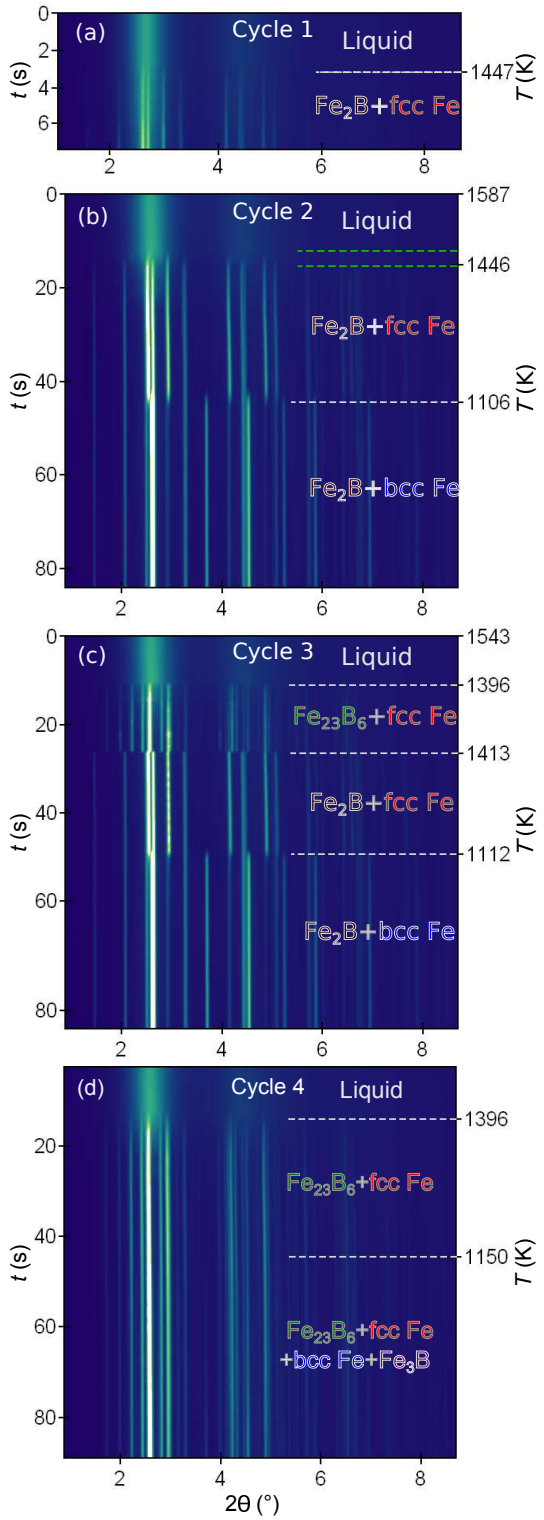

Figure 3.1: (Color online) X-ray diffraction measurements taken during free-cooling from the melt for (a) solidification directly into the equilibrium Fe_2B + Fe phases; (b) precipitation of metastable $Fe_{23}B_6$ + liquid phases in the region defined by the dashed green lines, followed by solidification into the equilibrium Fe_2B + Fe phase; (c) Solidification into the metastable $Fe_{23}B_6$ + Fe phases followed by a transformation into Fe_2B + Fe; and (d) primary solidification into $Fe_{23}B_6$ + Fe, which persists down to the lowest temperature measured (900 K). The precipitation of Fe_3B is concomitant with the appearance of *bcc* Fe.

3.3 Results

3.3.1 Overview

Cooling and heating cycles were run on several samples of $Fe_{83}B_{17}$ and key results are shown in Fig. A.1. The data shown were taken on the same sample processed through a number of heating/free-cooling cycles. These cycles are representative of all solidification pathways seen during the experiment, and were observed to occur in a seemingly random order at identical cooling rates, with no clear dependence on the thermal history of the sample.

Cycle 1, shown in [Fig. A.1(a)], describes the sample solidifying directly into the equilibrium Fe_2B + Fe phase, within the time resolution afforded by acquiring at 8 frames per second. Cycles 2 and 3 [Figs. A.1(b),1(c), 3 and 4] describe solidifications into an initial metastable $Fe_{23}B_6$ + Fe phase, which then subsequently underwent a second recalescence into the equilibrium Fe_2B + Fe phases within the solidification plateau. Cycle 4 [Fig. A.1(d)] describes solidifications where the metastable $Fe_{23}B_6$ + Fe phases persisted down to the lowest temperatures measured (∼900 K). When the metastable $Fe_{23}B_6$ + Fe phases persist down to low temperature, an additional metastable Fe_3B phase appears concomitant with the onset of the allotropic *fcc* to *bcc* transition for Fe.

One of the most interesting observations from Fig. A.1 is the behavior of the allotropic transition in the Fe phase fraction of the sample. In the presence of the equilibrium Fe_2B phase, the high-temperature *fcc* to *bcc* transition is clearly observed and sharp, as evident in Figs. A.1(b) and (c). However, no distinct transition is found in the presence of the metastable $Fe_{23}B_6$ phase in Fig. A.1(d). Instead, the *fcc* to *bcc* transformation appears to take place over a rather extended range of temperature. To investigate the evolution of the crystallization products of $Fe_{83}B_{17}$ with temperature in more detail, we performed Rietveld refinements on the full sequence of diffraction data shown in Figs. A.1(b), (c) and (d).

3.3.2 Cycles 2 and 3: Liquid → $Fe_{23}B_6$ → Fe_2B

Figure A.2 illustrates the refinements of the x-ray data at three selected temperatures for Cycle 2 [Fig. A.1(b)] obtained on free-cooling the liquid. The R-factors (R_p) for each refinement

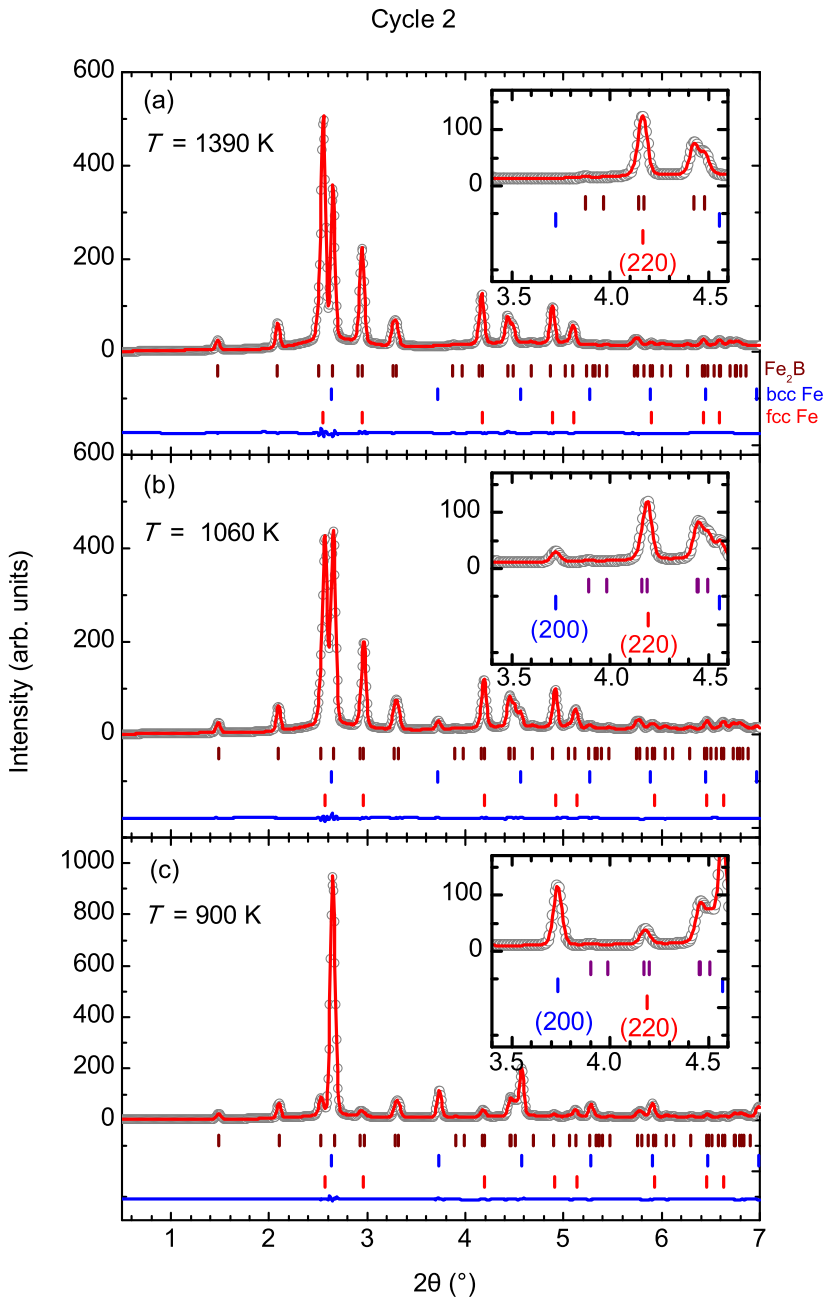

Figure 3.2: (color online) Refinements of the x-ray data taken on cooling into the equilibrium Fe_2B + Fe phases [Fig. A.1(b)] for Cycle 2 (a) immediately after solidification is complete, (b) during the Fe allotropic transformation, and (c) at the lowest recorded temperature. The insets show an expanded view near the positions of the (2 0 0) *bcc* and (2 2 0) *fcc* Fe diffraction peaks. The residual intensity at the position of the (2 2 0) *fcc* Fe diffraction peak in panel (c) is due to diffraction peaks from Fe_2B. The brown, blue, and red hash marks denote the calculated positions of diffraction peaks from Fe_2B, *bcc* Fe and *fcc* Fe, respectively. The line below the hashmarks plots the residuals from the fits to the experimental data.

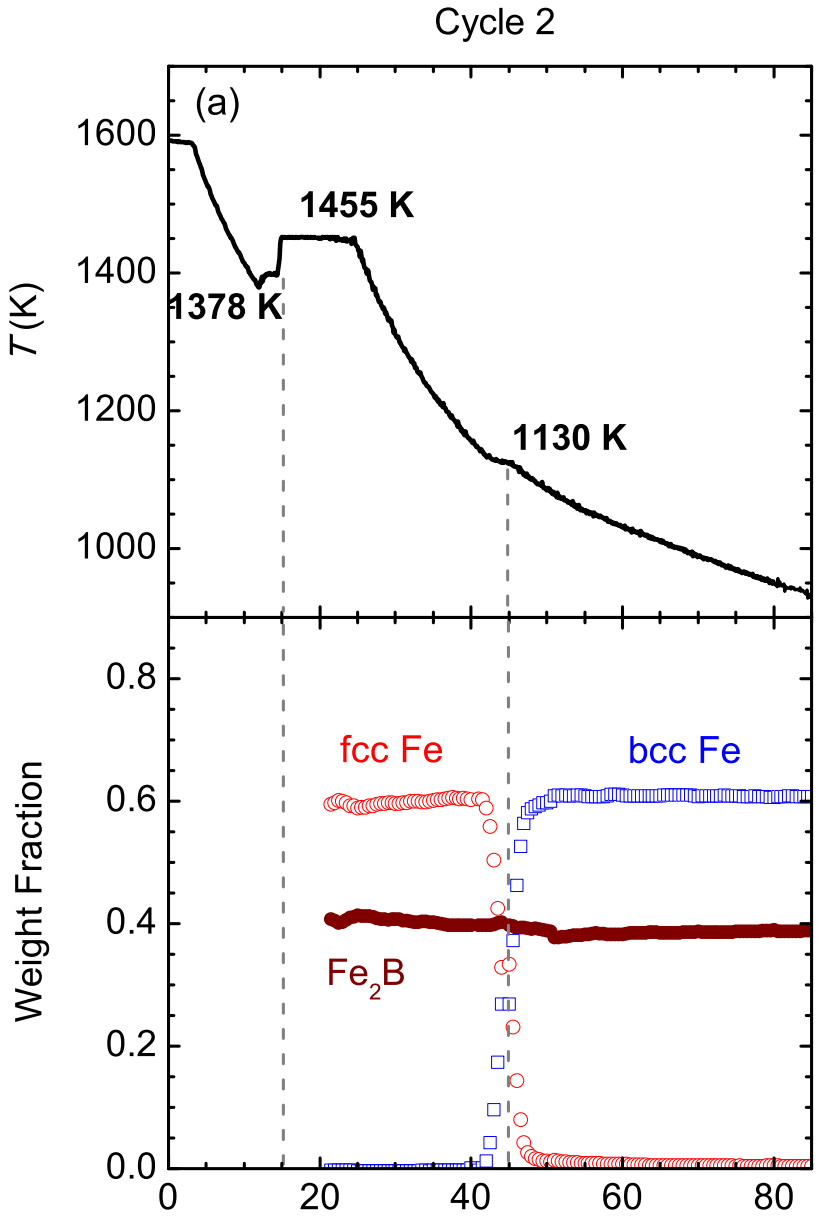

Figure 3.3: (color online) (a) Sample temperature curve determined from the pyrometer data taken during the high-energy x-ray diffraction measurement of Cycle 2. The initial temperature signature corresponds to the precipitation of the metastable phase. The second, larger recalescence indicates formation of the equilibrium Fe_2B + *fcc* Fe phases. The event at approximately 42 seconds corresponds to the allotropic *fcc* to *bcc* transition in Fe on cooling. (b) The weight fractions of the Fe_2B phase and Fe allotropes as determined from the sequential Rietveld refinements of the diffraction data.

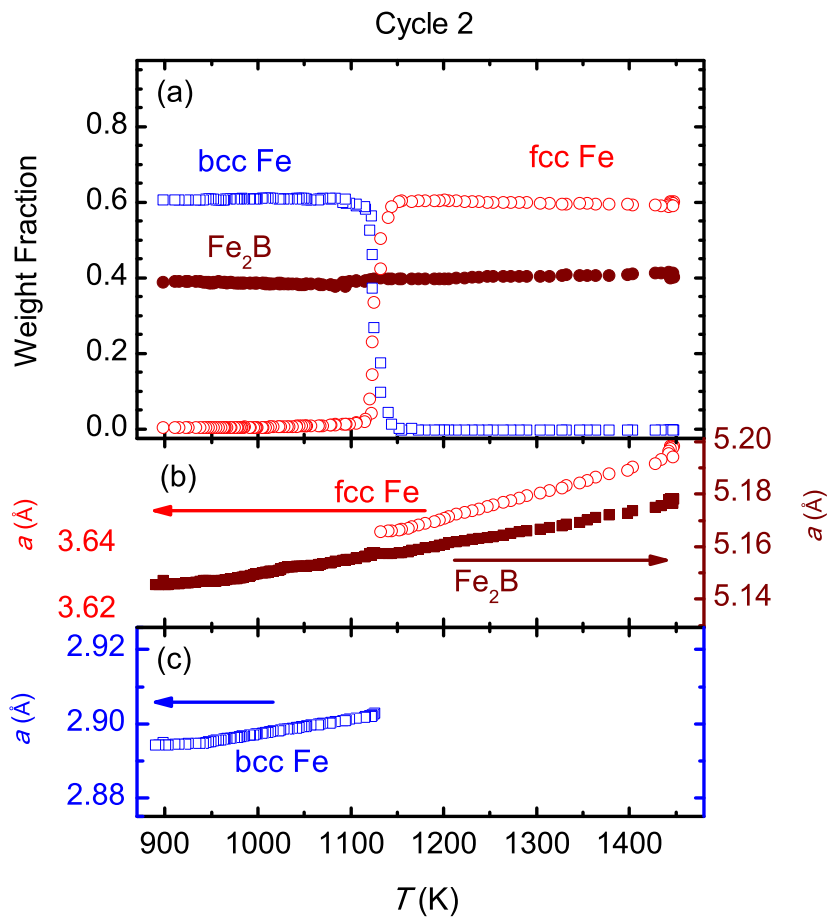

Figure 3.4: (color online) Results of the Rietveld refinement of the diffraction data displayed in Fig. A.1(b). (a) The weight fractions of the Fe_2B phase and Fe allotropes as a function of temperature, (b) The Fe_2B a lattice parameter as a function of temperature compared against the fcc Fe a lattice parameter and, (c) the a lattice parameter for bcc Fe as a function of temperature. All axes are scaled using geometric relationships between the lattice parameters of each structure.

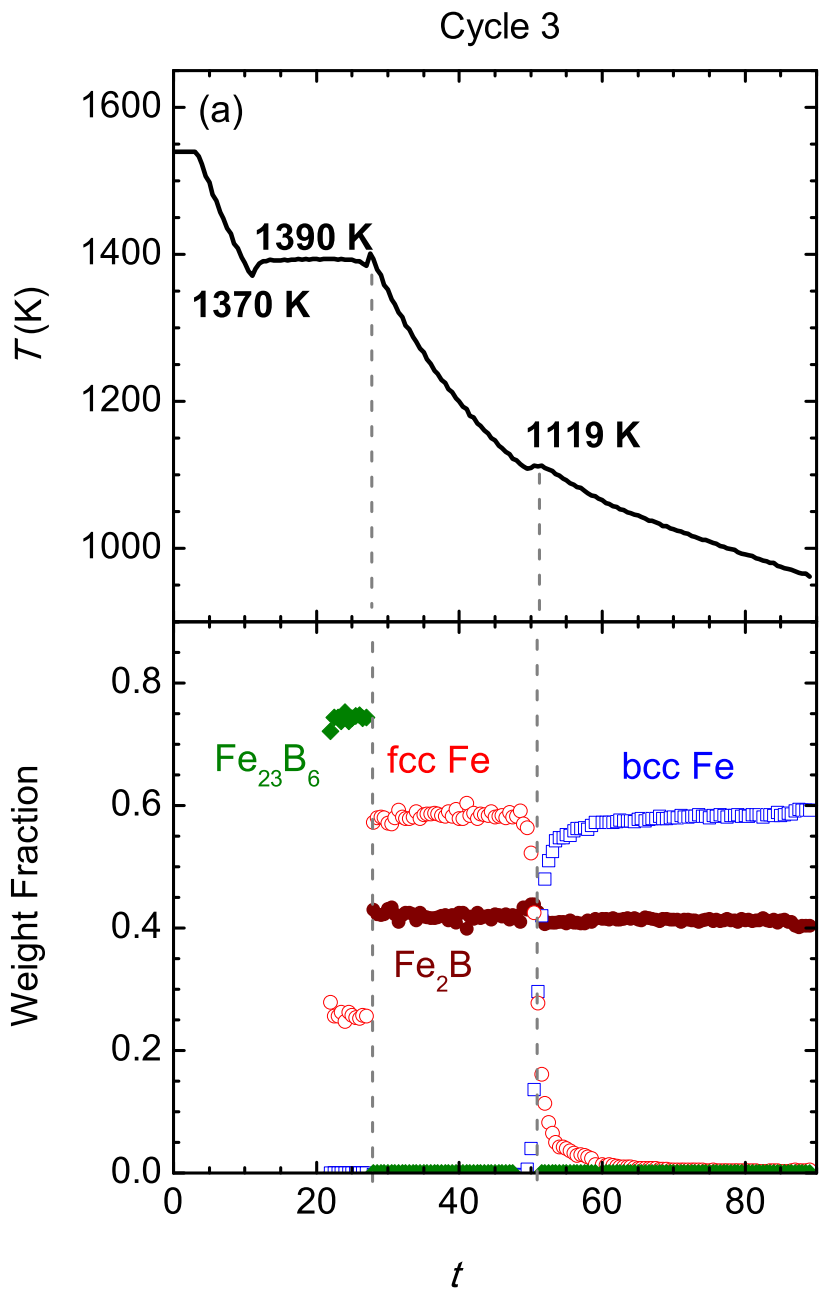

Figure 3.5: (color online) (a) Sample temperature curve determined from the pyrometer data taken during Cycle 3. The plateau from 10 to 28 seconds corresponds to the initial formation of the metastable phase. The second recalescence to 1401 K indicates relaxation into the equilibrium Fe_2B + Fe(fcc) phases. The event at approximately 46 seconds corresponds to the allotropic fcc to bcc transition in Fe on cooling. (b) The weight fractions of the $Fe_{23}B_6$, Fe_2B and Fe allotropes, starting from the earliest time in the solidification that sequential rietveld refinement converged.

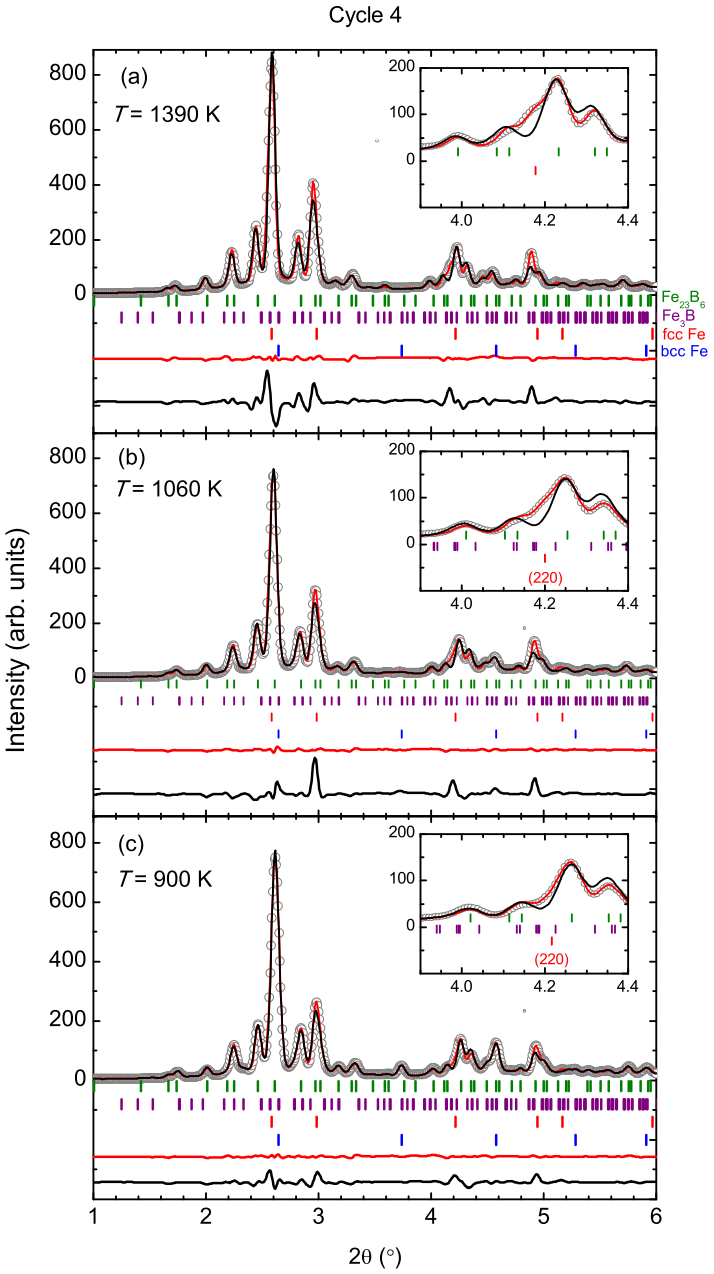

Figure 3.6: (color online) Refinements of the x-ray data taken on cooling into the metastable $Fe_{23}B_6$ + Fe phases during Cycle 4 (a) after solidification is complete, (b) during the Fe allotropic transformation, and (c) at the lowest recorded temperature. The red line corresponds to the best calculated pattern with all phases included, while the black is the pattern calculated from the same set of parameters refined without including *fcc* Fe. The insets show an expanded view near the positions of the (2 2 0) *fcc* Fe diffraction peak. The (2 2 0) *fcc* Fe diffraction peak appears as a shoulder on the low-angle side of a relatively strong diffraction peak from $Fe_{23}B_6$. The green, blue and red, and purple hash marks denote the calculated positions of diffraction peaks from $Fe_{23}B_6$, *bcc* Fe, *fcc* Fe, and Fe_3B, respectively. The residual from the final fit to the experimental data is shown in red, while the second line, in black, shows the residual to the fit not including the *fcc* Fe.

over the entire sequence of fits are quite reasonable, ranging from 0.037 at high temperature to 0.046 at 900 K. All diffraction peaks in the pattern were successfully indexed at all temperatures. The insets to Fig. A.2 show an expanded view of the diffraction patterns in the region of the most prominent *fcc* and *bcc* Fe Bragg peaks. Above the allotropic transition, no evidence of the *bcc* Fe (2 0 0) Bragg peak is found, but it is clearly present during the transition and for temperatures below the transition. The residual intensity close to the *fcc* Fe Bragg peak position arises from the near coincident positions of diffraction peaks from the Fe_2B phase.

The results of the refinements of the x-ray data in Cycle 2 are summarized in Figs. A.3 and 3.4. Figure A.3(a) displays the sample temperature as a function of time during the measurement. For this run, approximately 30 K of undercooling (below the solidification plateau of Fe_2B) was attained before the metastable $Fe_{23}B_6$ phase first appeared. Very quickly ($\sim$ 2 seconds later) the sample solidifies into the equilibrium Fe_2B + Fe equilibrium phases. The distinct anomaly in the cooling curve at $t = 42$ seconds corresponds to the allotropic *fcc* Fe to *bcc* Fe transition. Figure A.3(b) shows the relative weight fractions of Fe_2B, *bcc* Fe, and *fcc* Fe as a function of temperature determined from our refinements. The statistical uncertainty in the phase fractions is 1% as judged from the scatter in the data of Figure A.3(b). The allotropic transition in Fe is sharp and well-defined at the temperature indicated in Fig. A.3(a).

Figure 3.4 shows the temperature evolution of the weight fractions [Fig. 3.4(a)] and lattice parameters [Fig. 3.4(b) and (c)] of the various crystalline components, all derived from the refinement of the diffraction data. The weight fraction of the intermetallic Fe_2B phase remains constant over the entire temperature range and we find a sharp transition from *fcc* Fe to *bcc* Fe at approximately 1123 K, somewhat lower than the equilibrium transition temperature of 1185 K, as expected for a first-order transition on cooling.

Fig. 3.5 shows the results from pyrometry obtained during Cycle 3 as well as the weight fractions calculated from our refinements of the x-ray data. At high temperature, $Fe_{23}B_6$ is the primary phase with a small amount of *fcc* Fe, but it transforms rapidly into the equilibrium phases seen in Cycle 2. After the second recalescence event, all obtained refinement results were nearly identical to that of Cycle 2. The phase fractions shown here match those shown in Fig. 3.4 for Cycle 2 closely.

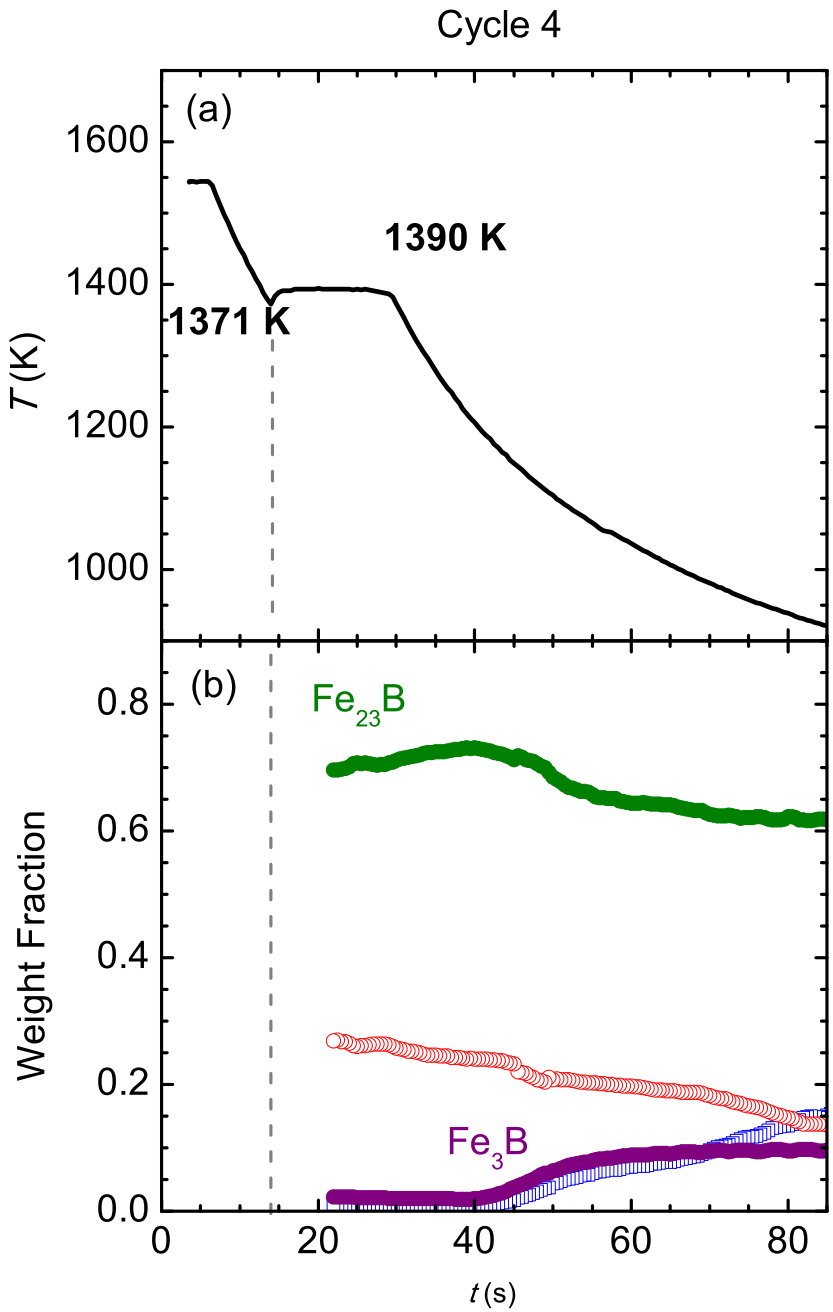

Figure 3.7: (color online) (a) Sample temperature curve determined from the pyrometer data taken during the high-energy x-ray diffraction measurement of Cycle 4. The initial temperature signature corresponds to the solidification of the metastable $Fe_{23}B_6$ + Fe phases. Note the absence of a distinct signature of the *fcc* to *bcc* transition for Fe as compared to the data in Fig. 3.4(b). The weight fractions of the $Fe_{23}B_6$, Fe_3B, and Fe allotropes as determined from the sequential Rietveld refinements of the diffraction data.

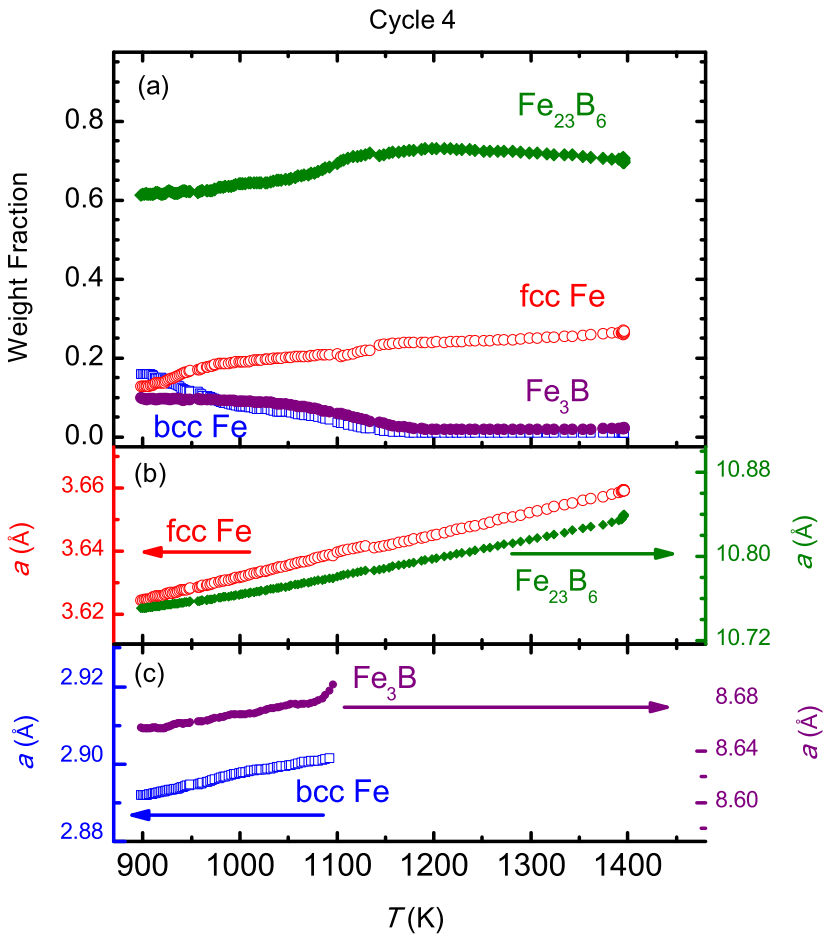

Figure 3.8: (color online) Results of the Rietveld refinement of the diffraction data displayed in Fig. A.1(d). (a) The weight fractions of the $Fe_{23}B_6$ phase and Fe allotropes as a function of temperature, (b) The cubic a lattice parameters as a function of temperature and, (c) the cubic a lattice parameters for bcc and fcc Fe as a function of temperature. Note the extended temperature range of the fcc to bcc transition and coexistence of the Fe allotropes on cooling.

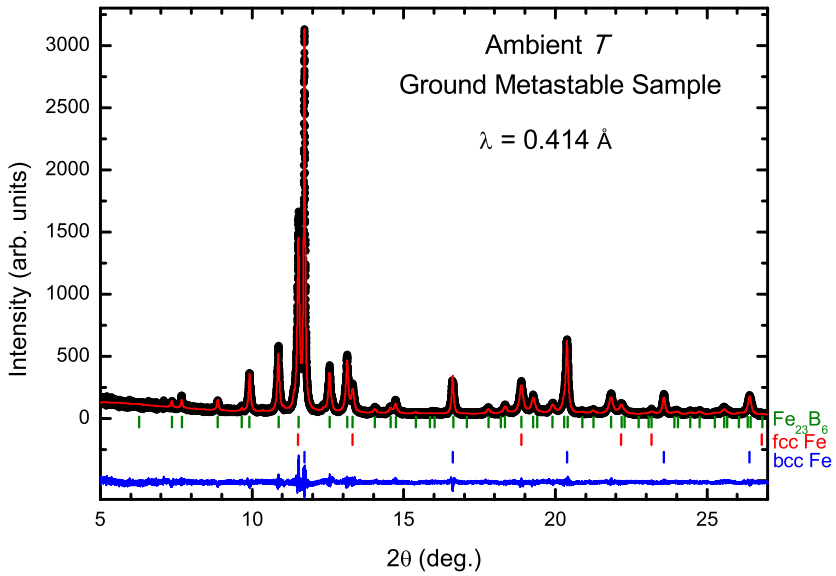

Figure 3.9: (color online) Rietveld refinement of x-ray diffraction data taken on powder produced from a levitation processed sample exhibiting behavior corresponding to metastable phase formation. Green tick marks represent $Fe_{23}B_6$, red *fcc* Fe, and blue *bcc* Fe. The blue line below the pattern represents the residual difference between the observed data and the refined fit.

3.3.3 Cycle 4: Liquid → $Fe_{23}B_6$

The refinements of the x-ray data obtained on free-cooling the sample illustrated in Cycle 4 indicate quite different behavior. The refinements at three temperatures during free-cooling are shown in Fig. 3.6. In contrast to what was found for Cycles 2 and 3, we find that the $Fe_{23}B_6$ metastable phase persists down to at least 900 K. The R-factors (R_p) for each refinement over the entire sequence of fits are again quite reasonable, ranging from 0.037 at high temperature to 0.033 at the lowest temperature measured. The insets to Figure 3.6 show an expanded view of the diffraction patterns in the region of the most prominent *fcc* and *bcc* Fe Bragg peaks. Above the allotropic transition, no evidence of the *bcc* Fe (2 0 0) Bragg peak is found, and the *fcc* Fe (2 2 0) Bragg peak appears as a low-angle shoulder on a relatively strong diffraction peak from $Fe_{23}B_6$. This shoulder decreases in intensity as temperature is lowered. However, it can still be seen at $T = 900$ K, well below the equilibrium *fcc* Fe to *bcc* Fe transition. In addition, several low intensity peaks were successfully indexed to a primitive tetragonal form of Fe_3B [27]. Inclusion of this phase improved the fit at the lowest temperature.

The results of the refinements to this series of diffraction data are summarized in Figs. 3.7 and 3.8. Figure 3.7 displays the sample temperature as a function of time during the measurement. For this run, approximately 20 K of undercooling below the solidification plateau of $Fe_{23}B_6$ (corresponding to a 70 K undercooling relative to the solidification plateau of Fe_2B) was realized before recalescence of the metastable $Fe_{23}B_6$ + *fcc* Fe phases. In contrast to Cycle 3, however, no clear evidence of a transformation to the equilibrium intermetallic Fe_2B structure was found down to the lowest temperature measured during this experiment ($\sim$ 900 K). We further note that we found no evidence of a transformation to Fe_2B down to a temperature of 600 K in cooling curves obtained using the ISU-ESL[62].

Figure 3.8 shows the temperature evolution of the weight fractions [Fig. 3.8(a)] and lattice parameters [Fig. 3.8(b) and (c)] of the crystalline components, again derived from the refinement of the diffraction data. The weight fraction of the metastable $Fe_{23}B_6$ phase remains relatively constant over the entire temperature range, although we see a small decrease in the amount of the phase below the onset of the *fcc* to *bcc* transition for the Fe fraction of the sample. Rather than the sharp transition from *fcc* Fe to *bcc* Fe described above in the presence of Fe_2B, there is only a gradual increase (decrease) in the weight fraction of *bcc* (*fcc*) Fe commencing at approximately 1150 K. Furthermore, the onset of the transition to *bcc* Fe is accompanied by the appearance of the primitive tetragonal Fe_3B phase. The weight fraction of Fe_3B increases at the same rate as the *bcc* Fe until leveling out below 1050 K. Even at the lowest temperature measured during the free cooling cycles, a finite weight fraction ($\sim$10%) of *fcc* Fe is observed, well below the equilibrium *fcc* Fe to *bcc* Fe transition.

However, the conversion of *fcc* Fe to *bcc* Fe apparently continues at lower temperatures. After Cycle 4, this sample was ground into powder and studied at station 11-BM-B at the APS. The refinement of this powder data, shown in Fig. 3.9, found that $Fe_{23}B_6$, with a lattice parameter of 10.7138(1) Å, comprised 65% of the sample by weight with the balance identified as *bcc* Fe ($\sim$35%). The refinement also indicated that, if present at all, the weight fraction of *fcc* Fe was less than a 1%. A more precise determination of the *fcc* Fe fraction was hampered by the near coincidence of all *fcc* Fe peaks with those from $Fe_{23}B_6$, and cooling the sample

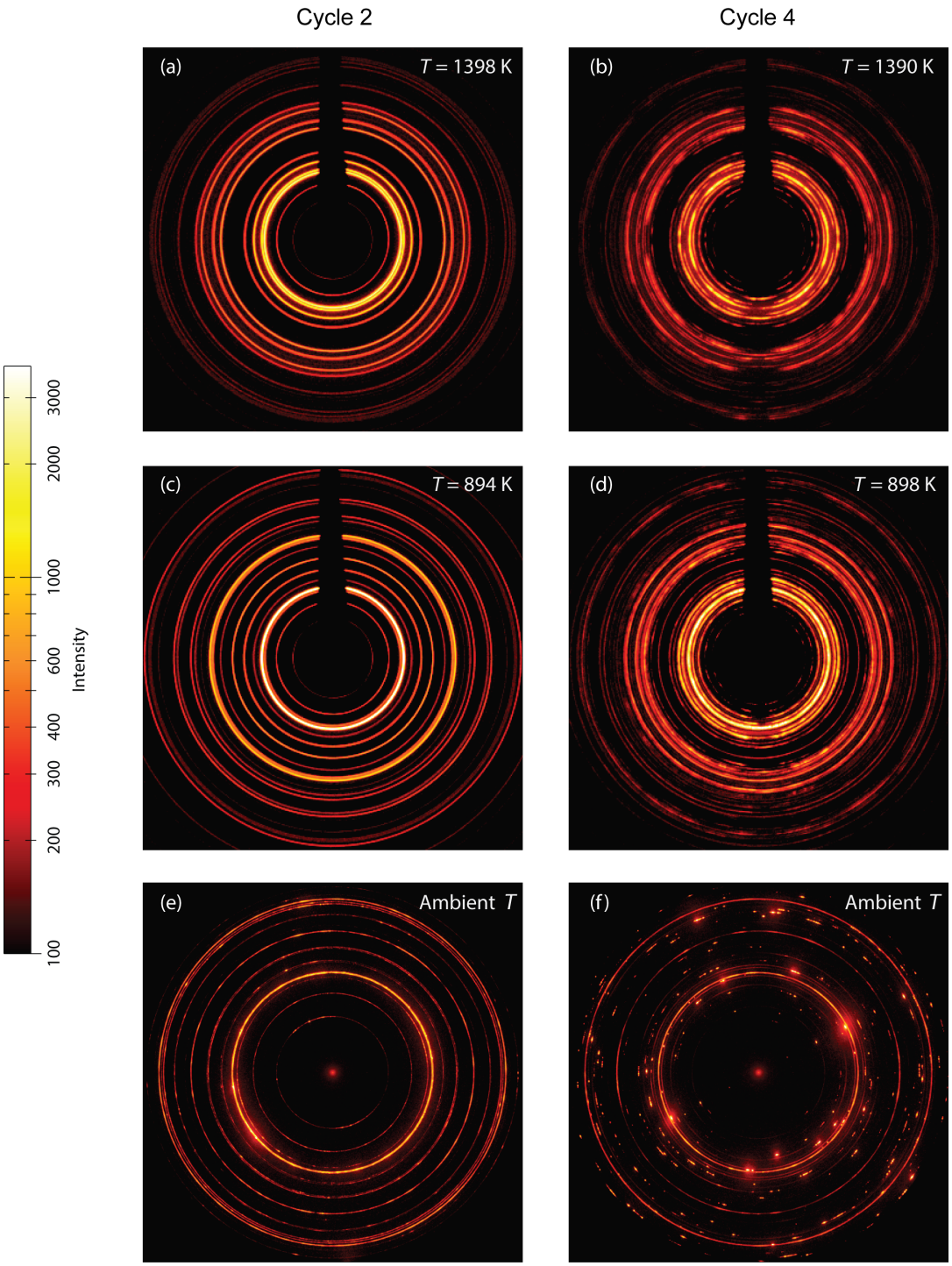

Figure 3.10: (color online) Several frames of background-subtracted x-ray patterns. (a)-(d) were obtained during the cycles in the BESL presented earlier while (e)-(f) were obtained at ambient temperature on samples processed in the ISU-ESL. (a) Equilibrium solidification of Fe_2B + *fcc* Fe during Cycle 2 directly after the solidification plateau at 1410 K, (c) Same sample a short time later at 900 K with Fe_2B+ *bcc* Fe. (b) Frames from Cycle 4 with $Fe_{23}B_6$ + *fcc* Fe immediately after solidification (d) Same cycle at 900 K with $Fe_{23}B_6$ + Fe_3B + *fcc* Fe + *bcc* Fe present. (e) Sample showing the same thermal profile in the ISU-ESL as those in Cycle 2 (f) Sample with a thermal history resembling that in Cycle 4.

down to 100 K failed to conclusively distinguish any of the *fcc* Fe peaks. Likewise, the weight fraction of Fe_3B present at ambient temperature was determined to be less than 1% by weight.

3.3.4 Evidence for the coherent growth of *fcc* Fe and $Fe_{23}B_6$

The data presented in the previous subsection demonstrates that both *fcc* Fe and $Fe_{23}B_6$ persist down to much lower temperatures than previously reported. To gain some insight into the mechanism for stabilizing these phases we turn to the raw 2D diffraction patterns in Figures 3.10 and 3.11. The pattern in Fig. 3.10(a) was taken immediately following solidification into the equilibrium Fe_2B +*fcc* Fe phase (Cycle 2), and Figure 3.10(b) shows a pattern upon crystallization into the metastable $Fe_{23}B_6$ phase (Cycle 4). Here, we see that a significantly higher degree of texturing is observed for solidification into the metastable $Fe_{23}B_6$ phase than for the equilibrium Fe_2B product. Figures 3.10(c) and (d) display the raw 2D diffraction patterns taken at the lowest temperatures measured, where the same trend in texturing is observed. Figure 3.10(e) shows the ambient temperature diffraction pattern from a sample solidified into the equilibrium Fe_2B + Fe phases in the ISU-ESL, whereas Figure 3.10(f) displays ambient temperature diffraction pattern from a sample that solidified into the metastable $Fe_{23}B_6$ + Fe phases, also processed in the ISU-ESL. The striking difference in grain size is consistent with the texturing in the $Fe_{23}B_6$ observed at all temperatures.

Figure 3.11 presents an enlarged portion of a diffraction pattern taken just after solidification on a sample that has formed the $Fe_{23}B_6$ phase. Of note is the coincidence of features in the Debye rings from the *fcc* Fe and $Fe_{23}B_6$ phases, most visible in the *fcc* Fe 220 and $Fe_{23}B_6$ 660 diffraction rings, as well as the *fcc* Fe 222 and $Fe_{23}B_6$ 666 rings. All incomplete arcs of these rings match perfectly between the two phases, indicating a shared orientation.

At 900 K, the lowest temperature recorded during free cooling, the lattice parameters for $Fe_{23}B_6$ and *fcc* Fe are found to be 10.7513(3) Å and 3.6258(4) Å, respectively. This corresponds to a ratio of 2.965, or a 1.2% lattice mismatch. The small mismatch, the shared texturing in the raw data, and the apparent necessity of the existence of the $Fe_{23}B_6$ phase for the persistence of the *fcc* Fe phase below the allotropic transition together indicate coherent intergrowth between the two phases.

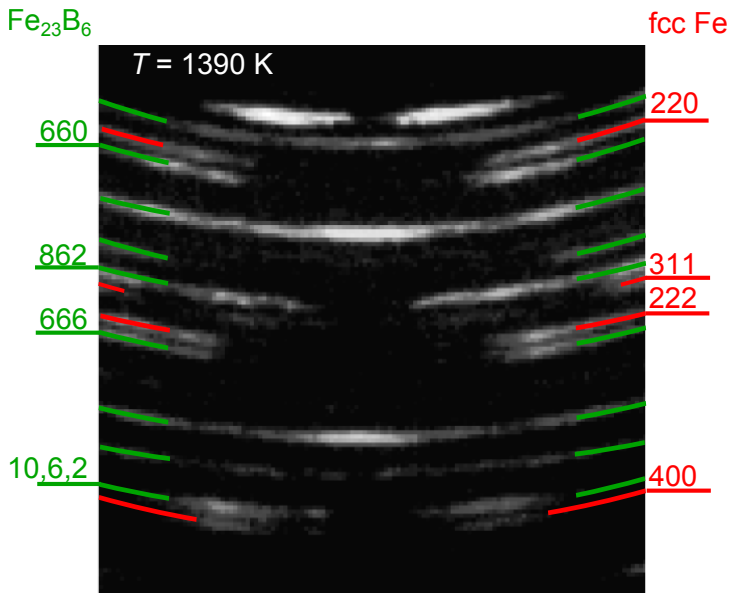

Figure 3.11: (color online) An enlarged section of a frame from Cycle 4, taken immediately following solidification at 1390 K. The green labels on the left indicate the *hkl* index for each ring belonging to $Fe_{23}B_6$, while the red indices on the right delineate the *fcc* Fe rings.

3.4 Summary and Discussion

Our high-energy x-ray diffraction have resulted in several interesting results. The solidification of the Fe_2B + Fe phase, illustrated in Cycle 1 and 2, is expected and the calculated weight fractions reasonably match the stochiometry of the sample to within a few percent. The allotropic transition in Fe is observed slightly lower than in previous reports, but this is most likely due to achieving some small degree of undercooling. From the 2D data available at both high and low temperatures, the phases appear to be well dispersed, as evidenced by the smooth diffraction rings.

The second solidification mode, however, provides some insight into the stabilization of the metastable *fcc* Fe phase. Whereas the growth and persistence of metastable $Fe_{23}B_6$ have been recognized for some time, previous investigations have suggested that its stability is dependent on a high cooling rate [45], and other solidification studies indicate Fe_3B as the initial solidified phase. In contrast to these results, the samples studied here show no dependence on cooling rate on either formation of the metastable $Fe_{23}B_6$ phase, or its persistence to lower temperatures. After several initial melt cycles, exhibiting minimal evaporative mass loss or variation in melting

temperature, the $Fe_{23}B_6$ phase generally nucleates before any equilibrium phases in the manner of Cycle 2 or 3. The two subsequent behaviors, transformation to the equilibrium Fe_2B phase during the solidification plateau or persistence of the $Fe_{23}B_6$ phase to lower temperatures, occur in seemingly random order in consecutive cycles. The consistent randomness of the solidification product, in comparison to past observations, may be a result of high temperature cleaning or mixing. While there is no clear evidence of $Fe_{23}B_6$ in those solidifications resembling Cycle 1, any precipitation of a metastable precursor that occurs on a fast timescale could be difficult to resolve at the 8 frames per second Cycle 1 was acquired at.

In addition, in previous studies finding persistent $Fe_{23}B_6$, either *fcc* Fe was not detected or the data were not fully refined [45, 46]. Here, the clear presence of *fcc* Fe is confirmed via refinement, at both high and low temperatures. The raw data reveals that these two phases are highly textured, with large grains appearing to grow coherently with each other. While the *bcc* Fe appears around the expected temperature, the transformation is slow. In addition, Fe_3B is shown to appear simultaneously with *bcc* Fe and the fractions of both phases increase together. Previous work on $Fe_{80}B_{20}$ using electron microscopy has shown that the *bcc* Fe phase grows coherently with Fe_3B [25]. In direct contrast to the other phases present, both the *bcc* Fe and Fe_3B appear to be more finely dispersed in the raw data (Fig. 3.10).

Careful analysis of the lattice parameters of all observed phases reveals a few key relationships. Previous work growing pseudomorphic thin films of *fcc* Fe on Cu (001) was successful with a 1% epitaxial mismatch [150], and the *bcc* form of Fe was successfully grown with a mismatch of 1.35% [151]. The lattice mismatch found in this study of 1.2% is close to these results and a plausible value for heteroepitaxy. While *fcc* Fe layers formed on the $Fe_{23}B_6$ may be strained to match the $Fe_{23}B_6$, our measurements only reveals the average lattice constant of the grains, and are insensitive to deformations of the few layers near the boundary between the two phases. The difficulty in confirming whether *fcc* Fe is retained at ambient temperature may result from the near coincidence of diffraction peaks from $Fe_{23}B_6$ and *fcc* Fe due to a further decrease in lattice mismatch with lowered temperature. Large grains visible on the Debye rings corresponding to both $Fe_{23}B_6$ and *fcc* Fe at ambient temperature may indicate the continued presence of the *fcc* Fe, but cannot be quantified without further experiments.

Here the epitaxial relationship between the $Fe_{23}B_6$ and *fcc* Fe likely provides a mechanism for the retention of *fcc* Fe by imposing a kinetic limitation on the allotropic transition. It is likely that this coherency also facilitates the formation and retention of the $Fe_{23}B_6$, as the *fcc* Fe is an equilibrium phase at the solidification temperature. The full details of this stabilizing mechanism cannot be entirely explained based on the data presented here, but is certainly worth further study. The nature of this growth raises questions about similar binary systems. For example, one might expect formation of an $Fe_{23}C_6$ structure in the Fe-C binary system. However, to our knowledge, the $Fe_{23}C_6$ structure is rarely observed in the binary, and more generally seen as a secondary product in materials composed of at least three components. Previous work investigated the properties and stability of this phase, with the most stable lattice parameter predicted to be 10.4668 Å[48], while the lattice parameter of $Fe_{23}C_6$ in $(Fe_{0.8}Cr_{0.2})_{79}B_{17}W_2C_2$ was determined experimentally to be 10.639 Å[152]. All reported values are smaller than the lattice parameter of $Fe_{23}B_6$ observed here and should lead to a larger lattice mismatch between the $Fe_{23}C_6$ and *fcc* Fe phases, possibly preventing stabilization via coherent growth between them. This mismatch may explain the rarity of $Fe_{23}C_6$ in binary Fe-C alloys, and is worth investigation.

The *fcc* Fe lattice parameter given here, slightly larger at this temperature than previously reported, also lends further motivation to a study of the magnetic structure of the material. Previous attempts to grow *fcc* Fe, as thin films grown epitaxially on a copper substrate [153–160] or in the bulk in Cu or Cu-Au matrices [161–164], resulted in lattice parameters between 3.57 Å and 3.75 Å, with the mixed magnetic properties of the films highly dependent upon preparation conditions. Theoretical work has previously established that a *fcc* Fe lattice parameter below 3.57 Å would exhibit FM ordering, while a value of or above 3.62 Å could yield a high-spin FM ordering state [165]. If *fcc* Fe is present in these samples to lower temperatures, as the observed trend in phase fractions seem to indicate, it can be estimated from the $Fe_{23}B_6$ lattice parameter that the *fcc* Fe phase would have a lattice parameter of about 3.61 Å at ambient temperature. This lattice parameter would be in the middle of this range, larger than those predicted to exhibit AFM ordering and smaller than those with high-spin FM ordering.

Further studies detailing the existence and potential magnetic ordering of the fcc Fe phase at lower temperatures are in progress.

CHAPTER 4. IN-SITU INVESTIGATION OF MAGNETISM IN METASTABLE PHASES IN LEVITATED $FE_{83}B_{17}$

This chapter is currently being considered for publication as a letter in *Physical Review: Applied*. It was drafted in collaboration with D. Messina, G.E. Rustan, A. Kreyssig, and A.I. Goldman. The author prepared samples, performed all experiments, analyzed all data, and drafted the manuscript. D. Messina assisted during sample preparation and the BESL run in 2016. G.E. Rustan performed the initial experiments that led to those performed here, and was the driving force behind the implementation of the TDO. A. Kreyssig and A.I. Goldman assisted in editing the manuscript.

Thermophysical properties such as density, specific heat, viscosity, surface tension, emissivity, conductivity and magnetization provide valuable insight into the nature of the metastable solids and liquids, and critical data for quantitative modeling of phase selection and solidification. However, metastable phases at high temperature are notoriously difficult to characterize, particularly when environmental contamination is of concern. Nevertheless, the ability to determine *in-situ* both the structure and properties of these metastable phases, their formation with composition and temperature, and their role in the formation or inhibition of stable phases at lower temperatures can add tremendously to our understanding of stable phase formation in complex systems.

The Fe-B binary system has been the subject of intense study for decades since it is a constituent of magnetic materials critical to a number of industries[166–168] as well as the essential component of a number of metallic glasses[13, 169]. Devitrification experiments on glassy samples have observed an abundance of metastable phases, such as primitive tetragonal

(pt) Fe_3B, body-centered tetragonal (bct) Fe_3B, orthorhombic (o) Fe_3B, and cubic $Fe_{23}B_6$. *In-situ* studies [44, 141, 45] have provided some new insights into the solidification pathways in eutectic $Fe_{83}B_{17}$. In particular our recent *in-situ* high-energy x-ray studies[146, 132] of of $Fe_{83}B_{17}$ have revealed that this alloy solidifies either directly into the equilibrium Fe_2B + fcc-Fe phases, or a metastable phase mixture of $Fe_{23}B_6$ + fcc-Fe that, subsequently, either transforms to the equilibrium high-temperature phases (Fe_2B + fcc-Fe) or persists down to ambient temperature. The selection of the solidification pathway for any given sample or heating cycle appears to be a stochastic process, and the sequence of solidification products for samples where the metastable $Fe_{23}B_6$ phase persists to ambient temperature is quite complex. For example, in these instances, the $Fe_{83}B_{17}$ phase is accompanied by the presence of coherently grown fcc-Fe which also persists to temperatures well below the allotropic fcc - bcc transition at ∼1150 K on cooling, and the metastable pt-Fe_3B is also observed at lower temperatures.

Given the past emphasis on the magnetic properties of the $Fe_{23}B_6$ phase[32], as well as extensive investigations into the magnetism of fcc Fe structures stabilized on a variety of substrates[170–172], there is considerable interest in the nature and formation of magnetism in these non-equilibrium metastable phases. The complex nature of the solidification, however, requires a probe that is well suited to the challenges of high temperature, the time dependence of the solidification process itself, and the requisite sensitivity to detect the subtle signals of the emergent magnetism. To overcome these challenges, the containerless processing environment of an electrostatic levitation furnace has been combined with a tunnel-diode oscillating (TDO) circuit for precision contactless measurements of dynamic magnetic susceptibility[93, 62]. While the TDO method has traditionally been employed as a highly sensitive probe of resistivity, susceptibility, and london penetration depth in the low temperature regime[173], here it has been adapted for use in high temperature processing.

Applied concurrently with simultaneous volumetric measurements, and correlated with high-energy x-ray diffraction experiments for phase determination, we have identified and characterized a number of magnetic transitions during the solidification of $Fe_{83}B_{17}$. Several new results, including an enhanced magnetic ordering temperature for $Fe_{23}B_6$ and the possibility

of a magnetic contribution to the driving force for the allotropic fcc-Fe - to - bcc-Fe transition are obtained from our measurements.

$Fe_{83}B_{17}$ ingots were prepared by arc melting 99.99% pure Fe from Toho Zinc Corporation and 99.9999% pure B from Alfa Aesar under a reducing atmosphere. The ingots were broken into 30 to 80 mg chunks and laser melted several times on a polished graphite surface, first under forming gas and then under high vacuum ($\sim 10^{-7}$ torr), to form spheres for levitation. All material was carefully weighed several times throughout processing to monitor any evaporative mass loss, and a Leco CS-444 carbon determinator was used to ensure there was no appreciable carbon contamination from the graphite substrates.

The samples were levitated in the ISU-ESL[93, 62] where controlled heating and cooling ramps were accomplished using a PID algorithm in the LabVIEW laser control program at a rate of 2 K/s. Free cooling cycles were accomplished by simply turning off the laser. The data presented here were taken on a 43 mg sample, exhibiting $\sim$0.1 mg of mass loss through the course of 10 heating and cooling cycles. Volumetric measurements were performed in the ISU-ESL using a well established videographic algorithm [79**?** , 62] and were performed concurrently with the TDO measurements to ensure that the observed magnetic transitions could be correlated consistently with the x-ray data.

The ISU-ESL TDO is described in detail in Refs. [93] and [62]. Briefly, a copper coil was installed in the bottom electrode of the ESL and connected to a tank circuit driven by a tunnel diode biased to the region of negative differential resistance on its $V(I)$ curve. Samples levitating above the coil are inductively coupled to coil (inductor) of the oscillator circuit and changes in the sample conductivity and/or magnetization result in a shift of the circuit's resonant frequency $f_0 = (2\pi\sqrt{LC})^{-1}$:

$$\frac{\Delta f}{f_0} = \frac{3}{4}\phi\Big(1 - \frac{3\delta}{2a}(1+\chi)\Big) \tag{4.1}$$

where Δf is the shift in frequency, f_0 is the resonant frequency of the empty circuit without the sample, ϕ is the sample filling factor, and $\chi = \mu - 1$ is the magnetic susceptibility. In general, the frequency shift is proportional to the total magnetic susceptibility of the sample, which consists of both skin-effect diamagnetism and electronic magnetism, either dia- or para-

depending on the situation. The latter contributes from the skin depth layer accessible to the AC excitation field. As we show below, the onset of magnetic ordering can produce frequency shifts of 10^2-10^3 Hz.

High-energy x-ray diffraction measurements were performed at Beamline 6-ID-D (λ = 0.09411 Å, E = 131 keV) at the Advanced Photon Source (APS) at Argonne National Laboratory. The samples were levitated in the Washington University Beamline Electrostatic Levitator (WU-BESL), a more detailed description of which can be found in Ref. [99], using a similar procedure to the one described in Ref. [132]. A two-dimensional GE Revolution 41-RT amorphous silicon flat-panel detector was used for rapid acquisition of diffraction patterns in transmission geometry, with ∼88% transmission through the sample. Data presented here were obtained at 1 frame per second on a 46 mg sample. No automated temperature control was available but efforts were made to match the ramp rates used for the TDO study. Gaps in the x-ray data are due to detector memory limits on continuous acquisitions. ImageJ[149] was used to correct diffraction images for dark current and background. Fit2D[116, 174] was used to determine detector distance, correct for detector rotation and tilt, and azimuthally integrate the 2D data. GSAS[175] was used for all sequential Rietveld refinements.

In Fig. A.1 we show the x-ray, volumetric and TDO data for a cooling/heating cycle where the $Fe_{83}B_{17}$ sample solidifies into the equilibrium Fe_2B + *fcc*-Fe phases from the melt. On cooling from the melt, Fe_2B is the primary equilibrium phase, accompanied by *fcc*-Fe at high temperature which transforms to *bcc*-Fe near T = 1150 K. The transformation of *fcc*-Fe to *bcc*-Fe represents a shift in average volume per Fe atom from 12.188 Å^3/atom to 12.238 Å^3/atom, which is reflected in the cooling curve in Fig. A.1(c) as an expansion at the transition. On heating, the transformation from *bcc*-Fe to *fcc*-Fe is observed in the x-ray data at 1220 K, and the corresponding volume contraction is seen in Fig. A.1(c) at nearly the same temperature.

The TDO data in Fig. A.1(d) exhibits a sizeable frequency shift (proportional to the magnetic susceptibility of the sample) at 1040 K, with a magnitude of 1080 Hz, signifying a large increase in magnetic susceptibility corresponding to the onset of magnetic ordering. This temperature closely matches the known Curie temperature (T_C) for the onset of ferromagnetism for *bcc*-Fe of 1043 K. On heating, a comparable decrease in frequency is observed at the same

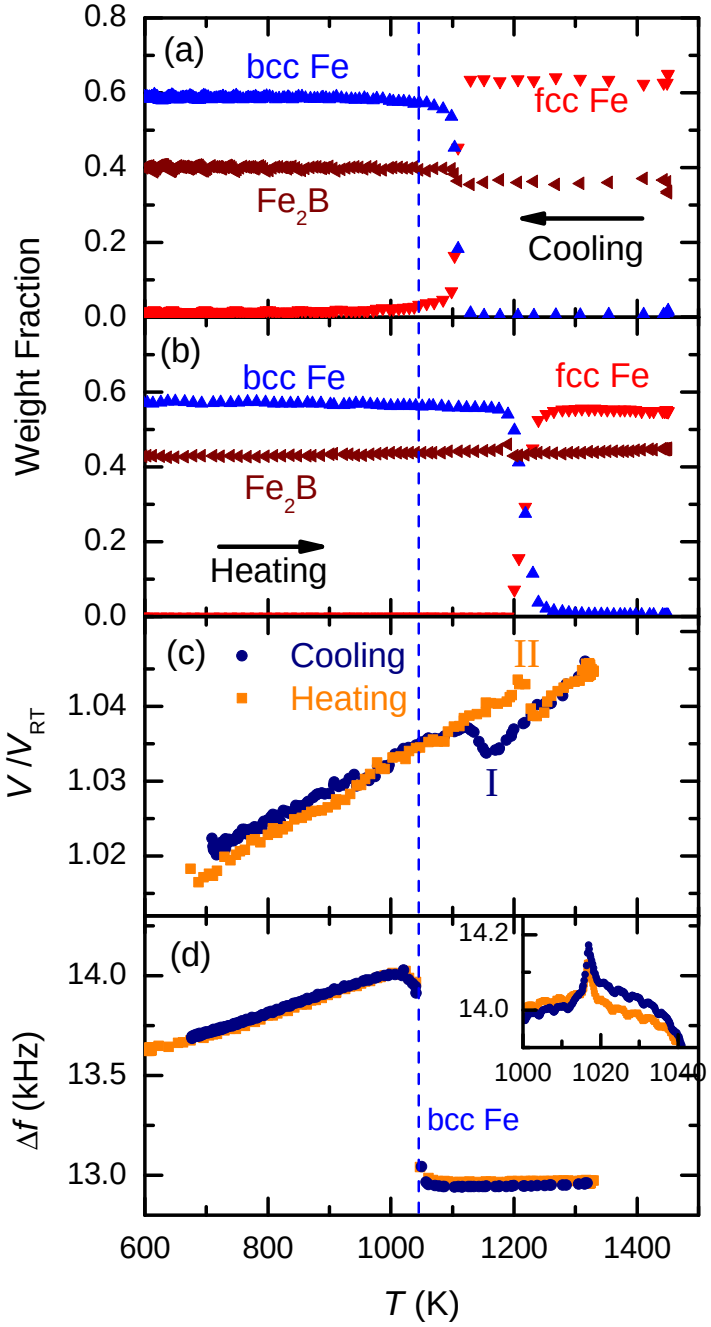

Figure 4.1: (color online) (a) and (b) Results of Rietveld refinements of the x-ray data. The red triangles represent *fcc*-Fe, blue triangles represent *bcc*-Fe, and the brown triangles represent Fe_2B. Weight fractions in panel (a) were measured on cooling, and those in (b) were measured on heating. (c) Volumetric data taken in the ISU-ESL. Temperatures labeled as I and II denote the allotropic transition on cooling and heating, respectively. (d) Frequency shift measured by the TDO circuit. The inset displays the peak near 1018 K taken on a similarly-sized sample with data taken at a lower cooling and heating rate (∼0.25 K/s) for higher resolution. Dark blue circles correspond to cooling and orange squares represent the subsequent reheat. The volume is represented as a fractional change from ambient temperature values to more easily compare to the results from the x-ray data.

temperature, signaling the transition from ferromagnetic order below, to paramagnetism above, T_C. Furthermore, there is a small but persistent peak at 1018 K. The well-established T_C for Fe_2B of 1015 K[18] allows us to identify this feature as arising from the ferromagnetic ordering of Fe_2B. Both the shape and the magnitude of this feature, however, are quite different from the step-like TDO frequency shift observed for the ferromagnetic ordering of *bcc*-Fe.

Extensive investigations into the TDO response to magnetic transitions have determined that the large, step-like increases in the frequency shift are associated with the onset of itinerant ferromagnetism[108], consistent with the itinerant magnetism in *bcc*-Fe. On the other hand, ferromagnetic transitions in local moment systems demonstrate small, sharp peaks in the frequency shift[108, 110] due to critical fluctuations. We note that there is some evidence for local moment magnetism in Fe_2B[176], consistent with the shape and small frequency shift of the transition with respect to the Fe_2B weight fraction. These measurements further demonstrate that the nature of the ordering (local vs. itinerant) in magnetic materials, as well as the ordering temperature itself, may be elucidated through TDO measurements.

We now turn to our measurements, displayed in Fig. A.2, for a cooling/heating cycle where where the $Fe_{83}B_{17}$ sample solidifies into the metastable $Fe_{23}B_6$ + *fcc*-Fe phases from the melt. In order to ensure that we capture the kinetics of the metastable phase transitions with temperature, all of these data were taken while free-cooling the sample from high temperature. Fig. A.2(a) and (b) are again the calculated weight fractions from the Rietveld refinements of the x-ray data during cooling and heating, respectively, and are consistent with our previous results[146, 132]. In addition to the persistence of the metastable $Fe_{23}B_6$ phase over the full temperature range probed here, several other features are noteworthy.

On cooling, the *fcc*-Fe - to - *bcc*-Fe transformation is suppressed to much lower temperature, commencing at approximately 1050 K, and is quite broad in temperature. A small weight fraction of the metastable *pt*-Fe_3B precipitates, but does not continue to grow beyond ∼5% of the sample weight. Rather than the sharp change in the volumetric data [Fig. A.1(c)] described above, the allotropic transition is reflected in Fig. A.2(c) as an inflection midway through the *fcc*-Fe to *bcc*-Fe transition region labeled I.

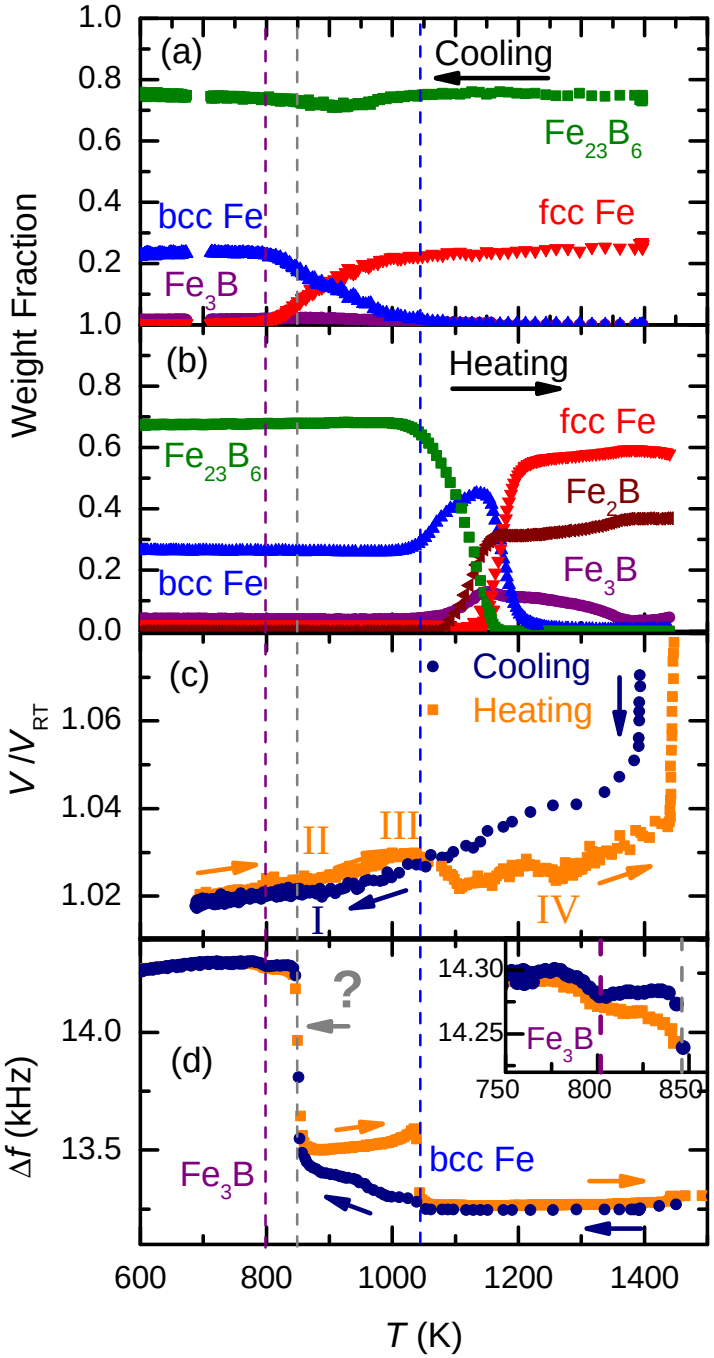

Figure 4.2: (color online) (a) and (b) display results of Rietveld refinements on x-ray data. Green squares represent $Fe_{23}B_6$, red triangles pointing down *fcc* Fe, blue triangles pointing up *bcc* Fe, brown triangles pointing left Fe_2B, and purple circles Fe_3B. Fractions in (a) were measured on cooling, and those in (b) were measured on heating. (c) Sample volume as compared to an ambient temperature measurement. Points I through IV are temperatures corresponding to transitions as described in the text. (d) The measured frequency shift in the TDO. The inset presents a detailed view of the signal near 790 K.

On heating, we note that the volume undergoes a slight increase at point II in comparison to cooling at this temperature. This feature is likely due to the continued transformation of any residual *fcc*-Fe in the sample to *bcc*-Fe as temperature is increased. The transformation from $Fe_{23}B_6$ to Fe_2B commences at approximately 1050 K, accompanied by an increase in the weight fraction of Fe_3B and *bcc*-Fe, consistent with the contraction in the volumetric data at point III in Fig. A.2(c). Finally, as the sample is heated above approximately 1375 K, the metastable Fe_3B transforms to Fe_2B and *bcc*-Fe.

Figure A.2(d) displays the corresponding TDO data for this $Fe_{83}B_{17}$ sample. In contrast to the data shown in Fig. A.1(d), on cooling there is no evidence of a sharp ferromagnetic transition at 1040 K, consistent with the absence of the *bcc*-Fe noted above. Rather, the TDO frequency shift exhibits a slow rise beginning at 1040 K, concomitant with the slow increase in the weight fraction of ferromagnetically ordered *bcc* Fe as temperature decreases. It is notable that the *fcc*-Fe - to - *bcc*-Fe transformation here is coincident with the onset of magnetic ordering. In light of previous studies of the magnetic contributions to the stability of the Fe allotropes[177], and evidence of magnetic contributions to the driving force for nucleation in undercooled liquid $Co_{80}Pd_{20}$[178], this observation suggests that magnetic interactions may play a role in the *fcc*-Fe - to - *bcc*-Fe transformation. This point certainly bears further investigations.

At $T = 850$ K, there is a large increase in the TDO frequency, again indicating a transition to a ferromagnetically ordered state. There is no known T_C among the iron borides at 850 K, with the closest belonging to *bct*-Fe_3B at 786 K and *o*-Fe_3B at 897 K [179]. The transition at 850 K is followed by a small, reversible signal at 790 K. This is most likely related to a magnetic transition in Fe_3B, being close to the reported T_C of 786 K for *bct*-Fe_3B, though far from the reported T_C of *pt*-Fe_3B. The low magnitude of the transition, 25 Hz, is reasonable given the small fraction of the sample occupied by Fe_3B (<5%). Both these signals are again present on heating, where *bcc* Fe shows a ferromagnetic to paramagnetic transition at 1040 K, with a magnitude reflecting the low weight fraction relative to that in the equilibrium solidification.

Fig. A.3 corresponds to an anneal subsequent to the cooling cycle shown in Fig. A.2(d), where the sample was heated to ∼990 K and held for eight minutes before cooling. A large volume contraction (∼1%) indicated the transformation from $Fe_{23}B_6$ to Fe_2B + Fe_3B + *bcc*

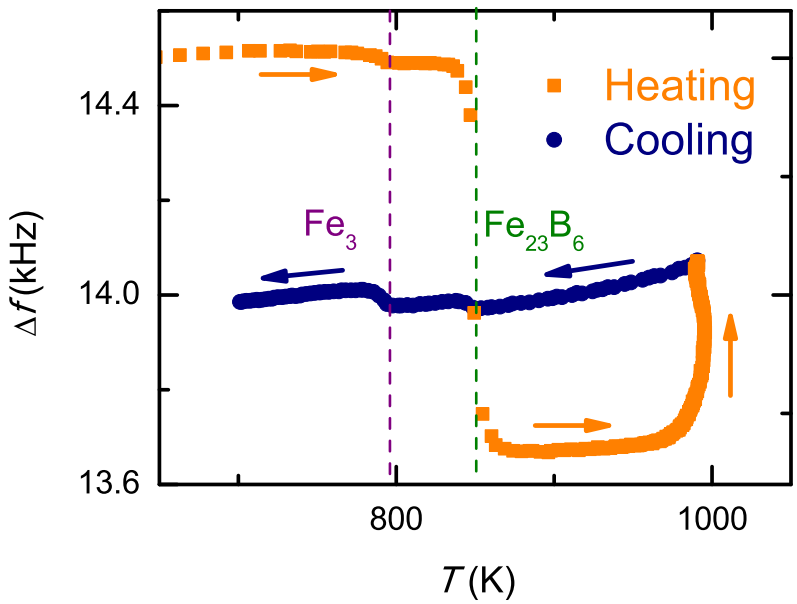

Figure 4.3: (color online) TDO output from an anneal following the solidification displayed in Fig. A.2(c) and (d), where the sample was heated to the temperature region where $Fe_{23}B_6$ transforms to Fe_2B + *bcc* Fe + Fe_3B. Orange squares represent the initial heat and eight minute anneal at 990 K, while blue circles represent the subsequent cool.

Fe. On cooling, the frequency shift at 850 K has almost disappeared, whereas the signal at 790 K is slightly enhanced. Given the expected increase in Fe_3B content and decrease in $Fe_{23}B_6$, the transition at 790 K must come from Fe_3B, and the signal at 850 K can be associated with ferromagnetic ordering in $Fe_{23}B_6$.

Studies have suggested that the flexibility of the $Fe_{23}B_6$ structure allows for different fractional occupations of the Fe sites as well as variations in bond lengths[180], resulting in noticeable differences in the magnetic order [48]. A series of investigations by Barinov et. al [181] on single phase $Fe_{23}B_6$ found a range of Curie temperatures from 623 K to 701 K, related to the Fe site vacancies and B concentration, c_B, of the structure given by $T_c = [101 + 26.1c_B]$ K. Nominally, $Fe_{23}B_6$ has a c_B of 20.7%, while our recorded T_C would require a c_B of 28.7%.

Two other explanations for the higher T_C for $Fe_{23}B_6$ seem plausible. The first, and most likely, is that this higher T_C is a result of the coherent growth of $Fe_{23}B_6$ on large grains of metastable *fcc* Fe. It is unclear from the Rietveld refinements and raw x-ray data if any of the *fcc* Fe remains at room temperature, and as past work has demonstrated[132], the overlap of peaks resulting from coherency together with extremely strong texturing make quantitative

measurements of the *fcc* Fe and $Fe_{23}B_6$ fractions challenging. The nature of the coherent stabilization might imply a kinetic barrier to further transformation at low temperature, leaving some small grains of *fcc* Fe throughout the sample, and the volume expansion seen in Fig. A.2(c) at (II) may support this.

If some *fcc* Fe is still indeed present at ambient temperatures, the possibility remains that this signal comes from stabilized *fcc* Fe clusters. There have been numerous efforts to characterize magnetic ordering in thin films of *fcc* Fe grown on Cu substrates[182] or in Cu[163] or Cu-Au[183] matrices. While *fcc* Fe is antiferromagnetic in the ground state, with a Néel temperature of 70 K[184], metastable low-temperature *fcc* Fe growth is predicted to exhibit a sensitive dependence on its lattice parameter, varying from low-spin to high-spin ferromagnetism between 3.57 and 3.62 Å [165, 185]. The lowest temperature where we have obtained a reliable lattice parameter of *fcc* Fe during the most recent course of work with the BESL yielded 3.628 Å at 850 K. This would imply any stabilized *fcc* Fe could be within the predicted high-spin regime.

The work performed by combination of x-ray diffraction, volume thermal expansion, and TDO susceptibility measurements paints a clear picture of magnetic transitions in the system. The equilibrium solidification displays the signature of ferromagnetic transitions in *bcc* Fe and what appears to be a primarily local moment ferromagnet, Fe_2B. Among the metastable phases, a transition at 790 K is ascribed to Fe_3B. A transition at 850 K can be safely attributed to a high Curie temperature phase resulting from $Fe_{23}B_6$ coherently grown with *fcc* Fe. This study provides an excellent example of the capacity of containerless instrumentation to map the magnetic phase diagram of sensitive non-equilibrium phases and high-temperature materials.

CHAPTER 5. THE STRUCTURE OF LIQUID $FE_{83}B_{17}$ AND $FE_{83}C_{17}$

5.1 Introduction

The physics of liquids has been an evolving area of study since the 1960s. Knowledge of thermophysical properties of the melt, such as viscosity and density, are crucial to many industrial casting process[60]. Advances in levitation-based containerless processing methodology combined with the development of third generation synchrotron light sources and high intensity neutron scattering laboratories over the past two decades have begun to produce a rich literature of structural studies on liquids. Combined with advances in computational power and the corresponding algorithms [186, 131], a number of studies have probed the relationship between the structure[85, 86, 187, 188] and dynamics[189, 190] of the liquid as they relate to non-equilibrium transformation processes such as the glass transition[88], liquid-liquid transitions[191], and metastable phase selection[192, 193]. By comparing structural motifs in the undercooled liquid to those in metastable phases, kinetic arguments for phase selection pathways may be made[187, 194]. Recent investigation combining x-ray and neutron scattering with computational methodology were able to compare the liquid ordering prior to solidification in ZrRh and ZrPt to those observed on solidification[92].

The Fe-B and Fe-C systems are both exhaustively well studied systems, as the former is relevant to metallic glass and permanent magnets as thoroughly detailed in Chapter 1, and the latter the foundation of steel, one of the most important and ubiquitous materials in the modern world. Many theoretical models for the liquid structure have been proposed and investigated via molecular dynamics simulations[145, 195]. However, due to the prohibitive experimental complications associated with isothermal holds of high temperature reactive liquids, experi-

mental studies of the liquid structure are scarce, with most investigations into liquid $Fe_{80}B_{20}$ and $Fe_{83}C_{17}$ being decades old[196, 197].

Here we perform a comparison study on the $Fe_{83}B_{17}$ and $Fe_{83}C_{17}$ eutectic compositions. Past work [132] has demonstrated that electrostatically levitated $Fe_{83}B_{17}$ solidifies into either equilibrium *bcc*-Fe + Fe_2B or a metastable coherently intergrown $Fe_{23}B_6$ phase in a manner that appeared to be near-stochastic[146]. This observation ran counter to a body of work claiming some form of Fe_3B as the main solidification product. As a primary devitrification product from glassy Fe-B binary alloys[32], the similarity of the $Fe_{23}B_6$ structure to that of the the amorphous phase is well documented[198], and it may be expected that this similarity extends to the liquid as well.

The $Fe_{23}C_6$ structure, while also definitively metastable, is expected to have a cohesive energy very close to that of θ-Fe_3C (19.5 meV/atom and 20.6 meV/atom, respectively), and is considered by some to be more stable[49]. However, it is never observed in the binary, appearing only in the grain boundaries of materials of three or more components, and commonly stabilized by the substitution of rare earth elements and large atoms. While a variety of explanations have been proposed to explain its absence [49], it remains a mystery why it is not more common.

The number of *in-situ* structural studies during the solidification process is limited, and the possibility remains that, as often seen during solidification in the Fe-B system, the $Fe_{23}C_6$ functions as a transient metastable state. The nominal composition of the structure is close to that of the eutectic, implying the same kinetic limitations that make θ-Fe_3C more commonly observed than the equilibrium γ-Fe + graphite phase would favor the growth of $Fe_{23}C_6$ as well. However, of the 50+ containerless solidifications observed during the experiments that contributed to this work, none observed the structure. It could be that the lifetime of the phase was shorter than what was observable within the time resolution of the experimental apparatus. However, it may also be the case that the local ordering in the Fe-C liquid is less favorable to the formation of the $Fe_{23}C_6$ structure than in the Fe-B system.

We have investigated the liquid structure of both alloys using the high-energy x-ray capabilities of a synchrotron light source combined with the Beamline Electrostatic Levitation Furnace (WU-BESL)[99] and time of flight (TOF) neutron studies using the Neutron Elec-

trostatic Levitator (NESL)[100]. The x-ray scattering strength of the metalloid (M) atoms, roughly proportional to Z, is small enough relative to the larger Fe atoms that they are nearly invisible to x-rays. However, the metalloid neutron scattering lengths are much larger, and thus simultaneous measurements provide enough contrast to determine the Fe-M partial pair correlation function. By modeling the resulting diffraction patterns using reverse monte carlo techniques, we provide a qualititative comparison between local ordering in the two liquids, and relate it to the structure of common solidification products.

5.2 Experimental Methods

5.2.1 X-ray and Neutron Scattering

Arc melted ingots were prepared at the Ames Laboratory Materials Preparation Center (MPC) using iron from Toho Zinc Corp. (99.99% purity, metals basis), boron-11 from Eagle Pritcher (99.54% purity), and carbon from Alfa Aesar(99.9995% purity, metals basis), and were melted under a reducing atmosphere. The ingots were then broken into small pieces and remelted under a forming gas on polished graphite blocks to form levitation spheres. In order to confirm the samples were free of contamination from the graphite, carbon analysis was performed on the raw ingots and the processed spheres at the MPC on a Leco CS-444 Carbon Determinator. All samples were prepared from the same batch. Samples for the BESL were sized between 30 and 80 mg, while samples for the NESL were chosen to be 150 mg to 400 mg, reflecting the greater volume required for neutron scattering statistics. Samples were massed before and after processing on the graphite and in the levitation furnaces to track stochiometry shifts. Initial sample procesing was carried out in the ISU-ESL[62]. Number density ($n = N_{\mathrm{A}}/M\rho_m$, N_{A} is Avogadro's number, M is the molar mass, and ρ_m the mass density) for normalization of $G(r)$ was acquired from volumetric data obtained via the machine vision method presented in [79].

For high-energy x-ray diffraction measurements, the WU-BESL was installed at beamline 6-ID-D at the Advanced Photon Source (APS) at Argonne National Laboratory. In the BESL, upon melting, samples (∼30-70 mg) were held isothermally in the liquid for 30 s while ac-

quiring x-ray diffraction patterns with a two-dimensional GE Revolution 40RT detector. The temperature was first stepped up in increments of 50 K to a maximum of 150 K above the melt before cooling down in similar steps in order to ensure complete dissolution of any solid material present.

To obtain the normalized structure factor $S(q)$ and pair distribution function $g(r)$, x-ray data was corrected for compton scattering, flourescence, Laue diffuse scattering, polarization, geometric corrections, and normalized by the atomic scattering functions as described in Chapter 2. All analysis was performed using the Washington University X-ray Batch Analysis package[199], which contains specific corrections for the WU-BESL sample environment, such as an absorption calculation for offset spherical samples. X-ray data was obtained out to 22 Å^{-1}, and is here presented truncated to 16 Å^{-1}.

Neutron diffraction measurements were performed at the Spallation Neutron Source (SNS) at Oak Ridge National Laboratory. The NESL was installed at the SNS at BL-1B, the Nanoscale Ordered Materials Diffractometer (NOMAD). In the NESL, once molten, samples ($\sim$200 mg) were held at two temperatures, one ten degrees above the melting temperature and one 50 K higher, for 18 minutes each. Due to the low statistics obtained, these scans were compared, found to be virtually identical, and have been subsequently summed. While it is now known the sample could have been held in the liquid state for longer, during the experiment there were concerns about evaporation, both regarding stochiometry shifts of the samples themselves as well as the effect on the mirrors used for positioning, pyrometry, and the heating laser. All neutron data was corrected for absorption and secondary scattering and normalized to the neutron scattering lengths by a set of IDL scripts and python programs developed at the NOMAD beamline. The neutron data was collected out to 30 Å^{-1}. Data presented here is truncated to 16 Å^{-1}.

Additional normalization for both x-ray and neutron data was performed by the method described in Chapter 2 as implemented in a LabVIEW VI by Johnson [128, 92]. To verify that there was no significant stochiometry shift via preferential evaporative mass loss, Fe-C samples were later analyzed by the Leco CS-444 Carbon Determinator and Fe-B samples by inductively

coupled plasma mass spectrometry (ICP-MS), where any compositional shift was determined to be within the measurement error of the instruments.

5.2.2 Computational Methods

Reverse Monte-Carlo (RMC) simulations were performed using the RMC_POT program [200], chosen for its ability to easily parallelize computation. The hard-sphere cutoff distance was determined using the minimum before the first peak in $g(r)$, and verified against those used in published MD simulations [201, 58]. A move-out option, forcing atoms below the cutoff distance to separate during the move generation process, was enforced to ensure there were no correlations below the hard sphere cutoff. An optimal grid was empirically determined to consist of 7 atoms as the minimum grid size that did not dramatically increase computational time. An r-spacing of 0.02 Åwas used, based off of the original resolution of the scattering data.

All RMC fits were performed using experimental $S(q)$ from both x-ray and neutron scattering as simultaneous constraints; previous work has demonstrated that the use of the q-dependent atomic scattering functions as indirect constraints results in more physical fits than simply using the weighting factors for $g(r)$[202]. For the neutron results, the weighting factors of each partial pair correlation function (PPCF) were determined using the approximation given by Ref. [126] and were given by $c_{\text{Fe-Fe}} = 0.865$ and $c_{\text{Fe-(B,C)}} = 0.135$. The q-dependent weighting factor of each PPCF was generated using the x-Ray batch analysis package and used directly by RMC_POT. Critically, in both materials, the metalloid-metalloid PPCF was calculated to be nearly invisible in the x-ray data (normalized weighting factor of ~ 0.007) and within the noise ratio in the neutron data ($\sim .01$), and so was set to zero in both sets of RMC simulations. The statistical error on the neutron scattering data collected was notably higher than the x-ray data; as such, for the purposes of RMC simulation, the x-ray data was weighted more strongly by assigning it a lower standard deviation.

Each RMC instance was run for 10 hours or until both the χ^2 and R_p quality factors converged to a stable value. Atoms were initially allowed 0.25 Å per move; after the quality factors of the fit converged, moves of 0.5 Å were allowed to enable the ensemble to escape any local

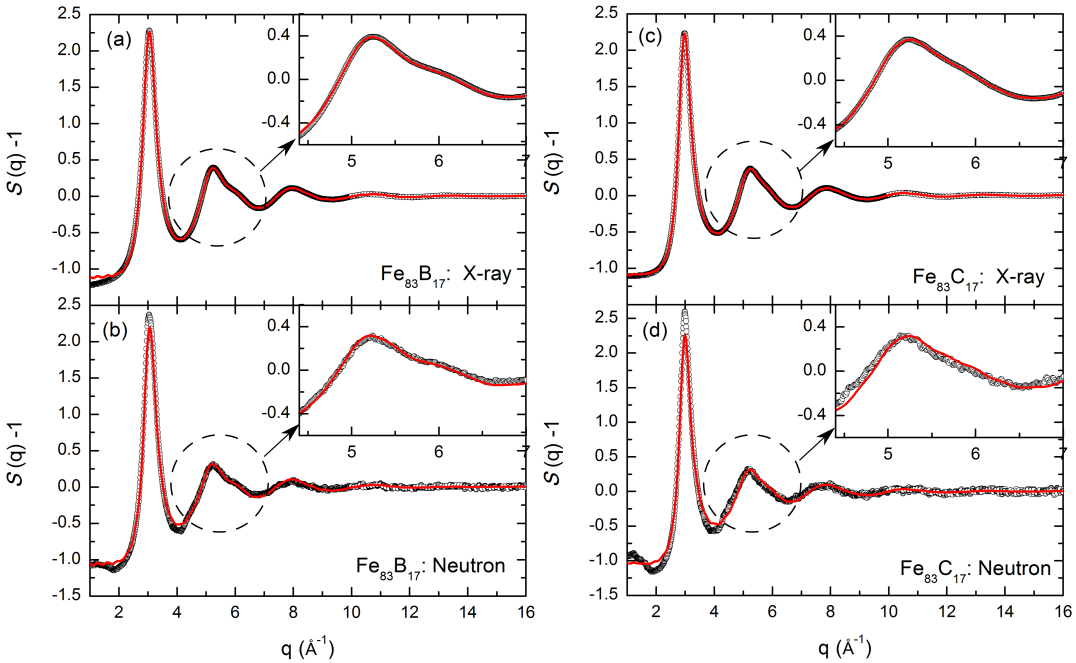

Figure 5.1: Black circles represent experimental $S(q)$ data, while red lines are the corresponding RMC fits. (a) X-ray and (b) neutron diffraction on $Fe_{83}B_{17}$ at 1470 K (c) X-ray and (d) neutron diffraction on liquid $Fe_{83}C_{17}$ at 1450 K

equilibria, before the move length was reduced back down. In addition to starting configurations generated using *fcc* and *bcc* ensembles, a series of 8 pseudo-random starting configurations of 5000 atoms each were generated using Mathematica[203]. Ten simulations were performed for each composition, one using each of the starting configurations. The simulations were individually examined to ensure no exceptional bias from the starting configuration was present. The analysis presented on each composition is an average of results from all simulations.

Voronoi analysis was accomplished using the Voro++[204] implementation in the Open Visualization Tool (OVITO)[130] as controlled by a custom python script written for this work. It can be shown that weighted bisecting planes based on atomic radii produce more physical results than traditional voronoi tesselation[205]. Polydispersive tesselation was performed by specifying Goldschmidt radii for each element as given in Ref. [206]. In order to reduce spurious nearest neighbor geometries, a minimum face size cutoff of 0.25 $Å^2$ was applied.

Honeycutt Anderson (HA) calculations were performed through a python program written by collaborators from Washington University used for previous publications [84]. All results

were verified by comparing the output with a Mathematica package written during the course of this dissertation. Both packages use a cutoff scheme to determine the bonded nature of root pairs in the system. Here, bond lengths were calculated by using the first minimum in $g(r)$ after the first peak, and in both systems were found to be ∼3.4 Å. While unbonded root pairs were also examined, results presented here are based only on the bonded root pairs, and all non-physical root pair clusters have been removed from the results. Honeycutt Anderson indices were also calculated for the crystal structures in the system. The indices are an extremely sensitive function of the bond length; for each crystal structure, the cutoff length was chosen according to the first wide minimum in the pair distribution function

All structure visualization was performed with the use of the Visualization of Electronic and Structural Analyis package (VESTA)[207].

5.3 Results

5.3.1 The Structure factor $S(q)$ and pair distribution function $g(r)$

Normalized $S(q)$ obtained 20 K above the melt temperature for each sample (1470 K for $Fe_{83}B_{17}$ and 1450 K for $Fe_{83}C_{17}$) and the results of corresponding RMC simulations are displayed in Fig. 5.1. The fit to the x-ray data is excellent in both cases ($\chi^2 \sim 1.2$). The fit to the neutron data is worse ($\chi^2 \sim 3$) but still good. While it generally follows the experimental structure, there are large deviations in the first peak in both materials. This is most likely a result of the secondary scattering curvature correction described in Chapter 2.

There are several subtle differences between the compositions visible in the structure data. Most notably, a high-q shoulder on the second peak becomes much more pronounced in Fe-B sample than the Fe-C, so much so that in the neutron $S(q)$, the high-q side of the of the second peak in the Fe-C pattern is almost flat. The coherent scattering length $< b >$ of B^{11} and C are nearly identical (6.65 and 6.646 fm, respectively)[208], allowing direct comparison of the $S(q)$ data, and so it can be assumed this difference in features is due to a difference in structural ordering. Given the increased contribution of the Fe-(B,C) PPCF in the neutron scattering results, it is likely that this shoulder is largely a result of the Fe-Fe PPCF in both

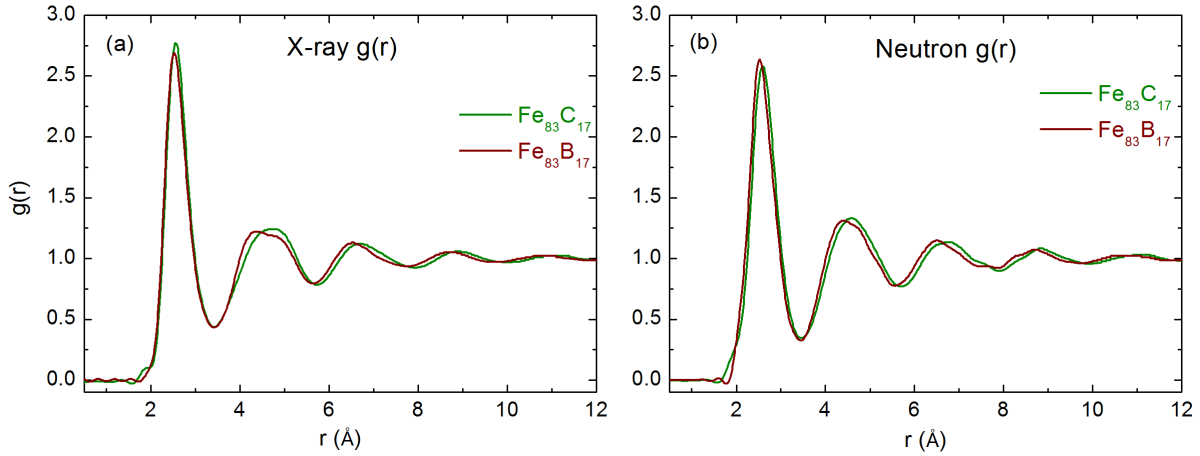

Figure 5.2: (a) Comparison of the $g(r)$ obtained for both materials by (a) x-ray scattering and (b) neutron scattering. Brown lines correspond to $Fe_{83}B_{17}$ while green represent $Fe_{83}C_{17}$

systems. Typically, this feature has been associated with a degree of icosahedral ordering in the melt[209]. In addition, there is a slight difference in the spacing of the peaks, representing a slightly increased number density in liquid $Fe_{83}B_{17}$ over $Fe_{83}C_{17}$. The coordination number was determined by integrating the first peak in the $g(r)$, and was determined to be 13.6(5) and 14.1(5) for Fe-C and Fe-B, respectively.

Figure 5.2 contains the $g(r)$ data obtained from x-ray and neutron scattering. The second peak, representing the second coordination shell, exhibits a double peak in $Fe_{83}B_{17}$ that is not present in the $Fe_{83}C_{17}$ data. This structure is replicated in published MD results [58], appearing even more strongly in pure iron [57]. By contrast this feature is not present in the $Fe_{83}C_{17}$ peaks, with the second coordination shell asymmetric and skewed towards high r. Additionally, there is a subtle feature at low r in the $Fe_{83}C_{17}$ data, just below 2 Å, that is present in increased magnitude in the neutron results, implying the contribution comes from the Fe-C PPCF. It may be tempting to dismiss this feature as a termination ripple or other artifact of the fourier transformation, but it was consistently produced while the data reduction process was refined, appearing no matter what Q_{max} or damping functions were applied. This feature has also been observed in MD simulations on the Fe-C liquid [201], corresponding to a peak in the Fe-C PPCF.

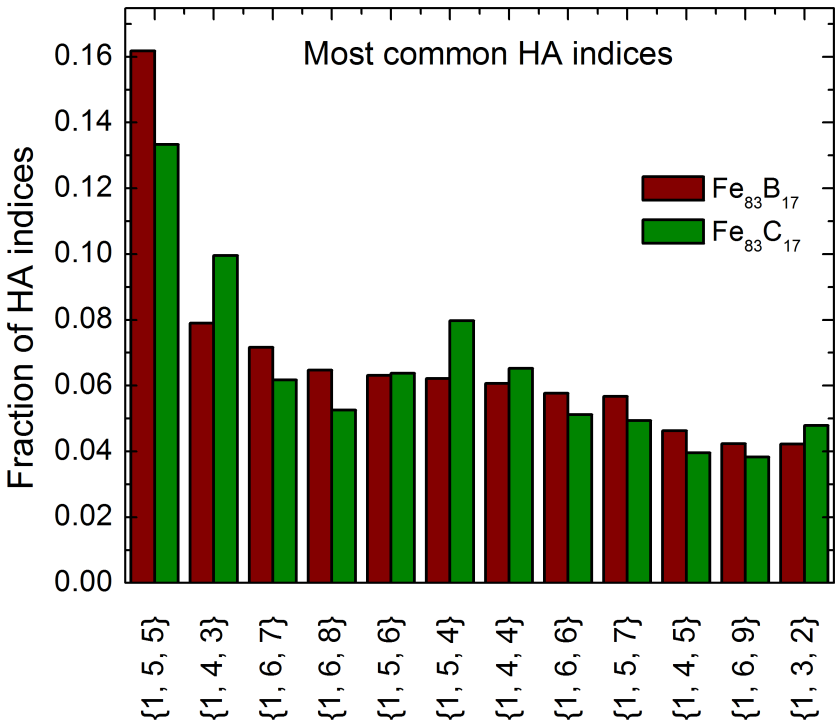

Figure 5.3: Most prevalent Honeycutt-Andersen indices among root pairs in the liquid, arranged by prevalence in the Fe-B system

5.3.2 Honeycutt-Andersen Index

The results of Honeycutt-Andersen indexing on the RMC configurations are presented in Fig. 5.3. Here we classify only the topological ordering of the system and ignore any potential differences in the local environment between the chemical species. We also focus only on bonded root pairs. The most striking result is the dominance of the (1,5,5,1) index in the Fe-B liquid. Root pairs characterized by the (1,5,5,1) index were twice as common as the the next most common root pair in the Fe-B liquid. The (1,5,5,1) index is also the most common ordering in the Fe-C liquid, but the Fe-C liquid appears to contain a larger relative fraction of distorted icosahedral environments, such as the (1,5,4) and (1,4,3) indices. These indexes represent stress-relieving disclinations from the ideal icosahedral cap. It is important to note, however, that an HA index is not representative of a complete cluster, and a complete icosahedron would require 12 of these structures associated with it.

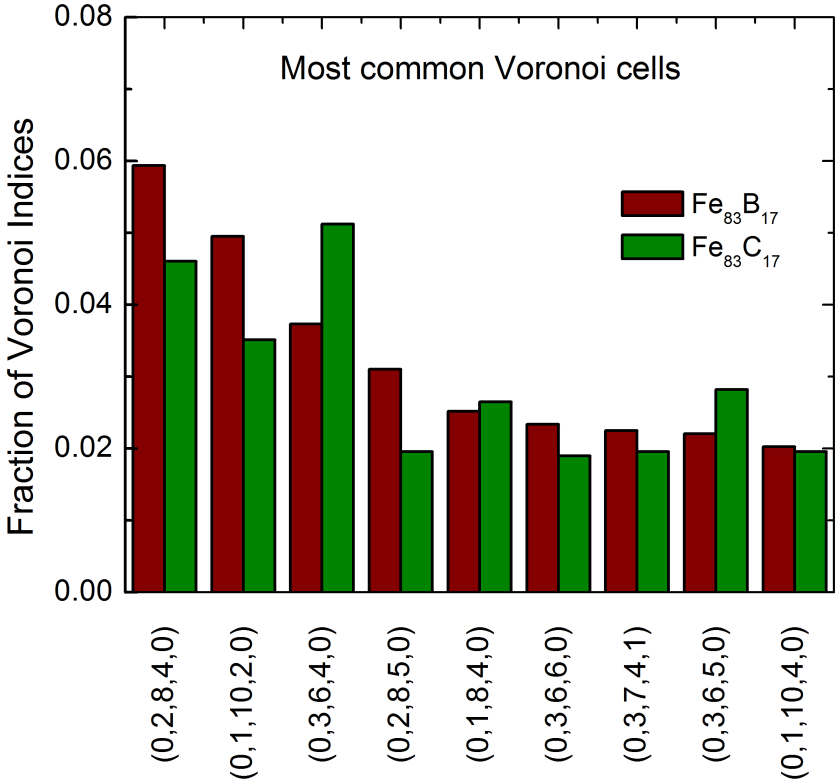

Figure 5.4: Most prevalent Voronoi indices in the liquid, arranged by prevalence in the $Fe_{83}B_{17}$ system

5.3.3 Voronoi Tesselation

Figure 5.4 charts the most common voronoi indices $(n_3, n_4, n_5, n_6, n_7)$ appearing in the system. The fraction of atoms that exhibit a local order resembling an icosahedron is largest in the $Fe_{83}B_{17}$ liquid. Notably, the system is dominated by $(0, 2, 8, 4, 0)$ type indices followed by $(0, 1, 10, 2, 0)$. This result is consistent with both RMC studies of other glass forming materials, such as $Zr_{80}Pt_{20}$ [87], and the results of previous XRD on liquid $Fe_{80}B_{20}$[58]. $(0, 2, 8, 4, 0)$ and $(0, 1, 10, 2, 0)$ structures are closely related topologically [61], representing distortions of the perfect icosahedral $(0, 0, 12, 0, 0)$ cell. Icosahedron are closely related to the glass formability of a material, causing a degree of structural frustration[210] as well as being associated with slow moving clusters in the liquid[61], and thus to see these dominate the glass-forming $Fe_{83}B_{17}$ is consistent with conventional knowledge of the structure of metallic glass forming liquids[**?**]. By contrast, the most common Fe-C liquid index comes from $(0, 3, 6, 4, 0)$ clusters, representing a distortion of ideal fcc ordering of $(0, 12, 0, 0, 0)$. This is consistent with the results of MD simulations[195]. Though the high occurrence of (0,1,10,2) was not observed in that study, those simulations demonstrated that (0,1,10,2) Fe-centered clusters exhibited particularly long lifetimes. The overall spread of indexes is fairly broad, as one would expect from a disordered liquid, with the vast majority of indexes appearing only once or twice.

5.4 Discussion

Given the features observed in the liquid structures in Fig. 5.1 and the well known glass-formability of the Fe-B system, it is reasonable to see a predominance of icosahedral ordering. More insight may be gained by comparing the ordering in the liquid to the local atomic environments in the most common structures appearing in the system.

The Fe_2B structure consists of two inequivalent atomic sites, one Fe and one B. Locally, the boron atoms are characterized by bicapped Archimedes antiprisms [211], while the Fe atoms are surrounded by rectangular pyramids. These structures correspond to voronoi indices of (0,2,8,0) and (0,0,12,3), respectively. Notably, Fe_2B is the only boride with B-B nearest neighbor pairs.

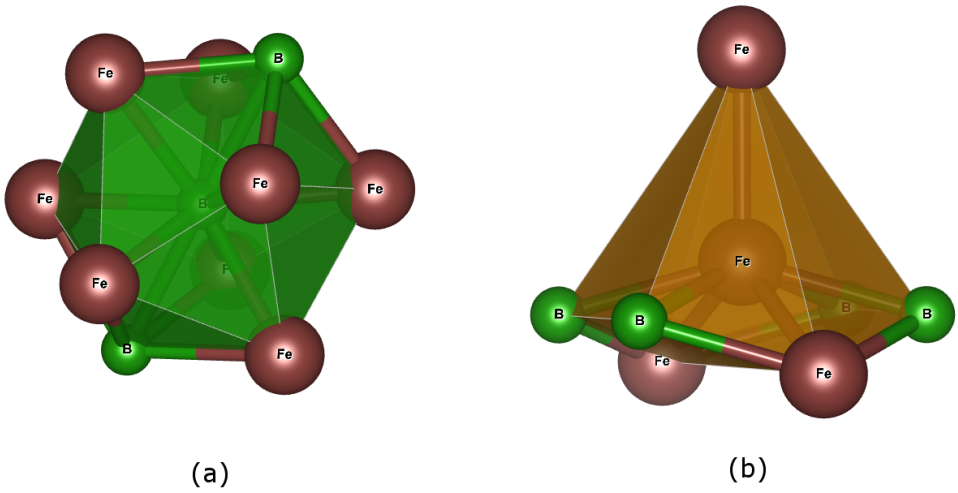

Figure 5.5: Coordination polyhedra of (a) boron atoms and (b) iron atoms in the Fe_2B structure

Ganesh et. al[144] found a B-B coordination number of 0.4 in the liquid as modeled by ab initio MD.

The $Fe_{23}B_6$ structure features five inequivalent positions. Due to the flexibility of the structure, the local atomic environments have been characterized in a number of different configurations[62, 180]. The environments in Fig. 5.6 were developed from the structure refined during the course of the work in Chapter 3. Boron atoms, occupying $24e$ sites, are characterized by a square antiprism (CN = 8). Fe atoms on the $8c$ sites are surrounded by atoms in a tetrahedral geometry $(4, 0, 0, 0)$. The Fe atoms occupying $4a$ sites, with a coordination number of 12, are characterized by a 14 sided polyhedra. The $32f$ site Fe atoms are 13 coordinated $(0, 3, 6, 4)$, and the $48h$ sites are 14 coordinated $(0, 0, 12, 2)$. These match well with the description in Ref. [180] aside from the $48h$ site Fe polyhedra. Others have reported more Frank Kasper polyhedra in the structure [62] and describe voronoi indices of $(0, 0, 12, 2)$, $(0, 3, 6, 4)$, $(0, 5, 4, 0)$, $(0, 0, 12, 4)$, and $(0, 6, 0, 12)$.

Finally, the θ-Fe_3C structure, as seen in Fig. 5.7, is characterized by 14 and 15 coordinated FK polyhedra on the Fe sites, with voronoi indices ($(0, 0, 12, 2)$ and $(0, 0, 12, 3)$, respectively,

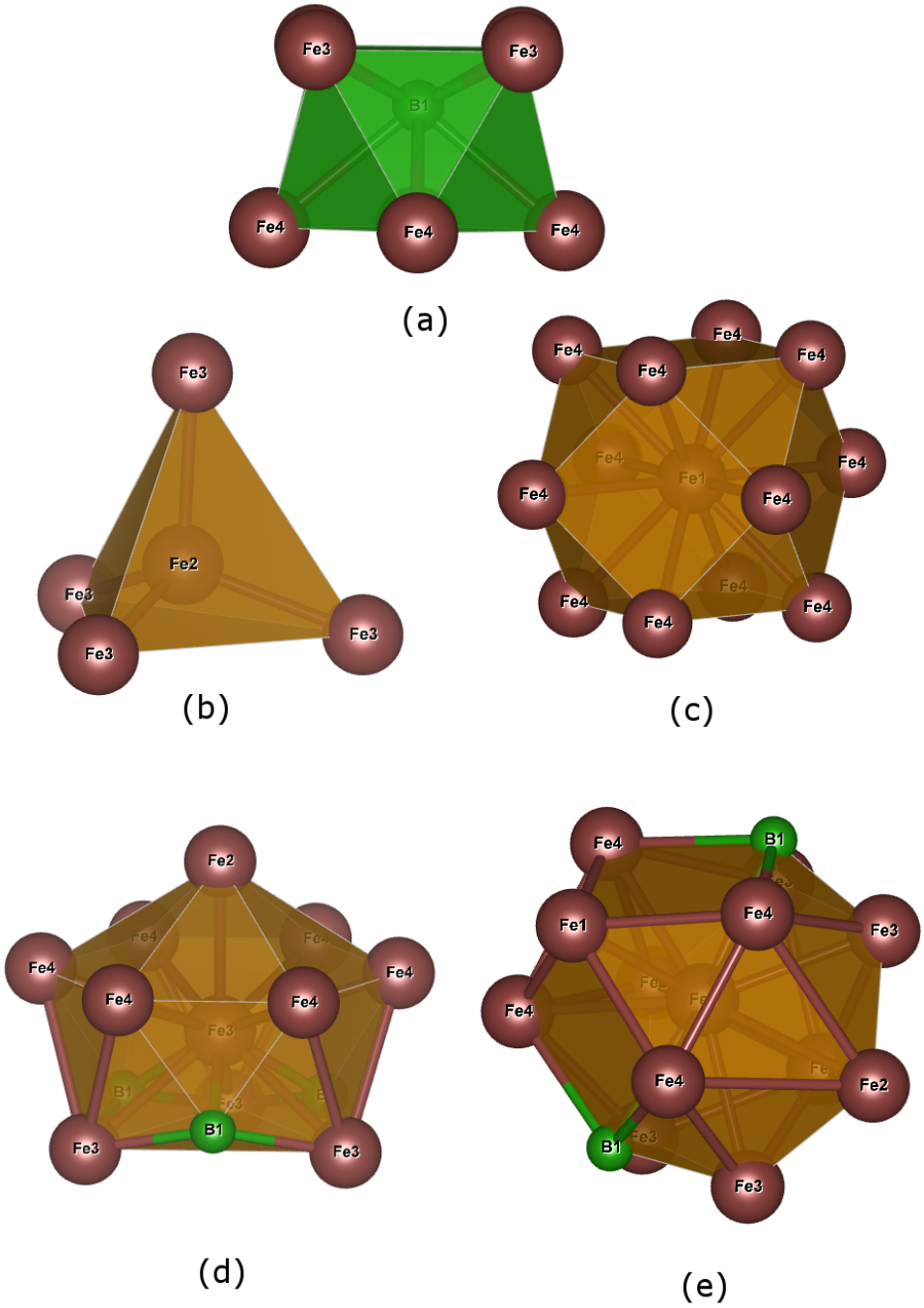

Figure 5.6: Coordination polyhedra of (a) boron atoms and (b-d) iron atoms in the $Fe_{23}B_6$ structure. (b), (c), (d), and (e) represent $8c$, $4a$, $32f$, and $48h$ sites, respectively.

Table 5.1: The voronoi indices of common structures near the Fe-B and Fe-C eutectic.

Structure	Voronoi Index	Fraction
$Fe_{23}B_6$	(0,0,12,2)	.37
	(0,3,6,4)	.28
	(0,2,8,2)	.12
	(0,3,6,1)	.12
	(0,7,6,4)	.09
θ-Fe_3C	(0,2,8,5)	.444
	(0,3,6,0)	.31
	(0,1,10,4)	.24
bct-Fe_3B	(0,3,6,0)	.25
	(0,3,6,5)	.25
	(0,3,6,7)	.25
	(0,1,10,4)	.25
Fe_2B	(0,0,12,3)	.63
	(0,2,8,0)	.36
bcc-Fe	(0,6,0,8)	1
fcc-Fe	(0,3,6,0)	1

and a trigonal prism on the C site, $< 0, 3, 6, 0 >$, which is common among many of the TM-B compounds.

The HA indices for θ-Fe_3 and the $Fe_{23}B_6$ are given in Fig. 5.8. The $Fe_{23}B_6$ structure is dominated by the $< 1, 5, 5 >$ index, mirroring the strong dominance of the pure $(1, 5, 5)$ cluster in the liquid. On the other hand, the θ-Fe_3C structure appears to be composed equally of disclinated $< 1, 5, 4 >$ indices. This mirrors the relative increase in disclinated icosahedral clusters in the Fe-C liquid. While our Voronoi tesselation on the Fe-C liquid does not reveal a large number of (0,3,6,0) polyhedra, MD simulations have suggested that these are the dominant local environments of the carbon atoms in the liquid[195], matching very well with the local environment of the C sites in θ-Fe_3C.

This similarity may form the basis for a kinetic argument as to the nature of phase selection in undercooled $Fe_{83}B_{17}$. Previously, we observed that the $Fe_{23}B_6$ structure frequently nucleated prior to the formation of the equilibrium Fe_2B. We were unable to determine a structural difference that may have led to the structure transforming versus persisting through cooling, and simply ascribed it to the metastable nature of the phase. However, the formation of a transient metastable phase that serves to reduce the nucleation barrier to the formation of

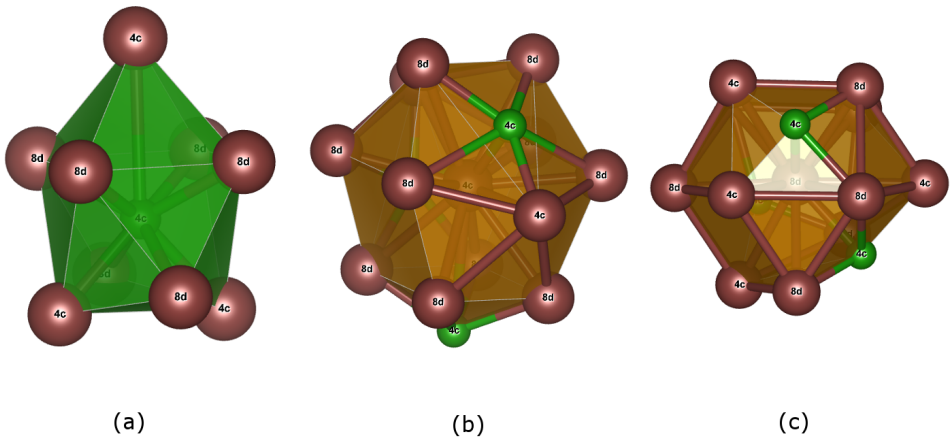

Figure 5.7: Coordination polyhedra of (a) 4*c* carbon atoms, (b) 4*c* iron atoms and (c) 8*d* iron atoms in the θ-Fe_3C structure.

the equilibrium structure has recently been observed in $Ni_{50}Zr_{50}$[96]. Given the compositions of $Fe_{23}B_6$ and Fe_2B (80.3% Fe (nominal) and 66.6% Fe, respectively) compared to the liquid, coupled with a reportedly large variability in composition of $Fe_{23}B_6$[180, 48], one may expect kinetic limitations would favor the formation of the $Fe_{23}B_6$ structure over Fe_2B in a similar manner. Indeed, once samples have been processed several times in the ESL, they tend to form the $Fe_{23}B_6$ phase far more frequently, raising the question of whether or not it forms every time as a transient metastable phase. Unfortunately, the limitations of our experimental resolution, both spatially and with regards to acquisition time, prevented us from being able to state definitively whether or not $Fe_{23}B_6$ always formed before the equilibrium structure. Similarly, if the $Fe_{23}C_6$ phase ever nucleated in the Fe-C liquid, it could happen on a timescale far too quick to observe using the BESL environment.

It is very important to recognize the limitations of this study. The original plan for the neutron scattering experiment had been to include isotopically substituted samples, using the contrasting Fe scattering lengths to establish a constraint on the third PPCF (metalloid-metalloid). The samples proved to be too dirty to process in the NESL. While approximating the PPCF from the M-M pairs as zero is mathematically sound as related to the scattering lengths and atomic form factors, it means that the RMC modelling is blind to any structure from B-B pairs or C-C pairs. Fortunately, previous MD work and liquid structure studies have suggested

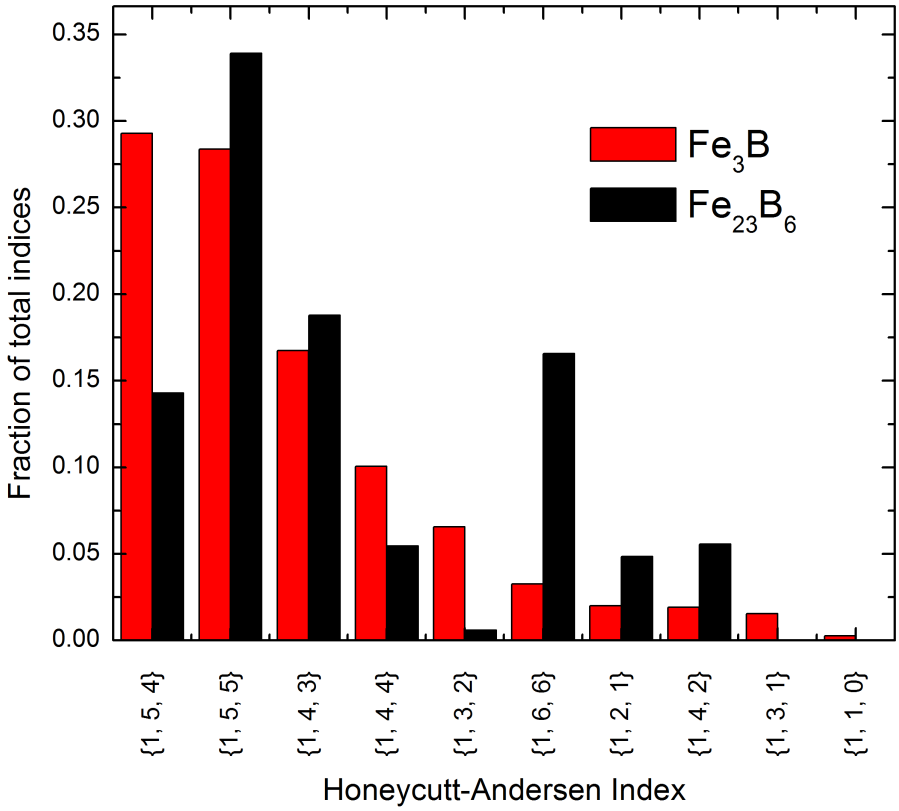

Figure 5.8: Most common HA indices in $Fe_{23}B_6$ (black) θ-Fe_3C (red) as fraction of total root pairs

that the metalloid-metalloid coordination number is either zero or very low[195]. However, as a result, we have shied away from identifying Voronoi polyhedra related to specific atomic species.

MD simulations have suggested that the distinctive high-Q shoulder on the second peak is largely a result of vertex and face sharing of boron-centered tri-capped trigonal prisms[145]. Likewise, MD work on the Fe-C liquids suggest that the most common Voronoi polyhedra are (0,4,4,0) and (0,3,6,0) coming from carbon atoms[195]. In both systems, it is likely that the local chemical order associated with the metalloid atoms plays a critical role in the different behavior of the liquid. The next step in this work, then, should be to add another constraint to allow proper modeling of the B-B PPCF.

However, what is presented here is a promising foundation for future work. The detectors at NOMAD have been heavily optimized in the year since this data was obtained, and any future scattering studies would likely gain a statistical advantage. There is now a better understanding of the stochiometry shift associated with long processing holds in the liquid state, as well as the tolerance of the NESL itself with regard to evaporation. It is possible that with the increasing robustness of the NESL system, even samples with large impurity populations, such as the isotopically substituted samples attempted in this investigation, may be processable. Alternatively, a number of successes in liquid structure modeling have come from constraining RMC ensembles with PPCFs generated from MD simulations. If these could be obtained, the chemical ordering in the liquid may resolve the unanswered questions in these systems.

It has been established that by generating a large body of statistics through repeated RMC simulations, even a partially constrained simulation such as the one presented here may offer insight into the topological order in the liquid[128]. Due to the incomplete constraint of the simulations performed here, this study has deliberately avoided insinuating any insight beyond general topological structure into the chemical ordering, and focused on general topological features of the liquid. From this perspective, we have determined a qualitatively stronger similarity between the Fe-B liquid and the $Fe_{23}B_6$ structure than in the Fe-C liquid, and noted similarities between the local environments in the θ-Fe_3C structure and the Fe-C liquid. In particular, the dominance of the pure icosahedral ordering in the Fe-B liquid reflects a similar

ordering in the $Fe_{23}B_6$ structure far more than in the Fe-C liquid. While this is far from a quantitative explanation regarding the absence of the $Fe_{23}C_6$ structure in the binary, this suggests an alternative line of inquiry that has not previously been considered, and show that there may be some basis for further exploration.

CHAPTER 6. CONCLUSIONS AND OUTLOOK

Through Chapters 3, 4, and 5, we have successfully demonstrated the use of ESL systems in versatile and multi-faceted approaches to characterize one particular system, and have produced novel results of wide interest. The coherent intergrowth stabilizing $Fe_{23}B_6$ and *fcc*-Fe to low temperatures is a new effect not noticed despite decades of intense research into this material, including solidification work using containerless processing. The magnetic properties of this enhanced phase have not been observed before, and applying the first use of the TDO to map out high temperature magnetic phase diagrams of the metastable phases in the system has shown that this intergrown structure has a new, previously unobserved, high T_C. The application to scattering environments, including some of the first data obtained with the NESL at the SNS, provides a comparison of two liquid systems that has not been done before, may answer a question of some considerable interest in the solidification of eutectic Fe-C, and at the very least provides the highest quality liquid structure on both eutectic Fe-B and Fe-C to date.

This work has demonstrated the varied capabilities of levitation environments in regards to the study of solidification, metastable phases, and undercooled liquids. During the course of this dissertation, the capabilities of the ISU-ESL have advanced to the point of experimental reliability, and analysis programs and protocols have been developed to understand the output of the system. Multiple scattering ESL environments have also been fully tested at the APS and the SNS, and the capabilities of these instruments are now better understood.

As with any good scientific investigation, however, more new questions have been raised than have been answered. There is still much work to do. The low temperature presence of metastable *fcc*-Fe needs clarification, whether through electron microscopy or still higher resolution x-ray work. The precise magnetic ordering of the $Fe_{23}B_6$+*fcc*-Fe phase is an open

question. With the NESL soon undergoing a series of planned upgrades for operational robustness, ease of deployment, and hardiness against evaporative materials, it may be possible to perform neutron scattering that clarifies this question. By performing a series of anneals above and below the magnetic transition temperature, it may be possible to observe a difference in peak intensity due magnetic scattering. Modifications to the detector banks at NOMAD have already fixed some of the statistical issues present in the work in Chapter 5. This may also allow neutron data to be taken on isotopically substituted samples as originally planned, adding a third constraint to allow full modeling of the liquid structures. MD results could be performed as well, and has been shown in the past, constraining the results of RMC simulations with MD partials enables an easy, repeatable, and accurate probe into the local ordering of the liquid.

A number of studies could spring from the science demonstrated here. For one, a thorough characterization of the off-eutectic solidification of Fe-rich Fe-B alloys may provide an easier look at retained fcc-Fe. Similar systems that form the $(TM)_{23}M_6$ structure could also be investigated, to see if this metastable intergrowth is attainable elsewhere, preferably focusing on materials where the $(TM)_{23}M_6$ structure has a lattice parameter large enough that stabilized fcc-Fe would be close to the high-spin regime. Such a system may provide an alternate venue for the exploration of potential ferromagnetism in metastable fcc-Fe, and the different lattice parameters associated with the different $(TM)_{23}M_6$ structures could also allow a tuning of the fcc-Fe lattice parameter. At one point, a thorough electron microscopy investigation of the metastably solidified Fe-B samples was planned to explore whether fcc-Fe was still present at room temperature and to determine the precise nature of the coherency with the $Fe_{23}B_6$ structure, and time constraints have so far held this work up. The pieces are all in place for the work to be performed at the Sensitive Instrument Facility.

To take advantage of the capabilities developed during the last several years, new projects in the laboratory should veer towards unexplored territory, using the hardware that has been established and now characterized. One significant project springs to mind. When the TDO was first implemented in the ISU-ESL, early experiments were performed on the $Co_{80}Pd_{20}$ alloy in order to test claims of ferromagnetic ordering in the deeply undercooled liquid. Those studies were largely unsuccessful due to sample impurity issues leading to heterogenous nu-

cleation, prohibiting deep undercooling. Much of the work of Rustan was on sample purity issues, and the laboratory now has a more advanced understanding of the techniques useful to produce clean samples. In addition, collaborators at the SNS have, or will have, access to multiple aerodynamic levitation environments, which could be used with a variety of reducing atmospheres to help purify samples.

Beyond that, however, the concept of magnetic ordering in liquids has not been well explored outside of the $Co_{80}Pd_{20}$ alloy, and the deep undercooling required to observe the effects there are prohibitive to many probes. Other materials should be explored, such as the (Co,Fe)-RE eutectic systems. Further, all investigations to date searching for magnetic ordering in liquids have focused exclusively on materials with a crystal structure with high T_C. Few candidates have been found with a T_C within the undercooling limit.

The search should broaden to include two other parameters. For one, part of the success of the $Co_{80}Pd_{20}$ studies was attributed to the uncommonly small volume expansion on melting, limiting the impact of any changes to the exchange energies among Co atoms and causing the projected liquid T_C to only lower by 20 K. Tetrahedrally coordinated liquids, such as silicon or germanium, experience a large volume contraction on melting, and alloying with ferromagnetic elements may provide the reverse effect on T_C. Further, the advent of ferromagnetic glasses and amorphous alloys suggests a new way at looking at the potential development of magnetism in a liquid, as the topological structure of a liquid will be much more similar to the glassy phase than to many common crystalline phases. Indeed, some compositions, such as those in the Co-Y system, have exhibited a uniformly higher T_C in the amorphous phase than in the crystalline phase. As a second search criteria, it would be wise to begin investigation on similar materials. If such a material could be found that requires less of a dramatic undercooling effect than in the CoPd system, it is possible that either the new NESL system or another levitation facility integrated into the SNS may be able to probe magnetic excitations in the liquid.

APPENDIX. SYNERGISTIC STABILIZATION OF METASTABLE $FE_{23}B_6$ AND γ-FE IN UNDERCOOLED $FE_{83}B_{17}$

Fe-B alloys are well known glass formers. When rapidly cooled at rates on the order of 10^6 K/s, alloys with B concentrations ranging from 12 - 28% can be quenched into a glassy state, with the eutectic composition (approximately $Fe_{83}B_{17}$) requiring the lowest cooling rate.[212] Much of the work in recent years has focused on the development of multi-component systems based on the Fe-B binary particularly with respect to their glass forming ability and engineering properties such as hardness,[136] corrosion resistance,[135] and soft ferromagnetism.[137, 138] According to the equilibrium phase diagram,[213] Fe-B alloys with Fe contents $\geq$ 66.7 at.% form two-phase mixtures of Fe_2B and Fe. However, when Fe-B and related alloys are quenched into a glassy state and undergo crystallization during subsequent annealing processes, it has been found that a wide variety of metastable intermetallic compounds can form that may play an important role in the production of industrially relevant materials such as permanent magnets.[32] The three most commonly observed metastable phases are body-centered tetragonal (bct) Fe_3B, orthorhombic (o) Fe_3B, and face-centered cubic (fcc) $Fe_{23}B_6$.

It is well known that the formation of metastable phases during the solidification of undercooled liquids can profoundly affect crystallization pathways and products.[65] The interactions among the high-temperature products of solidification can also play an important role in either enhancing or suppressing the transformation from metastable to equilibrium phases. By suppressing heterogeneous nucleation using a variety of techniques, several groups[44, 141, 45] have shown that non-equilibrium solidification of the undercooled $Fe_{83}B_{17}$ liquid can lead to the formation of metastable Fe_3B in the hypercooling regime (ΔT $\sim 386K$)[141] or $Fe_{23}B_6$ for more modest undercooling.[45] In the latter case, the transformation of the metastable $Fe_{23}B_6$ phase to the equilibrium Fe_2B can be suppressed for cooling rates greater than 30 K/s, but the

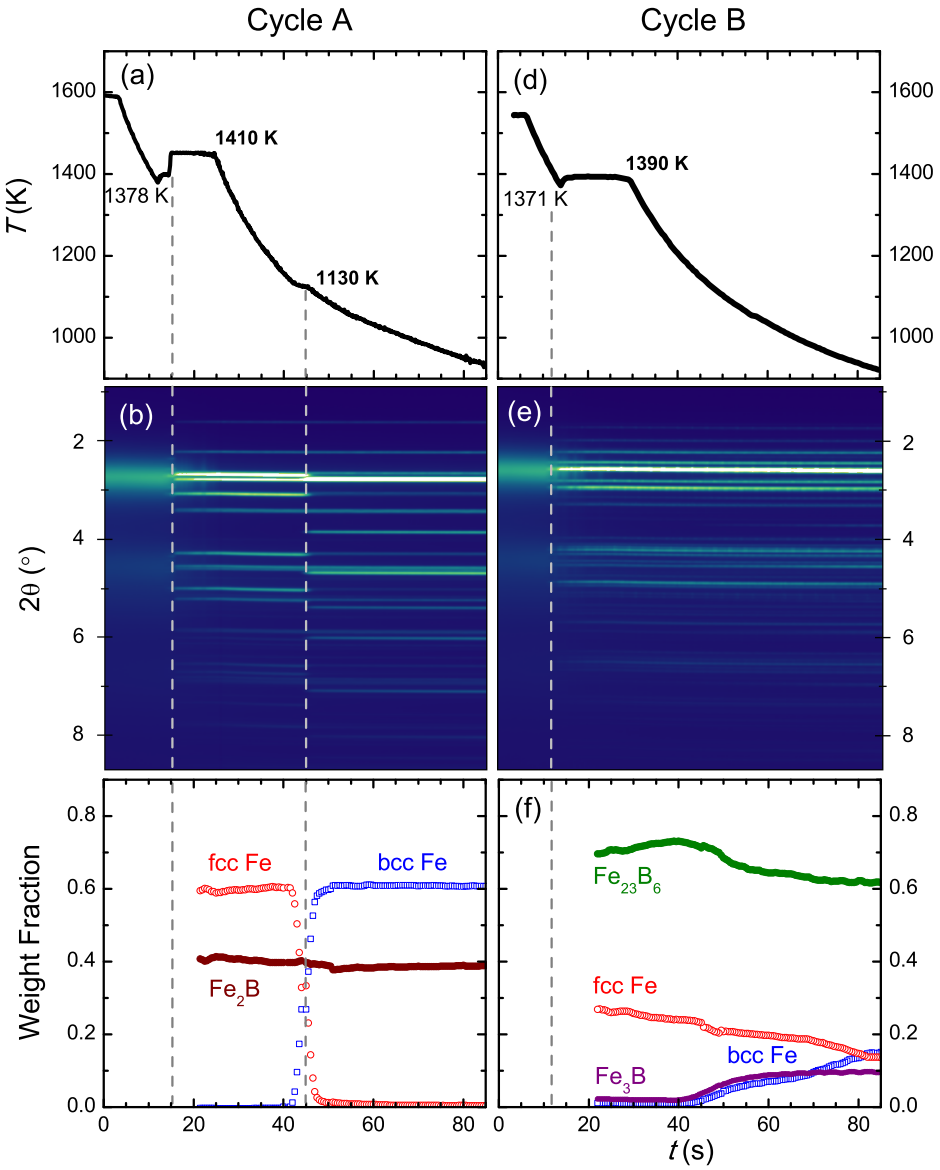

Figure A.1: (color online) Time-resolved high-energy x-ray diffraction measurements of $Fe_{83}B_{17}$. Cycles A and B denote two of the seventeen melting/cooling sequences on one of several samples in this study. The x-ray data were obtained at a rate of 2 fps. Panels (a) - (c) and (d) - (f) show the measured temperature of the sample, the corresponding x-ray diffraction pattern with the intensity color-coded and the weight fractions of the crystallization products determined from Rietveld refinements of the x-ray data for Cycles A and B, respectively. For both Cycles the total proportions of Fe and B, calculated from the composition and weight fractions of the constituent phases, remained constant within our experimental uncertainty of 1 -2 %, demonstrating the constant composition of the sample over the course of the measurement.

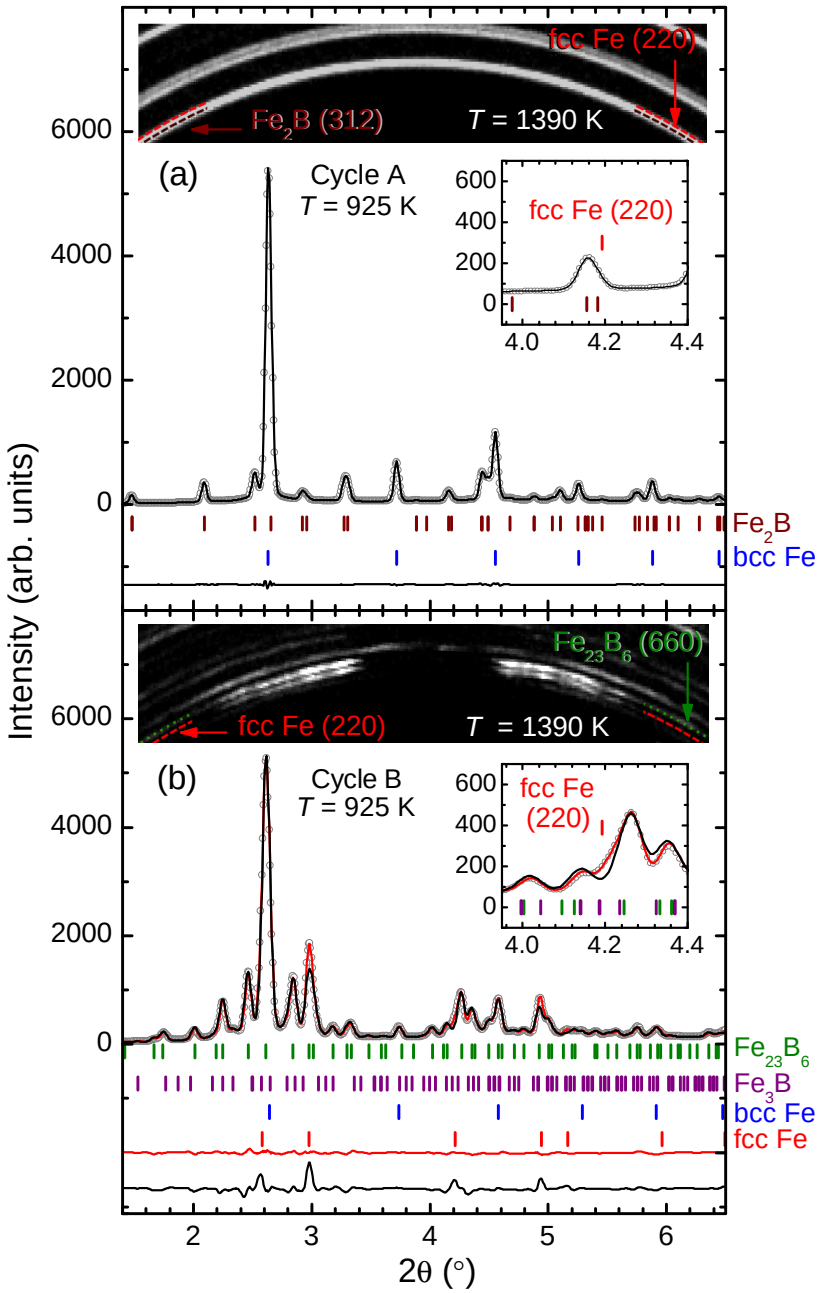

Figure A.2: (color online) Rietveld refinements of the x-ray data from (a) Cycle A and (b) Cycle B at $T = 925$ K, well below the allotropic fcc γ-Fe to bcc α-Fe transition. The hash marks correspond to the expected peak positions for the constituent phases. The lines through the data represent the fits from the refinement and the lines below the hash marks represent the residuals from these fits. No additional unindexed diffraction peaks, within the limits of detection were observed. For panel (a) $R_p = 0.027$. In panel (b) the fits and residuals including all four phases in the fit (red lines) ($R_p = 0.038$) or excluding γ-Fe (black lines) ($R_p = 0.073$) demonstrate a significant improvement in the fit including γ-Fe. The top insets to both panels show portions of the Debye-Scherrer rings recorded at $T = 1390$ K illustrating a smooth continuous nature for Cycle A [panel (a)] and the larger grain structure for Cycle B [panel (b)] in the grayscale encoded intensity. The smaller insets to each panel display an expanded view of the region close to the γ-Fe (220) Bragg peak illustrating the quality of the refinement.

mechanism underlying this suppression has not yet been identified. In particular, the role of the second solidification product, Fe, and its potential interaction with the Fe-B phase(s) have not been studied in any detail, motivating the present study using time-resolved high-energy x-ray diffraction and volume expansion studies of electrostatically levitated samples of Fe-B at the Fe-rich eutectic composition.

The $Fe_{83}B_{17}$ samples were prepared by arc melting appropriate quantities of high purity starting materials (99.99% pure Fe, 99.9999% pure B) and remelted several times to ensure a homogeneous composition throughout the volume. The alloy button was drop cast into rods that were cut into pieces with masses ranging from 25 - 75 mg. To form spheres for levitation these pieces were laser melted on a copper substrate within the Iowa State University electrostatic levitation furnace (ISU-ESL).[93] Measurements of the volume thermal expansion of levitated samples were also performed in the ISU-ESL using the machine vision video volume method described in detail previously.[79]

High energy x-ray diffraction measurements were performed at beamline 6-ID-D of the Advanced Photon Source ($E = 132$ keV; $\lambda = 0.0939$ Å) employing an incident beam cross-section of 0.2 x 0.2 mm. The samples were electrostatically levitated in the Washington University Beamline Electrostatic Levitator, a full description of which can be found in Ref. [99]. Once molten, samples were overheated 150 to 200 K above the apparent melting temperature and held for 20 to 30 seconds to ensure the samples were fully molten and to facilitate the dissolution of any oxide or impurity phases that may have been present. The laser was then shut off and the samples radiatively cooled to a temperature below the measurement range of the pyrometer (approximately 900 K). This cycle was repeated multiple times for each sample.

X-ray powder diffraction patterns were collected using a two dimensional Ge Revolution 41-RT flat panel detector. The range of scattering angles accessible was $0.9° \leq 2\theta \leq 19.5°$, allowing measurements over a range of momentum transfers of $1\ \text{Å}^{-1} \leq Q \leq 22.6\ \text{Å}^{-1}$. The acquisition speed of the data presented here was 2 fps. The sample-to-detector distance, detector tilt/rotation and flat-field corrections were refined using powder data taken on levitated spheres of Si powder mixed with epoxy, and the x-ray frames were azimuthally integrated to produce x-ray powder profiles, all using Fit2D.[120] The levitated samples spin about a vertical axis as

a result of the radiation pressure from the laser heating, providing some degree of averaging over grains in the recrystallized material. Nevertheless, the raw x-ray data from some solidified samples did exhibit texturing resulting in peak intensity fluctuations from frame to frame. For Rietveld refinements, a moving boxcar average over seven frames was applied to damp these intensity fluctuations. The refinements were performed on the x-ray data over the measured temperature range using the sequential refinement capabilities included in GSAS.[175] Peak profiles were modeled with a pseudo-Voigt function, and the half widths were allowed to vary. For all data sets, the lattice parameters, atomic positions, and isotropic thermal parameters of the Fe atoms were allowed to vary but, since the scattering of x-rays by B is relatively small, the positions and thermal parameters for B were fixed.

Figure A.1 summarizes key results of our high-energy x-ray study. In agreement with the previous study, the metastable $Fe_{23}B_6$ phase is the first binary product observed during solidification of the undercooled liquid.[45] The sample then either undergoes a second recalescence into the equilibrium Fe_2B phase (Cycle A), or the metastable $Fe_{23}B_6$ phase persists down to the lowest temperatures measured in the x-ray experiments ($\sim$ 900 K) (Cycle B). For similar undercoolings ΔT $\sim$ 75 K below the melting plateau of the equilibrium Fe_2B phase, we find no clear correlation between cooling rate and the preservation of $Fe_{23}B_6$ down to low temperature. Furthermore, thermometric measurements on a number of samples using the ISU-ESL found no clear correlations among thermal history and heating/cooling rates that indicate whether any given processing protocol will result in the solidification of the equilibrium Fe_2B + Fe or the metastable $Fe_{23}B_6$ + Fe phases for initial cooling rates on the order of 30 - 50 K/s; sequential heating/cooling cycles on any given sample result in either set of crystallization products in a seemingly stochastic fashion.

As illustrated in Fig. A.1, there are several clear and interesting differences between Cycles A and B. For Cycle A a double recalescence is observed: the first associated with the solidification of the metastable $Fe_{23}B_6$ + γ-Fe at approximately 1390 K, and a second recalescence to the equilibrium Fe_2B binary phase at 1410 K. For Cycle B, only the plateau associated with the solidification of $Fe_{23}B_6$ + γ-Fe is observed. Whereas the cooling curve of Fig. A.1(a) for Cycle A evidences a distinct feature at the allotropic fcc to bcc transition for Fe at approximately

1130 K on cooling, no clear feature is observed in Fig. A.1(d) for Cycle B. This is consistent with the presence of a sharp fcc to bcc transition in the diffraction data of Fig. A.1(b) and its absence in Fig. A.1(e). The weight fractions of the crystalline components in Fig. A.1(f), taken from a full series of Rietveld refinements of the x-ray data, demonstrate the persistence of fcc γ-Fe and the metastable $Fe_{23}B_6$ phase down to at least 900 K. In addition, below the nominal temperature of the γ-Fe to α-Fe transition, we find additional Bragg diffraction peaks corresponding to α-Fe and a not often seen, but previously identified, primitive tetragonal form of metastable Fe_3B.[**?** 214] The weight fractions of these phases increase gradually as those for $Fe_{23}B_6$ and γ-Fe decrease. We note that previous studies of the crystallization of glassy $Fe_{80}B_{20}$ have observed an orientational relationship between the primitive tetragonal Fe_3B and bcc α-Fe phases, and proposed that the presence of α-Fe may be a prerequisite for the formation of Fe_3B.[214] This is consistent with our observation of the simultaneous appearance of these two phases and concomitant growth.

A detailed analysis of both the raw diffraction data and Rietveld refinements in Fig. A.2 provides support for the interpretation above and additional evidence concerning the mechanism responsible for the persistence of the $Fe_{23}B_6 + \gamma$-Fe phase mixture to lower temperature in Cycle B. In Fig. A.2(a) the refinement of x-ray data from Cycle A at $T = 925$ K, well below the nominal fcc to bcc transition for Fe, shows only the presence of Fe_2B and α-Fe. Figure A.2(b) displays the diffraction data and refinement at the same temperature for Cycle B. Keeping in mind that the refinement shown in this panel is for data taken well below the fcc to bcc transition, Fig. A.2(b) manifests a much more complex mixture of phases including $Fe_{23}B_6$, γ-Fe, α-Fe and primitive tetragonal Fe_3B.[**?** 214] All of these phases, with the weight fractions given in Fig. A.1(f), were required for a reasonable fit of the diffraction data for temperatures below approximately 1150 K. This point is reinforced by the small insets to both panels in Fig. A.2 which focus on the region close to the γ-Fe (220) Bragg diffraction peak. For Cycle A, only peaks from Fe_2B are in evidence whereas, for Cycle B, the fit is qualitatively improved when all phases are included. The presence of γ-Fe is difficult to discern because of the nearly complete overlap of the γ-Fe diffraction peaks with those from $Fe_{23}B_6$ since the lattice parameter of fcc

$Fe_{23}B_6$ [10.70(1) Å at $T = 906$ K] is almost precisely three times that of γ-Fe [3.61(1) Å at $T = 906$ K].

The diffraction data also provide strong evidence for the coherent growth of γ-Fe and $Fe_{23}B_6$, which provides a mechanism for the persistence of these phases to low temperature. The uniformity of the Debye-Scherrer rings in the top inset of Fig. A.2(a) indicates that the grains of both Fe_2B and γ-Fe are quite small and randomly oriented at high temperature. However, in the top inset to Fig. A.2(b) we see gaps forming in the Debye-Scherrer rings and discrete reflections are observed, indicating that the grains of both $Fe_{23}B_6$ and γ-Fe are larger. Most importantly, the coincidence of the structure in the rings for both γ-Fe and $Fe_{23}B_6$ are indicative of a coherent orientational relationship between these two phases, as would occur for intergrowth or epitaxial growth. It has already been established that coherently oriented fcc γ-Fe precipitates can be stabilized to low temperature in a Cu matrix[161–163], in Cu-Au alloys,[183] or via epitaxial growth on Cu surfaces.[182] From our refinements we find that the longitudinal widths of the γ-Fe diffraction peaks are resolution limited, corresponding to a mimimum grain size on the order of a few tens of nanometers, similar to the grain sizes of γ-Fe precipitates in supersaturated Cu-Fe solid solutions.[161, 162] However, the strong texturing we observed suggests that the size of the coherently grown grains is likely much larger.

The stabilization of γ-Fe via coherent growth with $Fe_{23}B_6$ is particularly interesting in light of the many experimental and theoretical investigations of magnetism in fcc Fe over the past five decades. The nature of the magnetic ground state remains a matter of some debate although there is agreement that the paramagnetic and low-spin/high-spin antiferromagnetic/ferromagnetic ground states are all sensitive functions of the fcc lattice parameter.[215, 216, 165, 185, 217] Coherent precipitates of γ-Fe in a Cu matrix order antiferromagnetically with a small moment ($< 0.5\mu_B$/Fe) at a Néel temperatures of less than 70 K.[184, 218] On the other hand, ferromagnetic order at ambient temperature for Fe in a high-spin state was proposed for coherent precipitates of γ-Fe in Cu-Au alloys, with an expanded lattice parameter, via Mössbauer spectroscopy.[183] According to some theoretical calculations[165, 185, 217] our measured lattice parameter for γ-Fe [3.61(1) $\mathring{A}$ at T $=$ 906 K] lies close to the boundary between the proposed antiferromagnetic and ferromagnetic ground states. Neutron diffraction

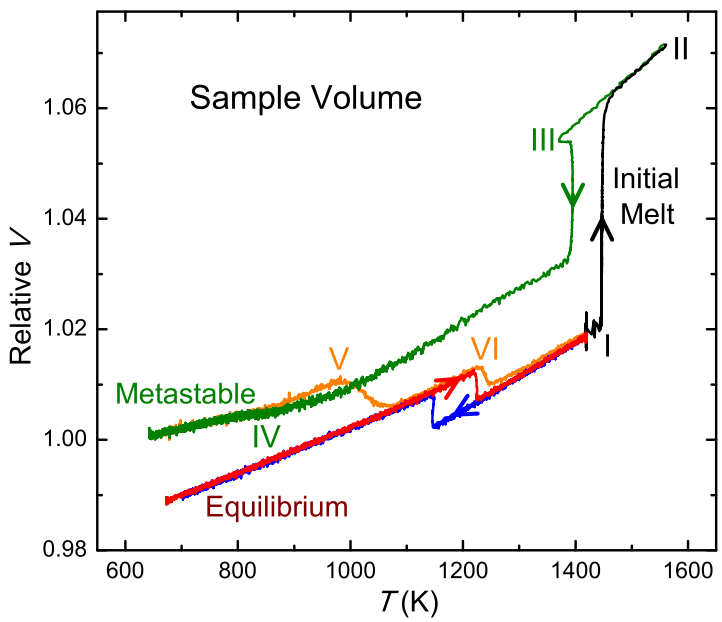

Figure A.3: (color online) Volume thermal expansion measurements of $Fe_{83}B_{17}$. The volumes are normalized to the lowest temperature measured on cooling from the liquid. The data acquisition began at (I), with the sample in the equilibrium Fe_2B + γ-Fe solid phases at a temperature of 1420 K. The heating laser power was increased in a single step (black curve) such that the sample melted and was heated to a maximum temperature of 1565 K (II). The heating laser was turned off and the sample underwent free radiative cooling (green curve). At (III) the liquid reached its minimum temperature of 1368 K, corresponding to an undercooling below the Fe_2B melt plateau of $\Delta T \sim 79K$, and underwent recalescence and solidification into the metastable $Fe_{23}B_6$ + γ-Fe phases. A gradual positive deviation (IV) from linear behavior occurred as the sample temperature decreases down to 640 K. After a two minute hold at this temperature, the sample temperature was increased at a constant rate of 3 K/s to 1420 K (orange curve). The cooling and heating curves begin to diverge at (IV) with a step in the volume at (V). After heating to 1420 K, the temperature was decreased to 670 K (blue curve) and increased to 1420 K (red curve) at a rate of 3 K/s. The cooling and heating curves are featureless beyond the expected first-order allotropic phase transition for Fe (VI).

measurements are planned to resolve the question of magnetic ordering in the metastable γ-Fe phase present in our samples.

Measurements of the volume thermal expansion of $Fe_{83}B_{17}$ using the ISU-ESL confirm that the metastable solid phases persist down to at least 640 K. The data from a representative run are shown in Fig. A.3. Upon cooling from the melt (green curve) no distinct signature in the volume thermal expansion is observed through the region of the Fe allotropic transition, in agreement with the x-ray results described above. Rather, we see a gradual positive deviation (IV) from linear behavior as the sample temperature decreases. The curvature may result from

the evolution of the phases described above, or from magnetoelastic effects due to the onset of ferromagnetism in this temperature range. Upon reheating (orange curve) we attribute the clear step at (V) to the transformation of the $Fe_{23}B_6$ metastable phase and remaining γ-Fe fraction to the equilibrium Fe_2B + α-Fe phases. This is consistent with the relatively sharp transition from α-Fe to γ-Fe now observed at (VI) on warming. After this point both the cooling (blue) and heating (red) curves are featureless beyond the expected allotropic phase transition for Fe found at 1147 K on cooling and 1224 K on heating due to hysteresis in the first-order transition. The average value of the transition temperature is 1186 K, in good agreement with the value indicated in the equilibrium phase diagram.[213]

Based on the time-resolved high-energy x-ray diffraction data and volume thermal expansion measurements we propose the following scenario for the evolution of crystalline phases in undercooled $Fe_{83}B_{17}$. First we note that, if during the initial solidification of the liquid a second recalescence to the equilibrium Fe_2B + γ-Fe phases occurs, the allotropic fcc to bcc transition for Fe is well-defined and complete. However, in the absence of a second recalescence event in the melt plateau, sizeable coherently grown grains of $Fe_{23}B_6$ and γ-Fe are found that appear to stabilize both metastable phases well below the allotropic fcc to bcc transition for Fe. With further decreasing temperature we see a gradual increase in the weight fraction of α-Fe, a corresponding decrease in the weight fraction of γ-Fe, and the slow conversion of $Fe_{23}B_6$ into another metastable phase: primitive tetragonal Fe_3B, which is closely related to the phase previously identified under hypercooling the liquid by $\Delta T \sim 386\ K$.[141] Taken together, the time-resolved high-energy x-ray diffraction data and volume thermal expansion measurements provide strong evidence for the persistence of coherently oriented $Fe_{23}B_6$ and γ-Fe to low temperature, emphasizing the importance of interactions between metastable phases during the solidification of undercooled liquids.

Bibliography

[1] PK Liao and KE Spear. B–Fe (Boron–Iron). *Binary Alloy Phase Diagrams*, 1:480–483, 1990.

[2] KW Andrews. Tabulation of interplanar spacings of cementite Fe_3C. *Acta Crystallographica*, 16(1):68–68, 1963.

[3] AJ Vogt. Private communication.

[4] R. C. O'Handley, R. Hasegawa, R. Ray, and C.-P. Chou. Ferromagnetic properties of some new metallic glasses. *Applied Physics Letters*, 29(6):330, 1976.

[5] LA Davis, R Ray, C-P Chou, and RC O'handley. Mechanical and thermal properties of $Fe_{80}B_{20}$ glass. *Scripta Metallurgica*, 10(6):541–546, 1976.

[6] R Hasegawa, R C O Handley, L E Tanner, R Ray, S Kavesh, R Hasegawa, R C O Handley, L E Tanner, R Ray, and S Kavesh. Magnetization, magnetic anisotropy, and domain patterns of $Fe_{80}B_{20}$ glass. 219, 1976.

[7] Robert C OHandley, LI Mendelsohn, R Hasegawa, R Ray, and S Kavesh. Low-field magnetic properties of $Fe_{80}B_{20}$ glass. *Journal of Applied Physics*, 47(10):4660–4662, 1976.

[8] FE Luborsky. Amorphous ferromagnets. *Handbook of Ferromagnetic Materials*, 1:451–529, 1980.

[9] Y. D. Zhang, J. I. Budnick, J. C. Ford, W. A. Hines, F. H. Sanchez, and R. Hasegawa. Crystallization of Fe-B amorphous alloys: A NMR and x-ray study. *Journal of Applied Physics*, 61(8):3231–3233, 1987.

[10] A. S. Schaafsma, H. Snijders, F. Van Der Woude, J. W. Drijver, and S. Radelaar. Amorphous to crystalline transformation of $Fe_{80}B_{20}$. *Physical Review B*, 20(11):4423–4430, 1979.

[11] JA Leake and AL Greer. An examination of the sources of variation in the measured properties of $Fe_{80}B_{20}$ glass. *Journal of Non-Crystalline Solids*, 38:735–740, 1980.

[12] OT Inal, L Keller, and FG Yost. High-temperature crystallization behaviour of amorphous $Fe_{80}B_{20}$. *Journal of Materials Science*, 15(8):1947–1961, 1980.

[13] T Kemeny, I. Vincze, T. Kemény, B. Fogarassy, and Sigurds Arajs. Structure and crystallization of Fe-B metallic glasses. *Physical Review B*, 20(2):476–488, jul 1979.

[14] Akira Takeuchi and Akihisa Inoue. Quantitative evaluation of critical cooling rate for metallic glasses. *Materials Science and Engineering: A*, 304:446–451, 2001.

[15] Stig Rundqvist and Franz Jellinek. *The Structures of Ni_6B, Si_2B, Fe_2B and Some Related Phases*. United States Air Force, Office of Scientific Research, 1958.

[16] W Yl Ching, Yong-Nian Xu, BN Harmon, Jun Ye, and TC Leung. Electronic structures of Feb, Fe_2b, and Fe_3b compounds studied using first-principles spin-polarized calculations. *Physical Review B*, 42(7):4460, 1990.

[17] MC Cadeville and AJP Meyer. Points de curie et moments des borures ferromagnetiques du groupe du fer de type m2b, mb,(m1, m2) 2b et (m1, m2) b. *Comptes rendus*, 255(24):3391, 1962.

[18] Kenneth A Murphy and N Hershkowitz. Temperature-dependent hyperfine interactions in Fe_2b. *Physical Review B*, 7(1):23, 1973.

[19] Yong Kong and Fashen Li. Cohesive energy, local magnetic properties, and Curie temperature of Fe_3B studied using the self-consistent LMTO method. *Physical Review B*, 56(6), 1997.

[20] U Köster and Uy Herold. Crystallization of amorphous $Fe_{80}B_{20}$. *Scripta Metallurgica*, 12(1):75–77, 1978.

[21] P Duhaj. Metastable Fe_4B Phase in Amorphous Fe-B Alloys. *Physica Status Solidi (a)*, 719:719–726, 1980.

[22] A Lo Greer. Crystallisation kinetics of Fe80B20 glass. *Acta Metallurgica*, 30(1):171–192, 1982.

[23] John L Walter, Stanley F Bartram, and Ignacio Mella. Formation and crystallization of alloys with two amorphous phases. *Materials Science and Engineering*, 36(2):193–205, 1978.

[24] CL Chien, D Musser, EM Gyorgy, RC Sherwood, HS Chen, FE Luborsky, and JL Walter. Magnetic properties of amorphous Fe_xB_{100-x} (72 ¡ x ¡ 86) and crystalline Fe_3B. *Physical Review B*, 20(1):283, 1979.

[25] John L Walter, Stanley F Bartram, and Robert R Russell. Crystallization of the amorphous alloys $Fe_{50}Ni_{30}B_{20}$ and $Fe_{80}B_{20}$. *Metallurgical Transactions A*, 9(6):803–814, 1978.

[26] Y Khan and M Sostarich. Dynamic temperature x-ray diffraction analysis of the amorphous $Fe_{80}B_{20}$ alloy. *Z. Metallkd.*, 72(4):266–268, 1981.

[27] Stig Rundqvist. X-ray investigations of the ternary system Fe-P-B. *Acta Chem. Scand*, 16(1):1–19, 1962.

[28] M Mihalkovič and M Widom. Ab initio calculations of cohesive energies of Fe-based glass-forming alloys. *Physical Review B*, 70(14):144107, 2004.

[29] R Coehoorn, DB De Mooij, and C de de Waard. Meltspun permanent magnet materials containing Fe_3B as the main phase. *Journal of Magnetism and Magnetic Materials*, 80(1):101–104, 1989.

[30] M. Sagawa, S. Fujimura, H. Yamamoto, Y. Matsuura, and S. Hirosawa. Magnetic properties of rare-earth-iron-boron permanent magnet materials. *Journal of Applied Physics*, 57(8):4094, 1985.

[31] Lunan Huang, Valentin Taufour, T. N. Lamichhane, Benjamin Schrunk, Sergei L. Bud'Ko, P. C. Canfield, and Adam Kaminski. Imaging the magnetic nanodomains in $Nd_2Fe_{14}B$. *Physical Review B - Condensed Matter and Materials Physics*, 93(9):2–5, 2016.

[32] Eckart F Kneller and Reinhard Hawig. The exchange-spring magnet: a new material principle for permanent magnets. *IEEE Transactions on Magnetics*, 27(4):3588–3560, 1991.

[33] Y. T. Shen, T. H. Kim, a. K. Gangopadhyay, and K. F. Kelton. Icosahedral Order, Frustration, and the Glass Transition: Evidence from Time-Dependent Nucleation and Supercooled Liquid Structure Studies. *Physical Review Letters*, 102(5):6–9, feb 2009.

[34] DG Quirinale, GE Rustan, SR Wilson, MJ Kramer, AI Goldman, and MI Mendelev. Appearance of metastable B2 phase during solidification of $Ni_{50}Zr_{50}$ alloy: electrostatic levitation and molecular dynamics simulation studies. *Journal of Physics: Condensed Matter*, 27(8):085004, 2015.

[35] J Delamare, D Lemarchand, and P Vigier. Structural investigation of the metastable compound A1 in an as-cast Fe-Nd eutectic alloy. *Journal of alloys and compounds*, 216(2):273–280, 1995.

[36] KHJ Buschow, DB De Mooij, JLC Daams, and HM Van Noort. Phase relationships, magnetic and crystallographic properties of Nd-Fe-B alloys. *Journal of the Less Common Metals*, 115(2):357–366, 1986.

[37] Kazuhiko Kuribayashi and Shumpei Ozawa. Metastable phase formation from undercooled melt of Nd–Fe–B alloys. *Journal of alloys and compounds*, 408:266–272, 2006.

[38] J Gao, T Volkmann, and DM Herlach. Undercooling-dependent solidification behavior of levitated $Nd_{14}Fe_{79}B_7$ alloy droplets. *Acta materialia*, 50(11):3003–3012, 2002.

[39] J. Gao, T. Volkmann, S. Roth, W. Löser, and D.M. Herlach. Phase formation in undercooled NdFeB alloy droplets. *Journal of Magnetism and Magnetic Materials*, 234(2):313–319, sep 2001.

[40] BM Ma, JW Herchenroeder, B Smith, M Suda, DN Brown, and Z Chen. Recent development in bonded ndfeb magnets. *Journal of magnetism and magnetic materials*, 239(1):418–423, 2002.

[41] Jianding Yu, Paul-François Paradis, Takehiko Ishikawa, Shinichi Yoda, Shunpei Ozawa, Tetsuji Saito, and Tetsuichi Motegi. Containerless solidification of undercooled $Nd_2Fe_{14}B$ by electrostatic levitation furnace. *Japanese journal of applied physics*, 41(5R):2908, 2002.

[42] Changlin Yang, Feng Liu, Gencang Yang, Yuzeng Chen, Ning Liu, Jinshan Li, and Yaohe Zhou. Non-equilibrium transformation in hypercooled $Fe_{83}B_{17}$ alloy. *Materials Science and Engineering: A*, 458(1-2):1–6, jun 2007.

[43] Changlin Yang, Feng Liu, Gencang Yang, and Yaohe Zhou. Structure evolution upon non-equilibrium solidification of bulk undercooled FeB system. *Journal of Crystal Growth*, 311(2):404–412, jan 2009.

[44] Livio Battezzati, Carlo Antonione, and Marcello Baricco. Undercooling of Ni-B and Fe-B alloys and their metastable phase diagrams. *Journal of Alloys and Compounds*, 247(1-2):164–171, jan 1997.

[45] Akitoshi Mizuno, Jin Tamura, Shinji Kohara, and Masahito Watanabe. Time-Resolved X-Ray Diffraction Study on Solidification of Fe-B and Fe-C Eutectic Alloys. *Materials Science Forum*, 706-709:1702–1706, jan 2012.

[46] V. a. Barinov, V. a. Tsurin, V. I. Voronin, and V. T. Surikov. Instability of the $Fe_{23}B_6$ phase during thermomechanical treatment. *The Physics of Metals and Metallography*, 108(1):50–58, jul 2009.

[47] V. a. Barinov, V. a. Tsurin, and V. T. Surikov. DAPO effect in $Fe_{23}B_6$. *The Physics of Metals and Metallography*, 113(1):48–61, jan 2012.

[48] C.M. Fang, M.a. van Huis, M.H.F. Sluiter, and H.W. Zandbergen. Stability, structure and electronic properties of γ-$Fe_{23}C_6$ from first-principles theory. *Acta Materialia*, 58(8):2968–2977, may 2010.

[49] C. M. Fang, M. H. F. Sluiter, M. a. van Huis, C. K. Ande, and H. W. Zandbergen. Origin of Predominance of Cementite among Iron Carbides in Steel at Elevated Temperature. *Physical Review Letters*, 105(5):055503, jul 2010.

[50] M Widom and M Mihalkovic. Stability of fe-based alloys with structure type C_6Cr_{23}. *Journal of materials research*, 20(01):237–242, 2005.

[51] PR Ohodnicki Jr, NC Cates, DE Laughlin, ME McHenry, and M Widom. Ab initio theoretical study of magnetization and phase stability of the $(Fe,Co,Ni)_{23}B_6$ and $(Fe,Co,Ni)_{23}Zr_6$ structures of $Cr_{23}C_6$ and $Mn_{23}Th_6$ prototypes. *Physical Review B*, 78(14):144414, 2008.

[52] I Vincze, T Kemeny, and Sigurds Arajs. Short-range order in transition-metalmetalloid glasses. *Physical Review B*, 21(3):937, 1980.

[53] JM Dubois and G Le Caer. Ordre local et proprietes physiques des verres metalliques riches en fer. *Acta Metallurgica*, 32(11):2101–2114, 1984.

[54] Daniel B Miracle. A structural model for metallic glasses. *Nature materials*, 3(10):697, 2004.

[55] Akihiko Hirata, Yoshihiko Hirotsu, and Eiichiro Matsubara. Local atomic structures of amorphous $Fe_{80}B_{20}$ and $Fe_{70}Nb_{10}B_{20}$ alloys studied by electron diffraction. *Materials transactions*, 46(12):2781–2784, 2005.

[56] E Nold, P Lamparter, H Olbrich, and S Steeb. Determination of the Partial Structure Factors of the Metallic Glass $Fe_{80}B_{20}$. *Zeitschrift für Naturforschung A*, 36(10):1032–1044, 1981.

[57] P Ganesh and M Widom. Geometrical frustration in liquid Fe and Fe-based metallic glass. *arXiv preprint cond-mat/0702263*, 2007.

[58] Dmitri V Louzguine-Luzgin, Konstantinos Georgarakis, Andrey Tsarkov, Alexey Solonin, Veijo Honkimaki, Louis Hennet, and Alain R Yavari. Structural changes in liquid Fe and Fe-b alloy on cooling. *Journal of Molecular Liquids*, 209:233–238, 2015.

[59] G. Lee, a. Gangopadhyay, K. Kelton, R. Hyers, T. Rathz, J. Rogers, and D.S. Robinson. Difference in Icosahedral Short-Range Order in Early and Late Transition Metal Liquids. *Physical Review Letters*, 93(3):1–4, jul 2004.

[60] Ken Kelton and Alan Lindsay Greer. *Nucleation in condensed matter: applications in materials and biology*, volume 15. Elsevier, 2010.

[61] SG Hao, CZ Wang, MJ Kramer, and KM Ho. Microscopic origin of slow dynamics at the good glass forming composition range in $Zr_{1-x}Cu_x$ metallic liquids. *Journal of Applied Physics*, 107(5):053511, 2010.

[62] Gustav Errol Rustan. Electrostatic levitation studies of supercooled liquids and metastable solid phases. *PhD Thesis*, 2014.

[63] David L Price. *High-temperature levitated materials*. Cambridge University Press, 2010.

[64] HS Schnyders and JB Van Zytveld. Electrical resistivity and thermopower of liquid Ge and Si. *Journal of Physics: Condensed Matter*, 8(50):10875, 1996.

[65] Dieter M Herlach. Metastable solids from undercooled melts. In *Materials science forum*, volume 539, pages 1977–1982. Trans Tech Publ, 2007.

[66] G Jacobs, I Egry, E Gorges, and M Langen. Measurement of Density and Structural Short-Range Order of Levitated Liquid Metals 1. 19(3):895–903, 1998.

[67] C Bührer, M Beckmann, M Fähnle, U Grünewald, and K Maier. The liquid ferromagnet $Co_{80}Pd_{20}$ and its critical exponent γ. *Journal of magnetism and magnetic materials*, 212(1):211–224, 2000.

[68] D Holland-Moritz, T Schenk, P Convert, T Hansen, and DM Herlach. Electromagnetic levitation apparatus for diffraction investigations on the short-range order of undercooled metallic melts. *Measurement Science and Technology*, 16(2):372, 2005.

[69] Georg Lohöfer. Electrical resistivity measurement of liquid metals. *Measurement Science and Technology*, 16(2):417–425, 2005.

[70] J. K. Richard Weber. The Containerless Synthesis of Glass. *International Journal of Applied Glass Science*, 1(3):248–256, sep 2010.

[71] W. J. Xie, C. D. Cao, Y. J. Lü, Z. Y. Hong, and B. Wei. Acoustic method for levitation of small living animals. *Applied Physics Letters*, 89(21):126–129, 2006.

[72] JK Richard Weber, D Scott Hampton, Dennis R Merkley, Charles A Rey, Mark M Zatarski, and Paul C Nordine. Aero-acoustic levitation: A method for containerless liquid-phase processing at high temperatures. *Review of scientific instruments*, 65(2):456–465, 1994.

[73] Paul Fran??ois Paradis, Takehiko Ishikawa, Geun Woo Lee, Dirk Holland-Moritz, J??rgen Brillo, Won Kyu Rhim, and Junpei T. Okada. Materials properties measurements and particle beam interactions studies using electrostatic levitation. *Materials Science and Engineering R: Reports*, 76(1):1–53, 2014.

[74] Aaron J Rulison and Won-Kyu Rhim. A noncontact measurement technique for the specific heat and total hemispherical emissivity of undercooled refractory materials. *Review of scientific instruments*, 65(3):695–700, 1994.

[75] P.-F. Paradis, T. Ishikawa, and S. Yoda. Electrostatic Levitation Research and Development at JAXA: Past and Present Activities in Thermophysics. *International Journal of Thermophysics*, 26(4):1031–1049, jul 2005.

[76] Jonghyun Lee, RC Bradshaw, RW Hyers, JR Rogers, TJ Rathz, JJ Wall, H Choo, and PK Liaw. Non-contact measurement of creep resistance of ultra-high-temperature materials. *Materials Science and Engineering: A*, 463(1):185–196, 2007.

[77] Won-Kyu Rhim, Kenichi Ohsaka, Paul-Francois Paradis, and R. Erik Spjut. Noncontact technique for measuring surface tension and viscosity of molten materials using high temperature electrostatic levitation. *Review of Scientific Instruments*, 70(6):2796, 1999.

[78] Won-Kyu Rhim and Takehiko Ishikawa. Noncontact surface tension measurement by drop rotation. *Review of Scientific Instruments*, 72(9):3572, 2001.

[79] R. C. Bradshaw, D. P. Schmidt, J. R. Rogers, K. F. Kelton, and R. W. Hyers. Machine vision for high-precision volume measurement applied to levitated containerless material processing. *Review of Scientific Instruments*, 76(12):125108, 2005.

[80] TJ Rathz, MB Robinson, RW Hyers, JR Rogers, and D Li. Triggered nucleation in $ni_{60}nb_{40}$ using an electrostatic levitator. *Journal of materials science letters*, 21(4):301–303, 2002.

[81] Aaron J Rulison, John L Watkins, and Brian Zambrano. Electrostatic containerless processing system. *Review of scientific instruments*, 68(7):2856–2863, 1997.

[82] a. K. Gangopadhyay, G. W. Lee, K. F. Kelton, J. R. Rogers, a. I. Goldman, D. S. Robinson, T. J. Rathz, and R. W. Hyers. Beamline electrostatic levitator for in situ high energy x-ray diffraction studies of levitated solids and liquids. *Review of Scientific Instruments*, 76(7):073901, 2005.

[83] T. Kim, G. Lee, B. Sieve, a. Gangopadhyay, R. Hyers, T. Rathz, J. Rogers, D. Robinson, K. Kelton, and a. Goldman. Insitu High-Energy X-Ray Diffraction Study of the Local Structure of Supercooled Liquid Si. *Physical Review Letters*, 95(8):1–4, aug 2005.

[84] T. H. Kim, a. I. Goldman, and K. F. Kelton. Structural study of supercooled liquid silicon. *Philosophical Magazine*, 88(2):171–179, jan 2008.

[85] K. Kelton, G. Lee, a. Gangopadhyay, R. Hyers, T. Rathz, J. Rogers, M. Robinson, and D. Robinson. First X-Ray Scattering Studies on Electrostatically Levitated Metallic Liquids: Demonstrated Influence of Local Icosahedral Order on the Nucleation Barrier. *Physical Review Letters*, 90(19):19–22, may 2003.

[86] K.F Kelton, a.K Gangopadhyay, G.W Lee, L Hannet, Robert W Hyers, S Krishnan, Michael B Robinson, Jan Rogers, and Thomas J Rathz. X-ray and electrostatic levitation

undercooling studies in TiZrNi quasicrystal forming alloys. *Journal of Non-Crystalline Solids*, 312-314:305–308, 2002.

[87] N a Mauro and K F Kelton. A highly modular beamline electrostatic levitation facility, optimized for in situ high-energy x-ray scattering studies of equilibrium and supercooled liquids. *The Review of scientific instruments*, 82(3):035114, mar 2011.

[88] J. C. Bendert, A. K. Gangopadhyay, N. A. Mauro, and K. F. Kelton. Volume expansion measurements in metallic liquids and their relation to fragility and glass forming ability: An energy landscape interpretation. *Physical Review Letters*, 109(18):1–5, 2012.

[89] J. C. Bendert, N. a. Mauro, and K. F. Kelton. Pair distribution function analysis of X-ray diffraction from amorphous spheres in an asymmetric transmission geometry: application to a Zr58.5Cu15.6Ni12.8Al10.3Nb2.8 glass. *Journal of Applied Crystallography*, 46:999–1007, 2013.

[90] ME Blodgett, Takeshi Egami, Z Nussinov, and KF Kelton. Proposal for universality in the viscosity of metallic liquids. *Scientific reports*, 5, 2015.

[91] N A Mauro, A J Vogt, K S Derendorf, M L Johnson, G E Rustan, D G Quirinale, A Kreyysig, K A Lokshin, J C Neuefeind, Ke An, Xun-li Wang, A I Goldman, T Egami, and K F Kelton. Electrostatic levitation facility optimized for neutron diffraction studies of high temperature liquids at a spallation neutron source Electrostatic levitation facility optimized for neutron diffraction studies of high temperature liquids at a spallation . 013904, 2016.

[92] M L Johnson, M E Blodgett, K A Lokshin, N A Mauro, J Neuefeind, C Pueblo, D G Quirinale, A J Vogt, T Egami, A I Goldman, and K F Kelton. Measurements of structural and chemical order in $Zr_{80}Pt_{20}$ and $Zr_{77}Rh_{23}$ liquids. 054203:1–12, 2016.

[93] G. E. Rustan, N. S. Spyrison, A. Kreyssig, R. Prozorov, and A. I. Goldman. Noncontact technique for measuring the electrical resistivity and magnetic susceptibility of electrostatically levitated materials. *Review of Scientific Instruments*, 83(10):0–7, 2012.

[94] D.M. Herlach, D. Holland-Moritz, Th. Schenk, K. Schneider, G. Wilde, O. Boni, J. Fransaer, and F. Spaepen. Undercoolability of pure Co and Co-based alloys. *Journal of Non-Crystalline Solids*, 250-252:271–276, aug 1999.

[95] CZ et al. Wang. Structure and dynamics of the liquid-liquid phase transition in silicon. *In Preparation*, 2017.

[96] D G Quirinale, G E Rustan, S R Wilson, M J Kramer, a I Goldman, and M I Mendelev. Appearance of metastable B2 phase during solidification of Ni50Zr50 alloy: electrostatic levitation and molecular dynamics simulation studies. *Journal of physics. Condensed matter : an Institute of Physics journal*, 27(8):85004, mar 2015.

[97] DG Quirinale, A Kreyssig, S Saunders, D Messina, WE Straszheim, PC Canfield, MJ Kramer, and AI Goldman. The solidifcation of Al-Pd-Mn studied by high-energy x-ray diffraction from electrostatically levitated samples. *Zeitschrift für Kristallographie*, In press.

[98] Nicholas Mauro. Structural and thermophysical property studies of metallic liquids and glasses using the beamline electrostatic levitation technique. *PhD Thesis*.

[99] N a Mauro and K F Kelton. A highly modular beamline electrostatic levitation facility, optimized for in situ high-energy x-ray scattering studies of equilibrium and supercooled liquids. *The Review of scientific instruments*, 82(3):035114, mar 2011.

[100] Kevin Derendorf. *The Design, Construction, and Implementation of an Electrostatic Levitation Facility for Neutron Scattering Studies of Liquids*. PhD thesis, 2013.

[101] Samuel Earnshaw. On the nature of the molecular forces which regulate the constitution of the luminiferous ether. *Trans. Camb. Phil. Soc*, 7:97–112, 1842.

[102] T. Meister, H. Werner, G. Lohoefer, D.M. Herlach, and H. Unbehauen. Gain-scheduled control of an electrostatic levitator. *Control Engineering Practice*, 11(2):117–128, feb 2003.

[103] Won-Kyu Rhim and Paul-François Paradis. Laser-induced rotation of a levitated sample in vacuum. *Review of Scientific Instruments*, 70(12):4652–4655, 1999.

[104] J Lee and DM Matson. Prediction of mass evaporation of $fe_{80}co_{20}$ during measurements of thermophysical properties using an electrostatic levitator. *International Journal of Thermophysics*, 35(9-10):1697–1704, 2014.

[105] Won-Kyu Rhim and Kenichi Ohsaka. Thermophysical properties measurement of molten silicon by high-temperature electrostatic levitator: density, volume expansion, specific heat capacity, emissivity, surface tension and viscosity. *Journal of crystal growth*, 208(1):313–321, 2000.

[106] Bernhard Müller and Ulrich Renz. Development of a fast fiber-optic two-color pyrometer for the temperature measurement of surfaces with varying emissivities. *Review of scientific instruments*, 72(8):3366–3374, 2001.

[107] Georg Lohöfer. Electrical resistivity measurement of liquid metals. *Measurement Science and Technology*, 16(2):417–425, feb 2005.

[108] M. D. Vannette, A. S. Sefat, S. Jia, S. A. Law, G. Lapertot, S. L. Bud'ko, P. C. Canfield, J. Schmalian, and R. Prozorov. Precise measurements of radio-frequency magnetic susceptibility in ferromagnetic and antiferromagnetic materials. *Journal of Magnetism and Magnetic Materials*, 320(3-4):354–363, 2008.

[109] R. Prozorov, M. D. Vannette, R. T. Gordon, C. Martin, S. L. Bud'ko, and P. C. Canfield. Coexistence of Long-Range Magnetic Order and Superconductivity from Campbell Penetration Depth Measurements. (September 2008):1–11, 2008.

[110] Matthew Dano Vannette. Dynamic magnetic susceptibility of systems with long-range magnetic order. 2009.

[111] John David Jackson and Ronald F Fox. Classical electrodynamics. *American Journal of Physics*, 67(9):841–842, 1999.

[112] Hirokatsu Aoki, Paul-François Paradis, Takehiko Ishikawa, Tomotsugu Aoyama, Tadahiko Masaki, Shinich Yoda, Yoshinobu Ishii, and Toshio Itami. Development of an electrostatic levitator for neutron diffraction structure analysis. *Review of scientific instruments*, 74(2):1147–1149, 2003.

[113] Tobias Kordel, Dirk Holland-Moritz, Fan Yang, J Peters, T Unruh, Thomas Hansen, and Andreas Meyer. Neutron scattering experiments on liquid droplets using electrostatic levitation. *Physical Review B*, 83(10):104205, 2011.

[114] T H Kim and K F Kelton. Structural study of supercooled liquid transition metals. *The Journal of chemical physics*, 126(5):054513, feb 2007.

[115] Allen C Larson and Robert B Von Dreele. Gsas. *General Structure Analysis System. LANSCE, MS-H805, Los Alamos, New Mexico*, 1994.

[116] AP Hammersley. Internal report esrf97ha02t. *ESRF, Grenoble, France*, 1997.

[117] Donald S Young, Bruce S Sachais, and Leigh C Jefferies. The rietveld method. 1993.

[118] J. C. Bendert, M. E. Blodgett, and K. F. Kelton. Calculation of absorption and secondary scattering of X-rays by spherical amorphous materials in an asymmetric transmission geometry. *Acta Crystallographica Section A: Foundations of Crystallography*, 69(2):131–139, mar 2013.

[119] Johannes Schindelin, Curtis T Rueden, Mark C Hiner, and Kevin W Eliceiri. The imagej ecosystem: an open platform for biomedical image analysis. *Molecular reproduction and development*, 82(7-8):518–529, 2015.

[120] A. P. Hammersley, S. O. Svensson, M. Hanfland, A. N. Fitch, and D. Hausermann. Two-dimensional detector software: From real detector to idealised image or two-theta scan. *High Pressure Research*, 14(4-6):235–248, 1996.

[121] Brian H Toby. Expgui, a graphical user interface for gsas. *Journal of applied crystallography*, 34(2):210–213, 2001.

[122] Milton Abramowitz and Irene A Stegun. *Handbook of mathematical functions: with formulas, graphs, and mathematical tables*, volume 55. Courier Corporation, 1964.

[123] Simon Bates, George Zografi, David Engers, Kenneth Morris, Kieran Crowley, and Ann Newman. Analysis of amorphous and nanocrystalline solids from their X-ray diffraction patterns. *Pharmaceutical research*, 23(10):2333–49, oct 2006.

[124] M. Baricco, S. Enzo, T.a. Baser, M. Satta, G. Vaughan, and a.R. Yavari. Amorphous/nanocrystalline composites analysed by the Rietveld method. *Journal of Alloys and Compounds*, 495(2):377–381, apr 2010.

[125] Yoshio Waseda. *The structure of non-crystalline materials: liquids and amorphous solids*. McGraw-Hill, 1980.

[126] Takeshi Egami and Simon JL Billinge. *Underneath the Bragg peaks: structural analysis of complex materials*, volume 16. Newnes, 2012.

[127] Peter F Peterson, Emil S Božin, Th Proffen, and Simon JL Billinge. Improved measures of quality for the atomic pair distribution function. *Journal of applied crystallography*, 36(1):53–64, 2003.

[128] Mark Johnson. Structural Evolution, Chemical Order, and Crystallization of Metallic Liquids and Glasses. 2015.

[129] Chris Rycroft. Voro++: A three-dimensional voronoi cell library in c++. *Lawrence Berkeley National Laboratory*, 2009.

[130] Alexander Stukowski. Visualization and analysis of atomistic simulation data with ovito–the open visualization tool. *Modelling and Simulation in Materials Science and Engineering*, 18(1):015012, 2009.

[131] RL McGreevy and L Pusztai. Reverse monte carlo simulation: a new technique for the determination of disordered structures. *Molecular Simulation*, 1(6):359–367, 1988.

[132] DG Quirinale, GE Rustan, A Kreyssig, SH Lapidus, MJ Kramer, and AI Goldman. The solidification products of levitated $Fe_{83}B_{17}$ studied by high-energy x-ray diffraction. *Journal of Applied Physics*, 120(17):175104, 2016.

[133] R. Hasegawa and Ranjan Ray. Iron-boron metallic glasses. *Journal of Applied Physics*, 49(7):4174, jul 1978.

[134] Nicholas Decristofaro, Alfred Freilich, and Gordon Fish. Formation and magnetic properties of fe-b-si metallic glasses. *Journal of Materials Science*, 17(8):2365–2370, 1982.

[135] SJ Pang, T Zhang, K Asami, and A Inoue. Synthesis of fe–cr–mo–c–b–p bulk metallic glasses with high corrosion resistance. *Acta Materialia*, 50(3):489–497, 2002.

[136] Liqun Ma, L Wang, T Zhang, and A Inoue. Effect of nb addition on glass-forming ability, strength, and hardness of fe–b–zr amorphous alloys. *Materials research bulletin*, 34(6):915–920, 1999.

[137] TD Shen and RB Schwarz. Bulk ferromagnetic glasses prepared by flux melting and water quenching. *Applied Physics Letters*, 75(1):49–51, 1999.

[138] Akihisa Inoue, Tao Zhang, Takaomi Itoi, and Akira Takeuchi. New fe–co–ni–zr–b amorphous alloys with wide supercooled liquid regions and good soft magnetic properties. *Materials Transactions, JIM*, 38(4):359–362, 1997.

[139] M Aykol, AO Mekhrabov, and MV Akdeniz. Nano-scale phase separation in amorphous fe-b alloys: Atomic and cluster ordering. *Acta Materialia*, 57(1):171–181, 2009.

[140] Akihiko Hirata, Yoshihiko Hirotsu, Tadakatsu Ohkubo, Takeshi Hanada, and V. Z. Bengus. Compositional dependence of local atomic structures in amorphous Fe 100 x B x (x = 14 , 17 , 20) alloys studied by electron diffraction and high-resolution electron microscopy. *Physical Review B*, 74(21):214206, dec 2006.

[141] Changlin Yang, Gencang Yang, Feng Liu, Yuzeng Chen, N. Liu, D. Chen, and Yaohe Zhou. Metastable phase formation in eutectic solidification of highly undercooled $Fe_{83}B_{17}$ alloy melt. *Physica B: Condensed Matter*, 373(1):136–141, mar 2006.

[142] M. Tomut and H. Chiriac. Viscosity and surface tension of liquid Femetalloid glass-forming alloys. *Materials Science and Engineering: A*, 304-306:272–276, may 2001.

[143] M. Palumbo, G. Cacciamani, E. Bosco, and M. Baricco. Driving forces for crystal nucleation in FeB liquid and amorphous alloys. *Intermetallics*, 11(11-12):1293–1299, jan 2003.

[144] P. Ganesh and M. Widom. Ab initio simulations of geometrical frustration in supercooled liquid Fe and Fe-based metallic glass. *Physical Review B*, 77(1):014205, jan 2008.

[145] Lei Yang, Jingyu Qin, Shaopeng Pan, and Xiufang Bian. The shoulder in the second peak of the pair correlation function of superheated liquid $Fe_{80}B_{20}$ alloy. *Journal of Non-Crystalline Solids*, 357(16):3207–3211, 2011.

[146] DG Quirinale, GE Rustan, A Kreyssig, and AI Goldman. Synergistic stabilization of metastable $Fe_{23}B_6$ and γ-Fe in undercooled $Fe_{83}B_{17}$. *Applied Physics Letters*, 106(24):241906, 2015.

[147] PK Liao, KE Spear, and TB Massalski. Binary alloy phase diagrams. *ASM International, Materials Park, Ohio*, 1:557–559, 1990.

[148] TC Chiang, FJ Himpsel, A Goldmann, and EE Koch. Springermaterials–landolt-börnstein database.

[149] Caroline A Schneider, Wayne S Rasband, and Kevin W Eliceiri. Nih image to imagej: 25 years of image analysis. *Nature methods*, 9(7):671, 2012.

[150] A Kirilyuk, J Giergiel, J Shen, M Straub, and J Kirschner. Growth of stabilized γ-fe films and their magnetic properties. *Physical Review B*, 54(2):1050, 1996.

[151] GA Prinz. Stabilization of bcc co via epitaxial growth on gaas. *Physical Review Letters*, 54(10):1051, 1985.

[152] Daniel James Branagan, YL Tang, AV Sergueeva, and AK Mukherjee. Low-temperature superplasticity in a nanocomposite iron alloy derived from a metallic glass. *Nanotechnology*, 14(11):1216, 2003.

[153] WA Jesser and J Wo Matthews. Evidence for pseudomorphic growth of iron on copper. *Philosophical Magazine*, 15(138):1097–1106, 1967.

[154] WA Jesser and JW Matthews. Pseudomorphic growth of iron on hot copper. *Philosophical Magazine*, 17(147):595–602, 1968.

[155] U Gradmann and P Tillmanns. Supersaturation and mode of growth for fe films on cu (111). an experimental study using leed and aes. *physica status solidi (a)*, 44(2):539–547, 1977.

[156] W Keune, R Halbauer, U Gonser, J Lauer, and DL Williamson. Antiferromagnetism of fcc fe thin films. *Journal of Magnetism and Magnetic Materials*, 6:192–195, 1977.

[157] W Kümmerle and U Gradmann. Magnetic properties of ferromagnetic γ-fe films on cu (111). *physica status solidi (a)*, 45(1):171–180, 1978.

[158] C Rau, C Schneider, G Xing, and K Jamison. Ferromagnetic order at surfaces of ultrathin epitaxial fcc γ-fe (111) p (11) films on cu (111). *Physical review letters*, 57(25):3221, 1986.

[159] A Amiri-Hezaveh, G Jennings, DJ Joyner, and RF Willis. Electronic and magnetic states of ultra-thin fe films. *Le Journal de Physique Colloques*, 45(C5):C5–371, 1984.

[160] F Pontkees and H Neddermeyer. Electronic and structural properties of thin films of fe on cu (1 1 1) and of the system cu/fe/cu (1 1 1). *Physica B: Condensed Matter*, 161(1-3):276–280, 1990.

[161] JB Newkirk. Mechanism of precipitation in a cu-2. 5 pct fe alloy. *AIME TRANS*, 209:1214–1220, 1957.

[162] P Ehrhart, B Schönfeld, HH Ettwig, and W Pepperhoff. The lattice structure of antiferromagnetic γ-iron. *Journal of Magnetism and Magnetic Materials*, 22(1):79–85, 1980.

[163] Y Tsunoda, S Imada, and N Kunitomi. Anomalous lattice contraction and magnetism of γ-fe precipitates in cu. *Journal of Physics F: Metal Physics*, 18(7):1421, 1988.

[164] Y Tsunoda and N Kunitomi. Structural phase transition of γ-fe precipitates in cu. *Journal of Physics F: Metal Physics*, 18(7):1405, 1988.

[165] L. T. Kong and B. X. Liu. Correlation of magnetic moment versus spacing distance of metastable fcc structured iron. *Applied Physics Letters*, 84(18):3627, 2004.

[166] John J Croat, Jan F Herbst, Robert W Lee, and Frederick E Pinkerton. Pr-fe and nd-fe-based materials: A new class of high-performance permanent magnets. *Journal of Applied Physics*, 55(6):2078–2082, 1984.

[167] David Brown, Bao-Min Ma, and Zhongmin Chen. Developments in the processing and properties of ndfeb-type permanent magnets. *Journal of Magnetism and Magnetic Materials*, 248(3):432–440, 2002.

[168] D Givord, HS Li, and JM Moreau. Magnetic properties and crystal structure of $nd_2fe_{14}b$. *Solid State Communications*, 50(6):497–499, 1984.

[169] M. Palumbo, G. Cacciamani, E. Bosco, and M. Baricco. Thermodynamic Analysis of Glass Formation in Fe-B System. 25(4):625–637, 2002.

[170] Ernesto J Escorcia-Aparicio, RK Kawakami, and ZQ Qiu. fcc fe films grown on a ferromagnetic fcc co (100) substrate. *Physical Review B*, 54(6):4155, 1996.

[171] S Müller, P Bayer, C Reischl, K Heinz, B Feldmann, H Zillgen, and M Wuttig. Structural instability of ferromagnetic fcc fe films on cu (100). *Physical review letters*, 74(5):765, 1995.

[172] D. Bagayoko and J. Callaway. Lattice-parameter dependence of ferromagnetism in bcc and fcc iron. *Physical Review B*, 28(10):5419–5422, 1983.

[173] R Prozorov, RW Giannetta, A Carrington, P Fournier, RL Greene, P Guptasarma, DG Hinks, and AR Banks. Measurements of the absolute value of the penetration depth in high-t c superconductors using a low-t c superconductive coating. *Applied Physics Letters*, 77(25):4202–4204, 2000.

[174] AP Hammersley. High press. res., 1996, 14, 235;(b) ap hammersley, so svensson and a. thomson. *Nucl. Instrum. Methods Phys. Res., Sect. A*, 346:321, 1994.

[175] Allen C Larson and RB Von Dreele. Technical report, 2004.

[176] PJ Brown and JL Cox. Charge and spin density distributions in the ferromagnetic alloy fe_2b. *Philosophical Magazine*, 23(183):705–725, 1971.

[177] Thaddeus B. Massalski and David E. Laughlin. The surprising role of magnetism on the phase stability of Fe (Ferro). *Calphad*, 33(1):3–7, mar 2009.

[178] T Schenk, D Holland-Moritz, and DM Herlach. Observation of magnetically induced crystallization of undercooled co-pd alloys. *EPL (Europhysics Letters)*, 50(3):402, 2000.

[179] D Fruchart, P Chaudouet, R Fruchart, A Rouault, and JP Senateur. Etudes structurales de compose´ s de type ce´ mentite: Effet de l'hydrogene sur fe3c suivi par diffraction neutronique. spectrome´ trie mo¨ ssbauer sur feco2b et co3b dope´ s au57fe. *Journal of Solid State Chemistry*, 51(2):246–252, 1984.

[180] V A Barinov and V T Surikov. Short-Range Atomic Order in the Metastable Fe 23 B 6 Phase. 105(3):262–270, 2008.

[181] V. a. Barinov, V. a. Tsurin, V. I. Voronin, S. I. Novikov, and V. T. Surikov. Mössbauer investigations of the metastable Fe23B6 phase. *The Physics of Metals and Metallography*, 101(5):456–466, may 2006.

[182] C a F Vaz, J a C Bland, and G Lauhoff. Magnetism in ultrathin film structures. *Reports on Progress in Physics*, 71(5):056501, may 2008.

[183] U Gonser, K Krischel, and S Nasu. Ferromagnetic ordering in fcc γ-fe precipitates in cu-au alloys. *Journal of Magnetism and Magnetic Materials*, 15:1145–1146, 1980.

[184] SC Abrahams, L Guttman, and JS Kasper. Neutron diffraction determination of antiferromagnetism in face-centered cubic (γ) iron. *Physical Review*, 127(6):2052, 1962.

[185] L.T. Kong and B.X. Liu. Distinct magnetic states of metastable fcc structured Fe and FeCu alloys studied by ab initio calculations. *Journal of Alloys and Compounds*, 414(1-2):36–41, apr 2006.

[186] R L McGreevy. Understanding liquid structures. *Journal of Physics: Condensed Matter*, 3(42):F9–F22, 1999.

[187] KF Kelton, AL Greer, DM Herlach, and D Holland-Moritz. The influence of order on the nucleation barrier. *MRS bulletin*, 29(12):940–944, 2004.

[188] Yang Sun, Feng Zhang, Zhuo Ye, Yue Zhang, Xiaowei Fang, Zejun Ding, Cai-Zhuang Wang, Mikhail I. Mendelev, Ryan T. Ott, Matthew J. Kramer, and Kai-Ming Ho. Crystal Genes' in Metallic Liquids and Glasses. *Scientific reports*, 6(March):23734, 2016.

[189] JK Weber, Johan G Abadie, April D Hixson, Paul C Nordine, and Gregory A Jerman. Glass formation and polyamorphism in rare-earth oxide–aluminum oxide compositions. *Journal of the American Ceramic Society*, 83(8):1868–1872, 2000.

[190] Francesco Sette, Michael H Krisch, Claudio Masciovecchio, Giancarlo Ruocco, and Giulio Monaco. Dynamics of glasses and glass-forming liquids studied by inelastic x-ray scattering. *Science*, 280(5369):1550–1555, 1998.

[191] Paul F McMillan, Mark Wilson, Martin C Wilding, Dominik Daisenberger, Mohamed Mezouar, and G Neville Greaves. Polyamorphism and liquid–liquid phase transitions: challenges for experiment and theory. *Journal of Physics: Condensed Matter*, 19(41):415101, 2007.

[192] D.M. Herlach, J. Gao, D. Holland-Moritz, and T. Volkmann. Nucleation and phase-selection in undercooled melts. *Materials Science and Engineering: A*, 375-377:9–15, jul 2004.

[193] DM Herlach. Containerless undercooling and solidification of pure metals. *Annual Review of Materials Science*, 1991.

[194] IN Stranski and D Totomanow. Rate of formation of crystal nuclei and the ostwald step rule. *Z. Phys. Chem*, 163:399–408, 1933.

[195] Shaopeng Pan, Shidong Feng, Junwei Qiao, Bangshao Dong, and Jingyu Qin. The atomic structure of liquid Fe–C alloys. *Journal of Alloys and Compounds*, 648:178–183, 2015.

[196] N Mattern, AG Ilinskii, H Hermann, and AV Romanova. X-ray diffraction study on amorphous and liquid Fe-B alloys. *physica status solidi (a)*, 97(2):397–401, 1986.

[197] Yoshio WASEDA, Masanori TOKUDA, and Masayasu OHTANI. The structure of molten Fe and Fe-C alloys by x-ray diffraction. *Tetsu-to-Hagane*, 61(1):54–70, 1975.

[198] Dong Ho Kim, Jin Man Park, Do Hyang Kim, and Won Tae Kim. Development of quaternary Fe–B–Y–Nb bulk glassy alloys with high glass-forming ability. *Journal of materials research*, 22(02):471–477, 2007.

[199] James Christopher Bendert. Thermophysical and Structural Measurements of Liquid Metallic Alloys Using Electrostatic Levitation. *Analysis*, 2013.

[200] Orsolya Gereben and László Pusztai. Rmc_pot: a computer code for reverse monte carlo modeling the structure of disordered systems containing molecules of arbitrary complexity. *Journal of computational chemistry*, 33(29):2285–2291, 2012.

[201] David K Belashchenko, Alexander Mirzoev, and Oleg Ostrovski. Molecular dynamics modelling of liquid Fe-C alloys. *High Temperature Materials and Processes*, 30(4-5):297–303, 2011.

[202] N. a. Mauro, V. Wessels, J. C. Bendert, S. Klein, a. K. Gangopadhyay, M. J. Kramer, S. G. Hao, G. E. Rustan, a. Kreyssig, a. I. Goldman, and K. F. Kelton. Short- and medium-range order in $Zr_{80}Pt_{20}$ liquids. *Physical Review B*, 83(18):184109, may 2011.

[203] Wolfram Research, Inc. Mathematica, Version 11.1. Champaign, IL, 2017.

[204] Chris H Rycroft, Gary S Grest, James W Landry, and Martin Z Bazant. Analysis of granular flow in a pebble-bed nuclear reactor. *Physical review E*, 74(2):021306, 2006.

[205] Junyoung Park and Yoji Shibutani. Effects of atomic size for voronoi tessellation technique on binary and ternary systems of metallic glasses. *Materials transactions*, 47(12):2904–2909, 2006.

[206] William F Gale and Terry C Totemeier. *Smithells metals reference book*. Butterworth-Heinemann, 2003.

[207] Koichi Momma and Fujio Izumi. Vesta: a three-dimensional visualization system for electronic and structural analysis. *Journal of Applied Crystallography*, 41(3):653–658, 2008.

[208] *Neutron News*, 3(3):29–37, 1992.

[209] T. Schenk, D. Holland-Moritz, V. Simonet, R. Bellissent, and D. Herlach. Icosahedral Short-Range Order in Deeply Undercooled Metallic Melts. *Physical Review Letters*, 89(7):1–4, jul 2002.

[210] Hajime Tanaka. Roles of local icosahedral chemical ordering in glass and quasicrystal formation in metallic glass formers. *Journal of Physics: Condensed Matter*, 15(31):L491, 2003.

[211] V. a. Barinov, V. a. Tsurin, S. I. Novikov, I. R. Shein, and V. T. Surikov. Short-range atomic order in Fe2B powders. *The Physics of Metals and Metallography*, 103(5):470–480, may 2007.

[212] R. Hasegawa and Ranjan Ray. Iron-boron metallic glasses. *Journal of Applied Physics*, 49(7):4174–4179, 1978.

[213] P. K. Liao and K. E. Spear. *Binary Alloy Phase Diagrams*, pages 480–483, 1990.

[214] Ursula Herold and U Köster. Metastabile phasen in extreme schnell erstarrten eisen-borlegirungen. *Z. Metallkd*, 69(5):326–332, 1978.

[215] VL Moruzzi, PM Marcus, K Schwarz, and P Mohn. Ferromagnetic phases of bcc and fcc fe, co, and ni. *Physical Review B*, 34(3):1784, 1986.

[216] VL Moruzzi, PM Marcus, and J Kübler. Magnetovolume instabilities and ferromagnetism versus antiferromagnetism in bulk fcc iron and manganese. *Physical Review B*, 39(10):6957, 1989.

[217] R Iglesias and S Palacios. Ab initio studies on the magnetic phase stability of iron. *Acta Materialia*, 55(15):5123–5127, sep 2007.

[218] GJ Johanson, MB McGirr, and DA Wheeler. Determination of the néel temperature of face-centered-cubic iron. *Physical Review B*, 1(7):3208, 1970.